

# Dissertation

submitted to the  
Combined Faculties for the Natural Sciences and for  
Mathematics  
of the Ruperto-Carola University of Heidelberg,  
Germany  
for the degree of  
Doctor of Natural Sciences

Put forward by  
*Miguel David Campos Vidal*  
Born in Talcahuano, Chile  
Oral examination: 25th July 2018



# Phenomenology and Models of Dark Matter and Neutrinos

Referees: Dr. rer. nat. Werner Rodejohann  
Prof. Dr. rer. nat. Tilman Plehn





## Zusammenfassung

Die schwer fassbare Natur dunkler Materie stellt seit Jahrzehnten eine Herausforderung für theoretische und Experimentalphysiker dar. Um beide Herangehensweisen zusammenzuführen, untersuchen wir die Phänomenologie, durch die sich verschiedene vereinfachte Modelle in diversen Experimenten manifestieren würde und betonen dabei die Wichtigkeit ihrer Komplementarität. Wir behandeln die unterschiedlichen Rollen, die Neutrinos im dunkle Materie Problem spielen können. Schließlich betrachten wir eine vollständigere Theorie, welche Neutrinomassen erklärt und einen dunkle Materie Kandidaten stellt. Zunächst analysieren wir das *dark sequential  $Z'$  portal*, bezüglich dessen direkte Detektions- und Beschleunigerexperimente die Eigenschaften des Majorana-Fermions, welches die Rolle der Dunklen Materie übernimmt, am stärksten einschränken lassen. Im Anschluss nehmen wir an, dass ein schweres rechtshändiges Neutrino das Austauscheteilchen zwischen Standardmodell und dem dunklen Sektor darstellt, wodurch dunkle Materie Massen unter 200 GeV durch indirekte Detektionsexperimente ausgeschlossen werden konnten. Wir betrachten auch die Möglichkeit, dass ein keV steriles Neutrino selbst das dunkle Materie Teilchen ist und untersuchen, inwiefern aktuelle und zukünftige Detektionsexperimente dies einschränken können. Schließlich analysieren wir die Phänomenologie eines *Two Higgs-Doublet-Modells* mit einer zusätzlichen  $U(1)_X$  Eichsymmetrie um *flavour changing neutral interactions* zu vermeiden und gleichzeitig Neutrinomassen zu erzeugen. Das Hinzufügen dunkler Materie führt dabei zu weiteren Einschränkungen.

## Abstract

The evasive nature of dark matter has been challenging experimentalists and theorists alike for decades. In order to bridge both approaches, we investigate the phenomenology that different simplified models would imprint on various experiments, stressing the importance of the complementarity that they offer. We also address the different roles that neutrinos can play in the dark matter problem. Finally, we consider a more complete theory able to explain neutrino masses and provide a dark matter candidate. We start by analysing the *dark sequential  $Z'$  portal*, where direct detection and collider searches put the strongest bounds to the Majorana fermion, which plays the role of dark matter. Then we consider a heavy right-handed neutrino as the mediator between the Standard Model and the dark sector, ruling out dark matter masses below 200 GeV through indirect detection. We also explore the possibility of a sterile neutrino in the keV mass range being the dark matter particle itself, assessing how current and future direct detection experiments can impose limits. We conclude by analysing the phenomenology of a Two Higgs-Doublet Model, with the addition of a  $U(1)_X$  gauge symmetry in order to avoid flavour changing neutral interactions and produce neutrino masses at the same time. Further constraints are imposed when dark matter is added in this context.



# Disclaimer

The research presented in this thesis was published in peer-reviewed journals, as follows

- The simplified models presented in chapter 2 were published in “Dark sequential  $Z'$  portal: Collider and direct detection experiments”, *Phys. Rev. D* **97**, no. 4, 043009 (2018), in collaboration with Giorgio Arcadi, Manfred Lindner, Antonio Masiero and Farinaldo S. Queiroz (section 2.2); and “Search for right-handed neutrinos from dark matter annihilation with gamma-rays”, *JCAP* **1707**, no. 07, 016 (2017), in collaboration with Farinaldo S. Queiroz, Carlos E. Yaguna and Christoph Weniger (section 2.3).
- The study performed in chapter 3 contains work published in “Testing keV sterile neutrino dark matter in future direct detection experiments”, *Phys. Rev. D* **94**, no. 9, 095010 (2016), in collaboration with Werner Rodejohann.
- The model introduced in chapter 4 is based on “Neutrino masses and absence of flavor changing interactions in the 2HDM from gauge principles”, *JHEP* **1708**, 092 (2017), in collaboration with D. Cogollo, Manfred Lindner, T. Melo, Farinaldo S. Queiroz and Werner Rodejohann.



# Acknowledgments

This has been certainly an interesting journey. Not quite that of a hero, but full of rough patches and incredibly rewarding moments all the same, as any journey worth telling about. Luckily, it was about both, the journey and the destination. And I could have not possibly made it without the help of a few people I would like to acknowledge.

I am most thankful to my advisor, Werner Rodejohann for believing in me in the first place, for encouraging me through different scientific endeavours and for his general support and advice along the way. I am very fortunate to have had the opportunity of spending these years at the Max-Planck-Institut für Kernphysik, for which I would like to thank the director of our division, Manfred Lindner; its incredibly helpful administrative staff, Ludmila Hollmach, Britta Schwarz and Anja Berneiser; and all its members, both past and present, who not just created an enjoyable work environment but also were always ready to share their valuable insights into the different aspects of physics and otherwise. I am grateful to all of them, but particular thanks must go to Farinaldo Queiroz, whose sharp and solid advice put me back on track more than once. I'm certain that the experiences he shared will come handy in the future. Special thanks also go to my officemate, Anatoly Smolnikov, for his anecdotes and Russian chocolates.

I am indebted to those who sacrificed their time proofreading different parts of this thesis: Sebastian Ohmer, Thomas Hügler, Alex Helmboldt, Julia Haser and Marvin Lüben. If it approaches to any good is thanks to them, while its many shortcomings are my own. I want to additionally thank Julia for her encouraging words and all the hours spent dissecting the many aspects of life as a scientist; and Marvin for his friendship and his guidance through the German wilderness.

I owe thanks to the many friends I have encountered in the glorious little town of Heidelberg. And also to my former bachelor peers, scattered through Europe. I thank them for their kind words, their quips and for generally being there for me to lean on when I needed it. They greatly contributed to the bright sides of this journey.

I would like to express my gratitude to the people who have gone through our wonderful *WG*, for their warmth and all the amazing moments we spent together. A very special thanks to those who helped me towards the completion of this thesis, Marcel Laqueur and Jonas Kuhn, for their care, their time invested and their English and German advice, respectively. And to Mr. Spock, who was always willing to contribute by sitting on my keyboard.

Me gustaría también expresar mi gratitud por el cariño de mis amigos en Chile, quienes siempre han estado presentes, a pesar de la distancia. Finalmente, quiero agradecer de la manera más profunda el apoyo incondicional de mi familia. Mi hermana siempre ha tenido las palabras adecuadas cuando las he necesitado, tanto en lo personal como en lo científico, mientras que el amor y entrega invariable de mis padres ha sido un faro en todo momento. Sin ustedes jamás podría haber llegado a este punto. Gracias.

*Heidelberg, May 2018*  
*Miguel D. Campos*

*The evolution of the world can be compared to a display of fireworks that has just ended: some few red wisps, ashes, and smoke. Standing on a cooled cinder, we see the slow fading of the suns, and we try to recall the vanished brilliance of the origin of the worlds.*

Georges Lemaitre





# Table of Contents

<b>Abstract</b>	<b>i</b>
<b>Disclaimer</b>	<b>iii</b>
<b>Acknowledgments</b>	<b>v</b>
<b>1 Introduction</b>	<b>1-1</b>
1.1 The Current State of Affairs . . . . .	1-1
1.2 The Area of Knowledge: The Standard Model . . . . .	1-3
1.2.1 The Dawn of the SM . . . . .	1-3
1.2.2 The SM Symmetry Group . . . . .	1-5
1.3 The Perimeter of Ignorance: Dark Matter . . . . .	1-9
1.3.1 The Evidence . . . . .	1-9
1.3.1.1 Early Evidence . . . . .	1-9
1.3.1.2 Modern Evidence . . . . .	1-10
1.3.2 The Standard Halo Model . . . . .	1-17
1.3.3 The Usual Suspects . . . . .	1-18
1.3.3.1 WIMPs . . . . .	1-19
1.3.3.2 Axions . . . . .	1-20
1.3.3.3 Sterile Neutrinos . . . . .	1-20
1.3.4 Experimental Approaches . . . . .	1-24
1.3.4.1 WIMP Detection . . . . .	1-24
1.3.4.2 Sterile Neutrino Detection . . . . .	1-28
1.3.5 Theoretical Approaches . . . . .	1-29
1.3.6 Issues with $\Lambda$ CDM . . . . .	1-30
1.4 Neutrino Physics . . . . .	1-32
1.4.1 The Story so Far . . . . .	1-32
1.4.2 Unsolved Mysteries . . . . .	1-33
1.4.3 The Riddle of the Mass . . . . .	1-37
References . . . . .	1-39
<b>2 Simplified Models and Complementarity</b>	<b>2-1</b>
2.1 Introduction . . . . .	2-1
2.2 The Dark Sequential $Z'$ Portal . . . . .	2-2
2.2.1 The Model . . . . .	2-2

---

2.2.2	The Constraints . . . . .	2-3
2.2.2.1	Relic Abundance . . . . .	2-3
2.2.2.2	Direct Detection . . . . .	2-5
2.2.2.3	Indirect Detection . . . . .	2-6
2.2.2.4	Collider Searches . . . . .	2-7
2.2.2.5	Perturbativity . . . . .	2-9
2.2.3	The Results . . . . .	2-9
2.3	The Neutrino Portal . . . . .	2-13
2.3.1	The Method . . . . .	2-13
2.3.2	The Constraints . . . . .	2-18
2.3.2.1	Fermi-LAT Dataset . . . . .	2-18
2.3.2.2	H.E.S.S. Dataset . . . . .	2-21
2.3.3	The Results . . . . .	2-23
	References . . . . .	2-26
<b>3</b>	<b>Direct Detection of Sterile Neutrinos as Dark Matter</b>	<b>3-1</b>
3.1	Introduction . . . . .	3-1
3.2	Direct Detection in LXe Experiments . . . . .	3-2
3.3	Sterile Neutrinos and Bound Electrons . . . . .	3-3
3.4	Experimental and Statistical Details . . . . .	3-7
3.5	Results . . . . .	3-10
	References . . . . .	3-13
<b>4</b>	<b>Neutrino Masses in 2HDMs with a gauged <math>U(1)</math></b>	<b>4-1</b>
4.1	Introduction . . . . .	4-1
4.2	Two-Higgs Doublet Models . . . . .	4-2
4.3	Gauging $U(1)_X$ . . . . .	4-3
4.3.1	Anomaly Cancellation . . . . .	4-4
4.3.2	Neutrino Masses . . . . .	4-5
4.3.3	$Z'$ Strikes Again . . . . .	4-7
4.4	Phenomenological Constraints . . . . .	4-8
4.4.1	Higgs Physics . . . . .	4-10
4.4.2	Rare Meson Decays . . . . .	4-13
4.4.3	Atomic Parity Violation . . . . .	4-14
4.4.4	Neutrino Electron Scattering . . . . .	4-15
4.5	The Dark Matter Possibility . . . . .	4-18
	References . . . . .	4-21
<b>5</b>	<b>Summary and Outlook</b>	<b>5-1</b>
<b>A</b>	<b>Software Description</b>	<b>A-1</b>
A.1	Pythia . . . . .	A-1
A.2	GAMBIT & gamLike . . . . .	A-3
	References . . . . .	A-3

<b>B</b>	<b>Cross Section of Neutrinos with Bound Electrons</b>	<b>B-1</b>
B.1	Kinematic Variables . . . . .	B-1
B.2	The Roothan-Hartree-Fock Method . . . . .	B-3
	References . . . . .	B-5
<b>C</b>	<b>Theoretical Aspects of 2HDM</b>	<b>C-1</b>
C.1	Anomaly Cancellation . . . . .	C-1



# List of Figures

- 1.1 Comparison in sensitivity of the anisotropies measured by COBE, WMAP and Planck satellites with measurements done every ten years. . . . . 1-10
- 1.2 Temperature fluctuations of the CMB as a function of the multipole  $\ell$  as measured by Planck (red dots) in comparison with the best fit provided by the standard model of cosmology or  $\Lambda$ CDM (green curve, see section 1.3.6 for details about this model). The green area around the curve shows the predictions of all the variations of  $\Lambda$ CDM that best agree with the data. Credit to: ESA. 1-12
- 1.3 In blue and purple the results from the galactic surveys SDSS, CfA2 and 2dFGRS, while in red the corresponding results from the Millenium simulation with matching survey geometries and magnitude limits. Figure taken from [72]. . . . . 1-15
- 1.4 Hubble Space Telescope image of a cluster of galaxies called SDSS J1038+4849, depicting strong gravitational lensing. Credit to: NASA & ESA. . . . . 1-15
- 1.5 *Left panel:* The “bullet cluster” 1E0657-56. *Right panel:* the “baby bullet” MACSJ0025.4-1222. The X-ray emission of intra-cluster gas is shown in pink, while the total mass is shown in blue, using weak gravitational lensing that appears to coincide with the location of the galaxies in the cluster. Figure taken from [80]. . . . . 1-16
- 1.6 Composite image of the merging galaxy cluster Abell 520. Luminosity is shown in orange as measured by the Canada-France-Hawaii Telescope in Hawaii, hot gas is shown in green as detected by NASA’s Chandra X-ray Observatory and in blue the mass map of the cluster as measured by the Hubble Wide Field Planetary Camera 2 using weak lensing, that should be dominated by dark matter. Credit to: NASA, ESA, CFHT, CXO, M.J. Jee (University of California, Davis), and A. Mahdavi (San Francisco State University). . . . . 1-17
- 1.7 Large scale structure distribution simulation for a universe dominated by HDM (left plot) or CDM (right plot) in comparison with the observed distribution measured by CfA Survey. Figure taken from [98], reproduced from [95]. . . . . 1-19

---

1.8	Dark matter spectrum for a resonantly produced sterile neutrino with $m_S = 3$ keV as a function of $x = p/T$ . The dashed-dotted line represents the spectrum obtained through the Dodelson-Widrow Mechanism, while the dashed line is the Shi-Fuller contribution, with $L_\alpha = 16$ (see the text). Figure taken from [112], reproduced from [113]. . . . .	1-21
1.9	Depiction of the three kind of WIMP detection techniques. . . . .	1-25
1.10	Depiction of the kind of particles resulting of dark matter annihilation. . . . .	1-26
1.11	<i>Left panel:</i> Main decay channel of sterile neutrinos. <i>Right panel:</i> radiative decay of sterile neutrinos. . . . .	1-29
1.12	Scheme of the three different theoretical approaches. . . . .	1-30
1.13	Possible neutrino mass hierarchies. The flavour composition is indicated in the mass eigenstates as a function of the unknown phase $\delta_{CP}$ . Figure taken from [187]. . . . .	1-34
1.14	Quark level “lobster” diagram for $0\nu 2\beta$ decay, mediated by a Majorana neutrino. . . . .	1-35
1.15	<i>Left panel:</i> Bands for the value of the effective mass parameter as a function of the mass of the lightest neutrino, for NH (red band) and IH (green band). The present best experimental upper limits are shown in the blue band. <i>Right panel:</i> Present best upper limits, with uncertainty bars, on $\langle m_{\beta\beta} \rangle$ from experiments performed on each emitter element, as a function of their mass number $A$ . Figure taken from [192]. . . . .	1-36
2.1	Feynman diagrams relevant for dark matter annihilation. <i>Left panel:</i> the $Z'$ boson mediates $s$ -channel annihilations to SM fermions. <i>Right panel:</i> $t$ -channel decay to $Z'$ pairs. . . . .	2-4
2.2	Feynman diagram relevant for direct detection. The dark matter scattering off nucleons occurs via $t$ -channel $Z'$ exchange. . . . .	2-5
2.3	Feynman diagrams relevant for collider probes. <i>Left panel:</i> mono-jet searches for dark matter, where the $Z'$ decays invisibly with a jet being radiated from the initial state. <i>Right panel:</i> resonant production of the $Z'$ gauge boson. It is not sensitive to dark matter, but it restricts the $Z'$ mass, which has a great impact on this particular model. . . . .	2-7
2.4	Upper 95% CL limits on the $Z'$ production cross-section times branching ratio to two leptons of a single flavour as a function of $Z'$ pole mass, measured by ATLAS. Results are shown for the combined dilepton channel. The Sequential SM, relevant for this work, is shown as a black line. Figure taken from [16]. . . . .	2-8

- 
- 2.5 Exclusion limits for  $g_\chi = 0.1$ . The black solid curve outlines the region of parameter space with the correct relic density. From left to right: in blue dashed the parameter space excluded by Ice-Cube; the orange solid line represents the current bound from PICO; the green dashed line the current bound from LUX on SD scattering off neutrons with 129.5 kg-year exposure; the solid green line the projected bound from XENONIT on SD scattering off neutrons with 34 d×t of exposure; further right in light green, we show the projected sensitivity from XENONIT on SD scattering off neutrons with 2 y×t exposure; the region above the black dashed line delimits the non-perturbative regime; the red dashed curve depicts the parameter space excluded by LHC based on mono-jet data; blue vertical solid (dotted) lines delimit the current (projected) LHC exclusion regions derived from dilepton data. . . . . 2-10
- 2.6 Exclusion limits for  $g_\chi = 1$ . The black solid curve outlines the region of parameter space with the correct relic density. From left to right: in blue dashed the parameter space excluded by Ice-Cube; the orange solid line represents the current bound from PICO; the green dashed line the current bound from LUX on SD scattering off neutrons with 129.5 kg-year exposure; the solid green line the projected bound from XENONIT on SD scattering off neutrons with 34 d×t of exposure; further right in light green, we show the projected sensitivity from XENONIT on SD scattering off neutrons with 2 y×t exposure; the region above the black dashed line delimits the non-perturbative regime; the red dashed curve depicts the parameter space excluded by LHC based on mono-jet data; blue vertical solid (dotted) lines delimit the current (projected) LHC exclusion regions derived from dilepton data. . . . . 2-11
- 2.7 Exclusion limits for  $g_\chi = 4\pi$ . The black solid curve outlines the region of parameter space with the correct relic density. From left to right: in blue dashed the parameter space excluded by Ice-Cube; the orange solid line represents the current bound from PICO; the green dashed line the current bound from LUX on SD scattering off neutrons with 129.5 kg-year exposure; the green solid line the projected bound from XENONIT on SD scattering off neutrons with 34 d×t of exposure; further right in light green, we show the projected sensitivity from XENONIT on SD scattering off neutrons with 2 y×t exposure; the region above the black dashed line delimits the non-perturbative regime; the red dashed curve depicts the parameter space excluded by LHC based on mono-jet data; blue vertical dot-dashed (dotted) lines delimit the current (projected) LHC exclusion regions derived from dilepton data. . . . . 2-12

- 
- 2.8 Feynman diagrams for two-body decays of the right-handed neutrinos. . . . . 2-13
- 2.9 Gamma spectra for the annihilation of a dark matter particle with mass  $M_\chi = 100$  GeV (upper-panel) and  $M_\chi = 1000$  GeV (lower panel) into different final states. For simplicity we show just the case in which  $N$  mixes exclusively with  $\ell = e$ . Magenta and green curves represent the final states of  $b\bar{b}$  and  $W^+W^-$ . *Upper panel:* Orange and yellow curves account for annihilations into right-handed neutrinos with  $M_N = 90$  GeV and  $M_N = 10$  GeV respectively. *Lower Panel:* Orange and yellow curves account for annihilations into right-handed neutrinos with  $M_N = 500$  GeV and  $M_N = 50$  GeV respectively. . . . . 2-16
- 2.10 The energy spectrum for  $M_{DM} = 1$  TeV and  $M_N = 500$  GeV, for different final state leptons. One can see there is only a mild difference between them, with the final state  $\tau$  leading to harder gamma-ray yield, i.e. larger  $dN/dE$ , as expected since they lead to a relatively more efficient hadronization process. . . . . 2-17
- 2.11 Location of the dSphs listed in table 2.1 overlaid on a 4-year LAT counts map (for  $E > 1$  GeV). Those used in this analysis are shown as filled circles, while those not considered are shown as open circles. Figure taken from [26]. . . . . 2-20
- 2.12 Definition of the ROI (green) around the GC (black triangle), excluded area (yellow) and area used for background control (red). In particular the process for background subtraction for a particular telescope pointing position (star) is illustrated: the background control for pixel 0 is obtained from pixels 1 and 2, while pixel 3 is excluded. Each pixel has a size of  $0.02^\circ \times 0.02^\circ$ . Figure taken from [28]. . . . . 2-21
- 2.13 Reconstructed differential flux  $F_{Src/Bg}$ , weighted with  $E^{2.7}$  for better visibility, obtained for the source and background regions as defined in the fig. 2.12. Figure taken from [28]. . . . . 2-22
- 2.14 Upper limit on  $\langle\sigma v\rangle$  as a function of the dark matter mass ( $M_\chi$ ) for the electron right-handed neutrino final state. Blue curves represent the limits obtained using Fermi-LAT data, while red are those obtained using H.E.S.S. data. Solid, dashed and dot-dashed curves are for  $M_N = 10, 10^2, 10^3$  GeV respectively. The horizontal dotted line shows the thermal cross section  $\sim 3 \times 10^{-26} \text{ cm}^3 \text{ s}^{-1}$ . . . . . 2-24
- 2.15 Upper limit on  $\langle\sigma v\rangle$  as a function of the dark matter mass ( $M_\chi$ ) for the muon right-handed neutrino final state. Blue curves represent the limits obtained using Fermi-LAT data, while red are those obtained using H.E.S.S. data. Solid, dashed and dot-dashed curves are for  $M_N = 10, 10^2, 10^3$  GeV respectively. The horizontal dotted line shows the thermal cross section  $\sim 3 \times 10^{-26} \text{ cm}^3 \text{ s}^{-1}$ . . . . . 2-24



- 
- 2.16 Upper limit on  $\langle\sigma v\rangle$  as a function of the dark matter mass ( $M_\chi$ ) for tau right-handed neutrino final state. Blue curves represent the limits obtained using Fermi-LAT data, while red are those obtained using H.E.S.S. data. Solid, dashed and dot-dashed curves are for  $M_N = 10, 10^2, 10^3$  GeV respectively. The horizontal dotted line shows the thermal cross section  $\sim 3 \times 10^{-26}$  cm<sup>3</sup> s<sup>-1</sup>. . . . . 2-25
- 3.1 *Left panel:* Scheme of a TPC depicting the primary or scintillation signal ( $S1$ ) and the ionization or secondary signal ( $S2$ ). *Right panel:* Representation of the amplitude difference between ERs and NRs. Figure taken from [1]. . . . . 3-2
- 3.2 Event distribution in the discrimination parameter space  $\log_{10}(S2_b/S1)$  from 225 Live Days of XENON100 Data (black squares) as a function of the recoil energy (in keV) or the amplitude of the primary signal  $S1$  (in number of photoelectrons). The horizontal green dashed line rejects 99.75% of the ERs (upper region) from the NRs (lower region). The red and gray squares indicate the NR neutron calibration. Additional energy cuts are also displayed; more information can be found in the original source [6]. 3-3
- 3.3 Feynman diagrams for the interaction between sterile (anti)neutrinos and electrons. The NC diagrams are presented in the left side, while those in the right side represent the CC interactions. . . . . 3-4
- 3.4 Differential cross section of massive sterile neutrinos with free (dark green) and bound electrons (light colors) for  $m_S = 40$  keV and  $|U_{Se}|^2 = 5 \times 10^{-4}$ . The vertical dashed line represents the lower threshold of  $E_{Th} = 1$  keV (see next section 3.4). . . . . 3-7
- 3.5 *Upper panel:* Acceptance function for the XENON100 experiment, evaluated on calibration data. *Lower panel:* Conversion function between the recorded number of PEs and recoil energy (in keV) for XENON100. Both functions reproduced from [9]. . . 3-9
- 3.6 Differential number of events for bound electrons for  $m_S = 40$  keV and  $|U_{Se}|^2 = 5 \times 10^{-4}$  in XENON1T (blue) and estimated background  $F_b$  (red). The vertical dashed line represents lower threshold of  $E_{Th} = 1$  keV. . . . . 3-9

---

3.7	<i>Light Green</i> : Sensitivity on sterile neutrino WDM parameters for XENON100 as a function of $m_S$ and $ U_{Se} ^2$ . The contours delimit 90% and 99.9% C.L. <i>Dark Green</i> : Equivalent for XENONIT; <i>Blue</i> : Equivalent for DARWIN; <i>Purple</i> : Current limits from analysis of $\beta$ spectrum of different radioisotopes [18, 19]; <i>Black</i> : Expected statistical sensitivity of a modified KATRIN setup (Fig. 11 in [20]); <i>Red dashed</i> : Limits coming from $0\nu\beta\beta$ experiments [21]; <i>Magenta dashed</i> : Upper and lower bounds from Dodelson-Widrow production of DM [22]; Orange solid (and dot-dashed): Excluded area for production in case of a low reheating temperature (LRT) of $T_R = 5$ MeV ( $T_R = 10$ MeV) [23]; <i>Yellow</i> : Constraint from $X$ -ray searches [24, 25]; <i>Turquoise</i> : limit on $ U_{S\mu} ^2 +  U_{S\tau} ^2$ if the sterile neutrino does not couple to electron neutrinos and only has neutral currents. . . . .	3-11
4.1	<i>Left panel</i> : Forbidden tree-level FCNI in the SM. <i>Right panel</i> : GIM-suppressed loop-level FCNI in the SM. . . . .	4-2
4.2	Branching ratios as a function of the $Z'$ mass for several of the $U(1)_X$ models under study. . . . .	4-9
4.3	Feynman diagram for Higgs production at LEP, followed by its invisible decay. . . . .	4-11
4.4	Upper limits from invisible Higgs decay searches translated to the light Higgs mass $m_h$ . Figure taken from [21]. . . . .	4-11
4.5	Feynman diagrams for neutrino-electron scattering. The upper diagrams represent the SM contribution, while the lower diagrams shows the contribution of $Z'$ . . . . .	4-16
4.6	Constraints on $g_{B-L}$ using neutrino-electron scattering experiments. . . . .	4-17
4.7	Feynman diagram showing the $Z'$ portal connecting the dark matter particle $\chi$ and SM fermions $f$ . . . . .	4-19
4.8	Dark matter constraints summary for $M_\chi = 50$ MeV and $g_{B-L} = 1$ . . . . .	4-19
A.1	Gamma spectra for the annihilation of a dark matter particle with mass $M_\chi = 785$ GeV for 14 different values of $M_N$ , going from $M_N = 1$ GeV (red to the right) to $M_N = 545$ GeV (blue to the left). For simplicity we show just the case in which $N$ mixes exclusively with $\ell = e$ . . . . .	A-2

# List of Tables

1.1	Transformations of the chiral fields under the SM group for the three generations, $n = 1, 2, 3$ . . . . .	1-6
2.1	Milky Way dSphs observed by Fermi-LAT, their distance from Earth and associated $J$ -factors. The upper block comprises those used for the analysis performed in this section. . . . .	2-19
3.1	Binding energy $\varepsilon$ for the different electronic states $t$ in xenon. Values taken from [11]. . . . .	3-6
4.1	2HDMs classified depending on the parities under $Z_2$ of the fermionic and scalar content of the model. . . . .	4-4
4.2	Type-I 2HDM with an additional gauged $U(1)_X$ symmetry and the quantum numbers of the particle content of the model under this symmetry. The upper block describe models that can explain neutrino masses and forbid FCNI, while the lower block can achieve just the second. . . . .	4-6
4.3	Scalar interactions in the type-I 2HDM. . . . .	4-10
4.4	List of experimental limits on the branching ratio of the SM Higgs. . . . .	4-12
4.5	Existing (upper block) and projected (lower block) constraints on the kinetic mixing parameter as a function of the mass mixing parameter $\delta$ and the $U(1)_X$ boson mass $M_{Z'}$ . All masses in MeV. Table taken from [30]. . . . .	4-15
4.6	Neutrino-electron scattering experiments used to constrain $g_{B-L}$ in fig. 4.6. . . . .	4-16



# List of Acronyms

## #

$0\nu 2\beta$  Neutrinoless Double Beta  
2HDM Two Higgs-Doublet Models

## A

ALP Axion Like Particle  
APV Atomic Parity Violation

## B

BAU Baryon Asymmetry of the Universe  
BBN Big Bang Nucleosynthesis  
BSM Beyond Standard Model  
BTF Baryonic Tully Fisher Relation

## C

CC Charged Current  
CDM Cold Dark Matter  
CKM Cabibbo-Cobayashi-Maskawa  
CMB Cosmic Microwave Background



ISM Inter Stellar Medium

## L

LHC Large Hadron Collider  
LSB Low Surface Brightness  
LSS Last Scattering Surface  
LXe Liquid Xenon

## N

NC Neutral Current  
NFC Natural Flavour Conservation  
NFW Navarro-Frenk-White  
NH Normal Hierarchy  
NR Nuclear Recoil

## P

PE Photoelectron  
PMNS Pontecorvo Maki Nakagawa Sakata  
PMT Photomultiplier Tube

## Q

QCD Quantum Chromodynamics  
QED Quantum Electrodynamics  
QFD Quantum Flavourdynamics

## R

RHF Roothan-Hartree-Fock  
ROI Region of Interest

**S**

SD	Spin Dependent
SDSS	Sloan Digital Sky Survey
SHM	Standard Halo Model
SI	Spin Independent
SM	Standard Model
SSB	Spontaneous Symmetry Breaking
SSM	Sequential Standard Model
SUSY	Super Symmetry

**T**

TPC	Time Projection Chamber
TS	Test Statistic

**U**

UV	Ultra Violet
----	--------------

**V**

vev	vacuum expectation value
-----	--------------------------

**W**

WDM	Warm Dark Matter
WIMP	Weakly Interacting Massive Particle







*As areas of knowledge grow, so too do the perimeters of ignorance.*

Neil deGrasse Tyson

# 1

## Introduction

### 1.1 The Current State of Affairs

Much has been said about the beauty and the predictability of the Standard Model (SM), the framework that describes all known elementary particles and its possible interactions. In particular Quantum Electrodynamics (QED), an essential ingredient of it, stands out as one of the most accurate physical theories ever constructed, predicting for example a value for the anomalous magnetic moment of the electron that agrees with experiments at the order of parts per trillion [1]. On the other hand, much more has been debated about what are considered “open questions in high energy physics” and the necessity of an ultraviolet complete model that addresses these issues and from which the SM can be seen as a low energy effective theory. The mentioned problems can—arguably—be divided in two categories: those that arise from aesthetic reasons and those from puzzling measurements.

On the first group we find for example *the flavour problem*, *the strong CP problem* and *the hierarchy problem*. The flavour problem addresses the fact that the SM consists of three copies of the same particles that just have different masses, and the particular pattern of the mixing angles in the quark and lepton sectors [2–4]. It tries to look for an underlying reason behind this particular design, however nothing ensures that this ulterior motive actually exists. The strong *CP* problem originates from the fact that Quantum Chromodynamics (QCD) allows a term in the Lagrangian that could break Charge (*C*) and Parity (*P*).

This term, parametrized by an angle  $\theta$  would generate a non-zero value for the electric dipole moment of the neutron. The null results from experiments looking for this phenomenon constrain this angle to  $\theta < 10^{-9}$  [5, 6] which is seen as *unnaturally* small or fine-tuned. Finally, a key aspect of the hierarchy problem is usually associated with the fact that the mass of the Higgs boson ( $m_H = 125.09 \pm 0.32$  GeV [7]) receives large loop corrections related to the scale at which the SM description is believed to fail. If this scale is the so-called Planck scale ( $\Lambda_{\text{Planck}} \sim 10^{19}$  GeV), said corrections would be 16 orders of magnitude bigger than the measured value. For this to happen it is expected that a very fine cancellation between the bare mass and the quantum corrections would lead to the measured Higgs mass. This cancellation is deemed unnatural. The most widely accepted solution to this problem is to consider that a new symmetry appears, and hence new particles, at a scale much smaller than  $\Lambda_{\text{Planck}}$ . If this scale is  $\Lambda \sim 10$  TeV, a fine tuning around one part in 100 is still required [8] and as the Large Hadron Collider (LHC) has probed directly scales in the TeV scale without finding any evidence of physics beyond the SM, the proposed solution is getting under certain tension.

Now, when we talk about *naturalness*, we refer to the principle described by 't Hooft in 1979 [9]: “at any energy scale  $\mu$ , a physical parameter or set of parameters  $\alpha_i(\mu)$  is allowed to be very small only if the replacement  $\alpha_i(\mu) = 0$  would increase the symmetry of the system”. This has been an important guiding principle for particle physicists for decades (even before it was formally enunciated by 't Hooft), however it has not produced many results, excepts perhaps the observation of a lack of flavour changing neutral currents in the SM that led to the prediction of the charm quark through the GIM mechanism [10]. It has been recently argued [11] that the reason behind this is that naturalness is ill-defined because we do not have a probability distribution on parameter space, neither at low energies nor at high energies. Then, it is impossible to know how unlikely it is that a parameter of the theory, like the  $CP$  angle  $\theta$  or the difference between the Higgs bare mass and its quantum corrections, is really small in comparison to  $\mathcal{O}(1)$ .

Due to the mentioned reasons we qualify the aforementioned problems as merely of an aesthetic nature and we will focus in this thesis to one related to the second category outlined before: the dark matter problem. Before describing the nature of this open question, it is worth to mention where should the neutrino problem be put, as it will also play an important role. It can be argued that it is somehow midway between the two categories, depending on the specific aspect of it. For example the discovery of neutrino oscillations was certainly a puzzling measurement, because it implies that neutrinos are massive particles a fact that the SM, built as it is, cannot account for. However, merely inserting right-handed neutrinos and generating their masses in the same way as for the

rest of the fermions of the SM is possible, even if it requires very small Yukawa couplings. This mechanism is usually considered unsatisfactory for the same reasons of aesthetics mentioned before. Due to this, alternative mechanisms have been suggested, the most famous of which is the so-called seesaw mechanism.

In this chapter we outline the theoretical foundations of the SM, stressing the important role that symmetries have played in its development; present the evidence that has led to the so-called dark matter problem and the possibilities to solve it; and finally consider some interesting aspects of neutrino physics that will be linked to dark matter in the next chapters.

## 1.2 The Area of Knowledge: The Standard Model

### 1.2.1 The Dawn of the SM

In this subsection we present the SM from a historical point of view to highlight how the concept of symmetry has been a guiding principle since its first stages. Around the 50's there was a growing feeling of disappointment in the community of physicists trying to elucidate the laws of elementary particles. This was due to the fact that, after the recent undeniable success of QED, when they tried to apply the same techniques to the four-fermion theory of weak interactions, they realised that it was plagued with unremovable infinities. On the other hand, the theory of strong interactions was in fact renormalizable, but no practical calculations could be done with it because perturbation theory was rendered useless due to the strength of its interactions. On top of this, experiments pointed to the inescapable truth that many of the symmetries proposed in particle physics up to that point were approximate at best: isotopic spin symmetry [12, 13], strangeness [14] and even spacetime symmetries like  $P$  and  $PT$  (parity and time) were found to be violated [15, 16]. Later  $CP$  would follow the same destiny [17].

According to Steven Weinberg [18], one of the most important ideas that shaped the SM as we currently know it is that of gauge symmetries. Despite the fact that QED, developed in the 30's, can be regarded as a  $U(1)$  gauge theory, it was not originally proposed as such. And then, it was not until 1954 that the concept gained strength, when Yang and Mills [19] trying to provide an explanation for strong interactions, extended the concept of gauge theories to non-abelian groups. Due to self-interactions coming from the non-abelian group on which the theory was based, it had some original success, but soon it was realised that the gauge bosons must be massless, and that such particles should have been appeared in experiments. The solution came in 1964 when the idea of spontaneously broken symmetries was discovered by Higgs [20] and independently

by Brout and Englert [21]: there might be symmetries of the Lagrangian that are not symmetries of the vacuum. Looking for a way to evade the Goldstone theorem [22, 23] that establishes that for every spontaneously broken symmetry there must be a massless scalar, Higgs realised that if the symmetry was local, the Goldstone boson would become the helicity-zero part of a gauge boson, which in turns gets a mass. These ideas were applied by Weinberg [24] in 1967 and independently by Salam the next year [25] to the electroweak theory, based on the gauge group  $SU(2) \times U(1)$ , whose spontaneous breakdown would make the weak gauge bosons massive (called  $W$  and  $Z$  bosons), while at the same time leaving a massless photon behind. The theory resulted to be quite predictive as the masses and interactions of the  $W$  and  $Z$  depended on just a few parameters: a vacuum expectation value (vev), a gauge coupling and an angle today called the Weinberg angle  $\theta_W$ . It also predicted the existence of a new massive scalar, called the Higgs boson. Its couplings were known, but its mass was a free parameter, which explains why it took 45 years for it to be finally found, in 2012 at the Large Hadron Collider [26, 27].

The theory of strong interactions followed the electroweak theory after the renewed interest in Yang-Mills theories. However its origins based on symmetries are dated a bit back, specifically to the early 60's with the discovery of the *Eightfold Way* by Gell-Mann [28] and Ne'eman [29] who, based on an approximate  $SU(3)$  symmetry managed to find structure in the growing zoo of hadrons constantly being discovered. Later, in 1964, Gell-Mann [30] and Zweig [31, 32] proposed that this pattern can be understood if one assumes that these particles are not fundamental, but bound states of three constituents that Gell-Mann called *quarks* (Zweig named them *aces*, but it seems that his proposed name was less catchy). For some years this proposal was considered mere speculation as experiments failed to provide evidence of the direct observation of quarks. It also was conflicting, as quarks had to be fermions, but some hadrons should be composed of three identical particles, a fact forbidden by Fermi statistics. This led to several authors propose that if the quark model had to be taken seriously, they must carry a new quantum number that Gell-Mann later called colour. It was not until 1973 that the mystery of the non-observation of quarks was solved independently by Gross and Wilczek [33] and Politzer [34] who discovered the property of asymptotic freedom: in non-abelian gauge theories the running of the coupling constant goes to zero as the energy goes to infinity. This also explained the Bjorken scaling, proposed in 1968 [35] and observed at SLAC the next year [36]. As it was already known that each different quark can come in three colours, it was natural to take the gauge symmetry group as  $SU(3)$ , and hence quantum chromodynamics (QCD) was born. This symmetry was originally thought to be spontaneously broken, which would explain why its gauge bosons—called gluons—have not been measured in direct analogy to the elec-

troweak interaction. But soon afterwards a number of authors [37–39] arrived at the same conclusion: the symmetry is not broken and the gluons are indeed massless, however they carry colour in the same way quarks do and coloured particles can never be isolated. The fact that colour is trapped has never been formally proven and the Cray Mathematics Institute offers a million dollar prize for the proof of a generalized version of it.

After this very brief historical summary, we are in conditions to tackle the more formal aspects of the SM symmetry group.

### 1.2.2 The SM Symmetry Group

The Standard Model is a quantum field theory based on the group

$$G_{\text{SM}} = SU(3)_c \times SU(2)_L \times U(1)_Y, \quad (1.1)$$

where the subscripts are not related with group properties, but with the charge nature of the subgroup:  $c$  stands for colour,  $L$  refers to the left-chiral property of the coupling in  $SU(2)$ , while  $Y$  denotes the weak hypercharge. QCD is mediated by eight massless gauge bosons called glouns  $G_a$  (with  $a = 1, \dots, 8$ ), which correspond to the eight generators of  $SU(3)$ , and they affect coloured particles like quarks. The electroweak theory, sometimes called quantum flavourdynamics (QFD) is a chiral theory. The non-abelian part,  $SU(2)$ , acts only on left-handed fermions (quarks and leptons) via its gauge bosons  $W_i$  ( $i = 1, 2, 3$ ) while the abelian part,  $U(1)$ , is also chiral acting on left and right-handed fermions with different charges via its gauge boson  $B$ . After spontaneous symmetry breaking (SSB),  $SU(2)_L \times U(1)_Y$  is broken down to  $U(1)_{em}$ , which describes QED and where the massless photon results from a linear combination of  $B$  and  $W_3$ , while an orthogonal combination results in the massive  $Z$ , mediating neutral currents. Charge currents are mediated by the massive  $W^\pm$  which are combinations of  $W_1$  and  $W_2$ . During SSB fermions acquire mass (with the exception maybe of neutrinos). Additionally, a massive scalar appears in the spectrum (the Higgs boson), while QCD remains unbroken.

The SM Lagrangian can be split according to the different sectors

$$\mathcal{L}_{\text{SM}} = \mathcal{L}_{\text{gauge}} + \mathcal{L}_{\text{fermions}} + \mathcal{L}_{\text{Higgs}} + \mathcal{L}_{\text{Yuk}}, \quad (1.2)$$

which refer to the gauge, fermion, Higgs and Yukawa sectors respectively. Additional terms for gauge-fixing and ghosts will not be discussed here. The gauge sector consists of

$$\mathcal{L}_{\text{gauge}} = -\frac{1}{4}G_{\mu\nu}^a G^{\mu\nu a} - \frac{1}{4}W_{\mu\nu}^i W^{\mu\nu i} - \frac{1}{4}B_{\mu\nu} B^{\mu\nu}, \quad (1.3)$$

	names	$SU(3)_c$	$SU(2)_L$	$U(1)_Y$
quarks	$Q_{nL} = \begin{bmatrix} u_n \\ d_n \end{bmatrix}_L$	<b>3</b>	<b>2</b>	$\frac{1}{6}$
	$u_{nR}$	$\bar{\mathbf{3}}$	<b>1</b>	$\frac{2}{3}$
	$d_{nR}$	$\bar{\mathbf{3}}$	<b>1</b>	$-\frac{1}{3}$
leptons	$L_{nL} = \begin{bmatrix} e_n \\ \nu_n \end{bmatrix}_L$	<b>1</b>	<b>2</b>	$-\frac{1}{2}$
	$e_{nR}$	<b>1</b>	<b>1</b>	$-1$

Table 1.1: Transformations of the chiral fields under the SM group for the three generations,  $n = 1, 2, 3$

which describes the kinetic terms of the gauge bosons encoded in the field strength tensors

$$\begin{aligned}
G_{\mu\nu}^i &= \partial_\mu G_\nu^a - \partial_\nu G_\mu^a - g_s f_{abc} G_\mu^b G_\nu^c, & \text{with } a, b, c = 1, \dots, 8 \\
W_{\mu\nu}^i &= \partial_\mu W_\nu^i - \partial_\nu W_\mu^i - g \epsilon_{ijk} W_\mu^j W_\nu^k, & \text{with } i, j, k = 1, 2, 3 \\
B_{\mu\nu} &= \partial_\mu B_\nu - \partial_\nu B_\mu,
\end{aligned} \tag{1.4}$$

where  $g_s$  and  $g$  are the coupling constants and  $f_{abc}$  and  $\epsilon_{ijk}$  the structure constants of  $SU(3)$  and  $SU(2)$  respectively, and accompany the terms with the three and four-point self interactions for  $G^a$  and  $W^i$ .

The fermionic content of the SM and their transformations under  $G_{\text{SM}}$  can be seen in table 1.1.

The kinetic terms of these particles and their interactions with the gauge fields are given by

$$\mathcal{L}_{\text{fermions}} = \sum_{n=1}^3 (\bar{Q}'_{nL} i \not{D} Q'_{nL} + \bar{L}'_{nL} i \not{D} L'_{nL} + \bar{u}'_{nR} i \not{D} u'_{nR} + \bar{d}'_{nR} i \not{D} d'_{nR} + \bar{e}'_{nR} i \not{D} e'_{nR}), \tag{1.5}$$

where the index  $n$  takes into account the three different generations and  $\not{D} = \gamma_\mu D^\mu$  with  $D^\mu$  the covariant derivative given by

$$D^\mu = \partial_\mu + ig_s \frac{Q_s \lambda^a}{2} G_{a\mu} + ig \frac{I_3^W \sigma^i}{2} W_{i\mu} + ig' \frac{Y^W}{2} B_\mu, \tag{1.6}$$

where  $Q_s$  is a charge with a value of one for quarks and zero for leptons,  $\lambda^a$  are the eight Gell-Mann matrices, group generators of  $SU(3)$ ,  $I_3^W$  the third component of the weak isospin,  $\sigma^i$  the three pauli matrices, group generators of



$SU(2)$ ,  $g'$  the coupling constant of  $U(1)$  and  $Y^W$  the weak hypercharge. The electric charge of a given particle is related to the weak isospin and hypercharge through the Gell-Mann-Nishijima formula [14, 40, 41]

$$Q = I_3^W + \frac{1}{2}Y^W. \quad (1.7)$$

In eq. (1.5) we have labelled the fermions with primes ( $\prime$ ) to emphasize that these are weak eigenstates, having definite gauge transformation properties under  $SU(2)$  that forbid mass terms. In order to obtain the mass eigenstates that we observe in nature, the theory has to undergo SSB through the Brout-Englert-Higgs mechanism.

In the scalar or Higgs sector we find

$$\mathcal{L}_{Higgs} = (D_\mu \phi^\dagger)(D^\mu \phi) - V(\phi^\dagger \phi), \quad (1.8)$$

where  $\phi = \begin{bmatrix} \phi^+ \\ \phi^0 \end{bmatrix}$  is a complex Higgs scalar. The Higgs potential is restricted by the symmetry to

$$V(\phi^\dagger \phi) = +\mu^2 \phi^\dagger \phi + \lambda(\phi^\dagger \phi)^2, \quad (1.9)$$

where the desired SSB is obtained for  $\mu^2 < 0$  and  $\lambda$  describes the quartic interactions. For the vacuum to be stable we also require  $\lambda > 0$ . If the neutral component  $\phi^0$  acquires a non-zero vev,  $\langle \phi^0 \rangle = v$ , the electroweak symmetry  $SU(2)_L \times U(1)_Y$  breaks down to electromagnetism  $U(1)_{em}$  and gives mass to the  $W$  and  $Z$  gauge bosons

$$M_W = \frac{gv}{2}, \quad M_Z = \frac{\sqrt{g^2 + g'^2}v}{2} = \frac{M_W}{\cos \theta_W}, \quad (1.10)$$

where the Weinberg angle is defined as

$$\sin \theta_W = \frac{g'}{\sqrt{g^2 + g'^2}}, \quad \cos \theta_W = \frac{g}{\sqrt{g^2 + g'^2}}. \quad (1.11)$$

The Higgs vev determines the so-called weak scale, which is measured to be [ref]

$$v = 2M_W/g = (\sqrt{2}G_F)^{-1/2} \simeq 246.22 \text{ GeV}, \quad (1.12)$$

where  $G_F$  is the Fermi constant whose value can be determined through the muon lifetime [ref]

$$G_F = 1.1663787(6) \times 10^{-5} \text{ GeV}^{-2}. \quad (1.13)$$

The last term in eq. (1.2) represents the Yukawa couplings between the Higgs doublet and the fermions

$$\mathcal{L}_{Yuk} = - \sum_{m,n=1}^3 (y_{mn}^u \bar{Q}'_{mL} \tilde{\phi} u'_{nR} + y_{mn}^d \bar{Q}'_{mL} \phi d'_{nR} + y_{mn}^e \bar{L}'_{mL} \phi e'_{nR}) + h.c., \quad (1.14)$$

where we have defined

$$\tilde{\phi} := i\sigma^2\phi^\dagger = \begin{bmatrix} \phi^{0\dagger} \\ -\phi^- \end{bmatrix} \quad (1.15)$$

and  $y_{mn}^u, y_{mn}^d, y_{mn}^e$  are arbitrary Yukawa matrices that determine the fermion masses and mixings. The mass matrices are given by

$$M_{mn}^f = y_{mn}^f \frac{v}{\sqrt{2}}, \quad (1.16)$$

with  $f = u, d, e$  a superscript indicating the family. In general,  $M_{mn}^f$  needs not to be diagonal, Hermitian or symmetric. In order to obtain the physical states, we need to perform a bi-unitary transformation

$$V_L^{f\dagger} M^f V_R^f = M_D^f = \begin{bmatrix} m_1^f & 0 & 0 \\ 0 & m_2^f & 0 \\ 0 & 0 & m_3^f \end{bmatrix}, \quad (1.17)$$

with  $m_1^f, m_2^f, m_3^f$  the physical masses of the three generations of the family  $f$ . This bi-unitary transformation leads, in the quark sector, to a mixing of different quark flavours described by the Cabibbo-Kobayashi-Maskawa (CKM) matrix originally introduced in 1973 by Makoto Kobayashi and Toshihide Maskawa [42], extending to three quark generations the previous two-quark description by Nicola Cabibbo [43], in order to explain the  $CP$  violation measured in the kaon system in 1964 [17]. The so-called *standard* parametrization uses three Euler angles  $(\theta_{12}, \theta_{23}, \theta_{13})$  and a phase responsible for  $CP$  violation  $\delta_{13}$

$$V_{\text{CKM}} := (V_L^u)^\dagger V_R^d = \begin{bmatrix} c_{12}c_{13} & s_{12}c_{13} & s_{13}e^{-i\delta_{13}} \\ -s_{12}c_{23} - c_{12}s_{23}s_{13}e^{i\delta_{13}} & c_{12}c_{23} - s_{12}s_{23}s_{13}e^{i\delta_{13}} & s_{23}c_{13} \\ s_{12}s_{23} - c_{12}c_{23}s_{13}e^{i\delta_{13}} & -c_{12}s_{23} - s_{12}c_{23}s_{13}e^{i\delta_{13}} & c_{23}c_{13} \end{bmatrix}, \quad (1.18)$$

where  $s_{ij} := \sin\theta_{ij}$  and  $c_{ij} := \cos\theta_{ij}$ .

In the lepton sector this mixing was not originally needed, as neutrinos were thought to be massless. After the discovery of their small masses (see section 1.4), an analogous matrix was introduced. It is the so-called Pontecorvo-Maki-Nakagawa-Sakata (PMNS) matrix that describes neutrino mixings.

## 1.3 The Perimeter of Ignorance: Dark Matter

### 1.3.1 The Evidence

#### 1.3.1.1 Early Evidence

It is a common belief that the first time the term “dark matter” was used was by Franz Zwicky in 1933. However, its history can be traced earlier than this. The term *matière obscure* was coined by Henri Poincaré in 1906 referring to the “dark stars” that Lord Kelvin proposed existed in our Milky Way (MW), following discussions that were present during most of the second half of the 19th century in the community of astronomers about the possibility of dark objects that were not possible to observe through the common techniques at the time [44]. Interestingly enough, the methods proposed by Kelvin of treating the stars in the MW as a gas of particles, establishing a relationship between the size of the system and its velocity dispersion, is one of the methods used nowadays to measure the influence of dark matter. This idea was rediscovered in 1915 by Ernst Öpik and in 1922 by Jacobus Kapteyn concluding however that the presence of dark matter in our galaxy was negligible. In 1932 Jan Oort refined Kapteyn’s approach and concluded that “the total mass of nebulous or meteoric matter near the sun is less than  $0.05M_{\odot}$ , or  $3 \times 10^{-24} \text{ g cm}^{-3}$ ; it is probably less than the total mass of visible stars, possibly much less.” [45].

In 1931 Edwin Hubble and Milton Humason analysed the redshifts of several galactic clusters and found that the Coma Cluster exhibited an abnormally large velocity dispersion [46]. Franz Zwicky deepened this work applying the virial theorem to the Coma cluster, following the steps of Kelvin and Poincaré. He found out through this method that the velocity dispersion of the cluster should have been 80 km/s, when the measured value was close to 1000 km/s, concluding that “If this would be confirmed, we would get the surprising result that dark matter is present in much greater amount than luminous matter.” [47, 48]. This problem intensified in the next decades and by 1954 the number of systems showing large mass-to-light ratios ( $M/L$ ) had grown to 10, as compiled by Martin Schwarzschild [49]. Even if the proposed solution of dark matter was far from reaching a consensus, other alternatives were slowly being ruled out leaving astronomers in a state of confusion.

During the 60’s, Kent Ford developed an extremely sensitive spectrometer that he and Vera Rubin used to track the motion of the Andromeda Galaxy. This work was published in 1970 [50] and revealed that the stars at the outer part of M31 were moving almost as fast as those in the inner part, which was strange as the visible mass could not account for the gravity needed to bind such a system. The conclusion that large amounts of unseen matter in the outer region of spiral galaxies were needed to make them stable started to gain more

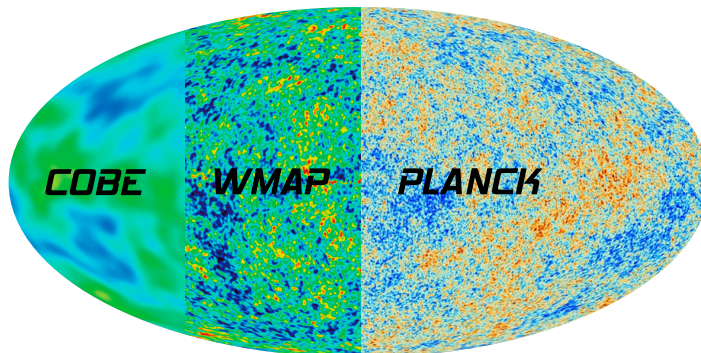


*Figure 1.1: Comparison in sensitivity of the anisotropies measured by COBE, WMAP and Planck satellites with measurements done every ten years.*

strength, as that same year Ken Freeman published a work [51] in which he observed that the rotation curves of M33 and NGC 300 peaked at larger radii than predicted. Even more, in 1973 Morton Roberts and Arnold Rots published the analysis of the movement of three spiral galaxies concluding that they must be larger than indicated by the usual photometric measurements, pointing to the first hints of a dark matter halo [52]. This idea was formally put forward by two independent groups in 1974, Einasto, Kaasik, and Saar [53] and Ostriker, Peebles and Yahil [54], which helped to convince the community about the existence, in spiral galaxies, of about ten times more dark, hidden matter than what can be accounted by visible stars. The cited works paved the way for the dark matter revolution that would start in the 80's with many particle physicists becoming increasingly interested in the problem, which would lead by the end of that decade to establishing what we consider today the common lore: the missing matter consists of (one or more) species of fundamental particles that have not been measured yet.<sup>1</sup> Before exploring the most popular candidates, we will briefly review the modern evidence supporting the idea of dark matter.

### 1.3.1.2 Modern Evidence

#### ★ The Cosmic Microwave Background

In 1948 George Gamow and Ralph Alpher (in the famous Alpher, Bethe and Gamow paper) [55] and Robert Herman [56] predicted the existence of a mi-

<sup>1</sup>As an alternative explanation to dark matter, theories of modified gravity still remain viable options. They will not be discussed in this thesis.

crowave background radiation and estimated its temperature to be between 5K and 50K while working out the details of chemical abundances in the early stages of the universe’s evolution (see ★ **Big Bang Nucleosynthesis** for details). Completely unaware of this prediction, Arno Penzias and Robert Wilson were working at Bell Labs in 1964, trying to measure radio transmission from communication satellites, when they measured a persistent isotropic 3.5K noise [57]. After talking to Robert H. Dicke, Jim Peebles and David Wilkinson [58] the conclusion was unavoidable: they had measured a remnant of the big bang, burying the “steady state model” forever and starting a new chapter for cosmology.

The Cosmic Microwave Background (CMB) is the faint glow of electromagnetic radiation left behind after the period of recombination, and it is by definition the oldest light that we can measure directly. The universe was a hot plasma of charged particles during its first 380.000 years (or redshift  $z = 1090$ ) and no photon could have escaped the constant scattering off electrons and protons. However, once the universe cooled down electrons were able to be bound to protons, creating neutral hydrogen and allowing photons to escape their electromagnetic grip by making the medium transparent. This period of photon decoupling left behind an isotropic relic radiation whose original wavelength has been shifted towards the microwave regime due to the expansion of the universe and it reaches us today as a thermal black body spectrum at  $T_{\text{CMB}} \simeq 2.72548 \pm 0.00057$  K [59].

The most direct way in which the CMB points us towards the existence of dark matter is through its anisotropies. Despite it being extremely uniform, small temperature variations appear at the order of  $30 \pm 5$   $\mu\text{K}$  (or  $\Delta T/T \sim \mathcal{O}(10^{-6})$ ), first detected by the COBE satellite in 1992 [60], later by the NASA Wilkinson Microwave Anisotropy Probe (WMAP) in 2003 [61] and finally by the Planck Satellite in 2013 [62]. In fig. 1.1 we contrast the sensitivities of these probes.

In order to analyse the CMB power spectrum, we decompose the angular temperature fluctuations into spherical harmonics

$$\delta T(\theta, \phi) = \sum_{\ell, m} a_{\ell m} Y_{\ell}^m(\theta, \phi), \quad (1.19)$$

where  $a_{\ell m}$  are complex coefficients. We can further define the angular power spectrum as

$$C_{\ell} = \langle |a_{\ell m}|^2 \rangle \quad (1.20)$$

which does depend on the multipole  $\ell$  (the inverse of the angle) but not on the directional parameter  $m$ , due to the CMB being isotropic. Finally, it is customary to plot  $\ell(\ell + 1)C_{\ell}$  because it gives the total power in the multipole  $\ell$ . In fig. 1.2 we show the power spectrum of the CMB as obtained by the Planck collaboration [62].

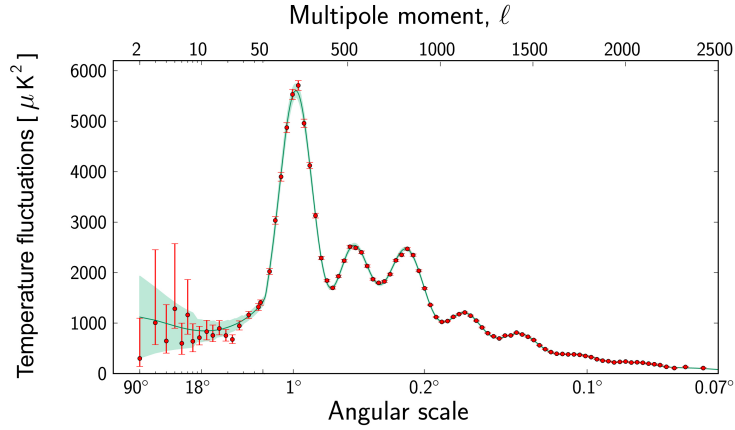


*Figure 1.2: Temperature fluctuations of the CMB as a function of the multipole  $\ell$  as measured by Planck (red dots) in comparison with the best fit provided by the standard model of cosmology or  $\Lambda$ CDM (green curve, see section 1.3.6 for details about this model). The green area around the curve shows the predictions of all the variations of  $\Lambda$ CDM that best agree with the data. Credit to: ESA.*

There are many physical effects that generate the temperature fluctuations in the CMB, but those that happened earlier are probably the most important as they are evidence of the last scattering surface (LSS). Considering a gravitational potential  $\phi$ , a radial peculiar velocity  $v_r$  and a density fluctuation  $\delta$ , then

1. photons will experience gravitational redshift if their last scattering happened in a potential well ( $\phi < 0$ ).
2. photons will be more energetic if they originate from an overdense region ( $\delta > 0$ ), because of the higher temperature.
3. photons interacting the last with matter whose peculiar velocity recede from us ( $v_r > 0$ ) will experience a Doppler redshift.

This can be summarized in the following equation

$$\frac{\Delta T}{T}(\vec{r}) = \phi(\vec{r}) + \frac{1}{3}\delta(\vec{r}) - \hat{r} \cdot \vec{v}(\vec{r}), \quad (1.21)$$

where  $\vec{r}$  is the comoving distance to the LSS vector. As overdense regions coincide with the potential wells, the first two effects partially cancel each other. In fact, for large scales it happens that  $\delta \approx -2\phi$  and then they combine to  $\phi/3$ : this is the Sachs-Wolfe effect [63] which is responsible for the flattening at the

left side of fig. 1.2. On the other hand, on small scales, the so-called acoustic oscillations generate fluctuations in  $\phi$ ,  $\delta$  and  $v_r$  that are necessary to take into account. A full mathematical description is beyond the scope of this introduction, but the physical phenomenon is easier to grasp. If we model protons and photons before decoupling as a photon-baryon fluid, the following cycle occurs: as soon as it falls into a gravitational potential it starts to compress until, due to internal pressure the fluid expands outward. This expansion stops when gravity wins over internal pressure and the cycle starts again. When photons emerge from the LSS, they will have different temperatures depending on their specific sequence location, and the CMB fluctuations will then depend on the universe baryon content which is reflected specifically on the height of the second peak of fig. 1.2. Here is when dark matter comes into play: ordinary matter cannot effectively clump together to generate the potential wells  $\phi$  just described, due to electrostatic forces. In order to generate the seeds that later will become the structures that we observe today, we need an electrically neutral form of matter. Dark matter plays this role and its effect can be seen in the height of the third peak, which gives us a measure of how much dark matter there is in comparison to the total amount of light at recombination.

Despite the sensitivity of the CMB power spectrum on the effects already mentioned, it presents also a high degree of degeneracy on the cosmological parameters. Once this degeneracy is broken (see below), Planck obtained the following values for the baryonic and the dark matter densities [64]:

$$\Omega_b h^2 = 0.02230 \pm 0.00014, \quad \Omega_{dm} h^2 = 0.1188 \pm 0.0010 \quad (1.22)$$

here  $h$  is the Hubble constant in units of  $100 \text{ km s}^{-1} \text{ Mpc}^{-1}$ . This equation implies that there is more than five times more dark matter than baryonic matter. In fact, from the total energy budget of the universe, we have that 4.9% corresponds to normal matter, 26.8% to dark matter and 68.3% to an unknown form of energy called dark energy, driving the expansion of the universe.

### ★ Large scale structure

One way to break the degeneracies in the CMB spectrum is by analysing the large scale structure of the universe. The first extensive 3D survey of galaxies was published in 1982, called the CfA redshift survey [65, 66] and showed the vast abundance of structure at large scales, something that would eventually be known as the “cosmic web”. The most up to date study of this type is the Sloan Digital Sky Survey (SDSS) that has mapped more than 900.000 galaxies in eight years [67]. The reason why these surveys provide evidence for dark matter was already hinted: the current structure of the universe arose from the initial density fluctuations that worked as seeds and that were later magnified by dark

matter. The most widely accepted source of the initial density perturbations are quantum fluctuations that were magnified by a process called inflation developed by Alan Guth [68] and Andrei Linde [69] which describes a period of early exponential growth  $10^{-35}$  seconds after the big bang. From these observations a power spectrum can also be obtained, that, as we already mentioned, is sensitive to the matter composition of the universe. A study in this direction from SDSS obtained, for the total matter density,  $\Omega_m = 0.286 \pm 0.018$  [70]. Additionally, N-body simulations have been trying to reproduce the structure we observe in the sky using cutting-edge technology since the 70's. Nowadays they are able to study the growth of nonlinear structure in the universe using supercomputers, like the Millennium Simulation that describes more than 10 billion particles to trace the evolution of the matter distribution in a cubic region of the Universe over 2 billion light-years on a side [71, 72]. Without dark matter, these simulations do not reproduce the observed structure of filaments and voids shown in fig. 1.3. And not just that, simulations in which the dark matter is relativistic during the period of structure formation (or hot, see section 1.3.3) find that small structures are washed-out, establishing that dark matter must be, dominantly, a non-relativistic particle.

### ★ Big Bang Nucleosynthesis

As already mentioned in ★ **The Cosmic Microwave Background**, the early attempts of explaining nuclear abundance patterns were done in the late 40's and throughout the 50's, from which the pioneer work of Gamow, Alpher and Herman stands out. These efforts developed in a theory of element formation now known as Big Bang Nucleosynthesis (BBN). The process of BBN takes time between 0.1 and  $10^4$ s after the Big Bang and predicts the production of the bulk of  $^4\text{He}$  and  $^2\text{H}$ , as well as good fractions of  $^3\text{He}$  and  $^7\text{Li}$  [73]. The formation of elements heavier than lithium, like the carbon on which all known life on Earth is based, would have to wait several billion years for a process called stellar nucleosynthesis. These predictions match very precisely the data as long as atoms are only 5% of the total constituents of the universe, confirming the findings of the CMB studies [74].

### ★ Gravitational lensing

As mass bends light, a high mass foreground (like a galaxy cluster) can distort a background of bright galaxies, very much as a magnifying glass would do. This is called *strong gravitational lensing*, and it can create arcs, or so-called Einstein rings, and multiple images like in fig. 1.4.



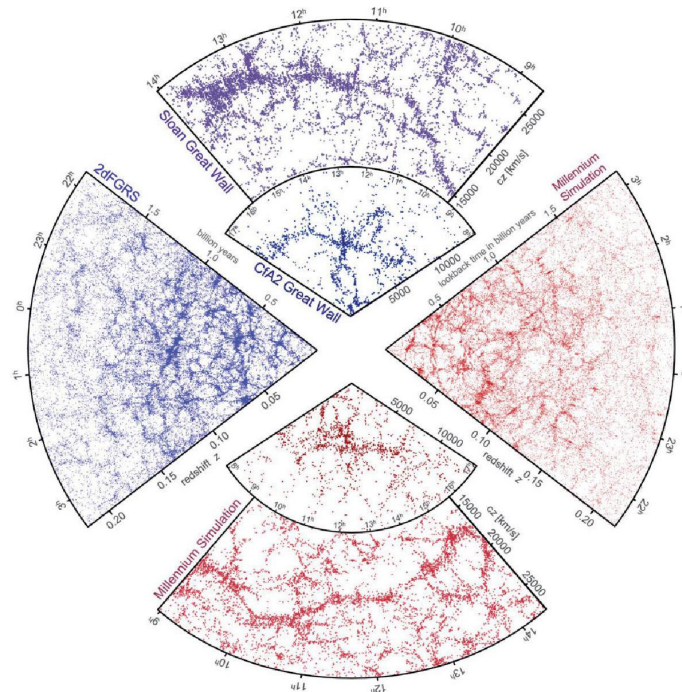


Figure 1.3: In blue and purple the results from the galactic surveys SDSS, Cfa2 and 2dFGRS, while in red the corresponding results from the Millenium simulation with matching survey geometries and magnitude limits. Figure taken from [72].



Figure 1.4: Hubble Space Telescope image of a cluster of galaxies called SDSS J1038+4849, depicting strong gravitational lensing. Credit to: NASA & ESA.



Figure 1.5: Left panel: The “bullet cluster” 1E0657-56. Right panel: the “baby bullet” MACSJ0025.4-1222. The X-ray emission of intra-cluster gas is shown in pink, while the total mass is shown in blue, using weak gravitational lensing that appears to coincide with the location of the galaxies in the cluster. Figure taken from [80].

This effect is very useful when it comes to map the foreground mass, by using the details of the image distortion. Strong gravitational lensing is, however, extremely rare. In most cases, it is necessary to use *weak gravitational lensing* where background images get merely sheared. Using statistical methods it is still possible to deduce the foreground’s gravitational potential with enough background sources. This is the method used to map the cluster mass in the Bullet Cluster: the result of a sub-cluster colliding with a larger galaxy cluster known as 1E 0657-56, a collision that happened 150 million years ago [75–77]. In the process, galaxies barely interacted (as the common distance among them is around 1 Mpc), but the hot gas that corresponds to most of the baryonic matter in the clusters got slowed down, compressed and emitted a large amount of X-ray radiation that was measured by the Chandra X-ray Observatory. When comparing this information (where most of the baryonic matter should be) to the weak lensing measurements (where most of the total matter should be), a discrepancy arises, as shown in the left panel of fig. 1.5. This discrepancy can be easily explained within the dark matter paradigm<sup>2</sup>, in which most of the clusters’ mass is contained in a form of non-interacting dark matter halo that crossed, unimpeded by the collision. In fact, from this observation it is possible to derive an upper limit on the self-interaction cross section of dark matter of  $\sigma/m < 1.25 \text{ cm}^2 \text{ g}^{-1}$  at 68% confidence level [79].

Other colliding clusters with similar characteristics have been measured, like MACS J0025.4-1222 shown in the right panel of fig. 1.5 known as the “baby bullet”, detected in 2008 [81]. On the other hand, a counter-example known as Abell 520 or the “train-wreck cluster” was observed in 2009 [82]. This cluster

<sup>2</sup>On the other hand, it seems that reproducing the high velocities at which these clusters collided,  $\sim 3000 \text{ km/s}$ , is difficult and the probability of finding such an event in dark matter simulations has been estimated to be between  $\sim 10^{-7}$  [78] and  $\sim 10^{-4}$  [70].



*Figure 1.6: Composite image of the merging galaxy cluster Abell 520. Luminosity is shown in orange as measured by the Canada-France-Hawaii Telescope in Hawaii, hot gas is shown in green as detected by NASA's Chandra X-ray Observatory and in blue the mass map of the cluster as measured by the Hubble Wide Field Planetary Camera 2 using weak lensing, that should be dominated by dark matter. Credit to: NASA, ESA, CFHT, CXO, M.J. Jee (University of California, Davis), and A. Mahdavi (San Francisco State University).*

collision presents a dark core in the middle where the hot gas is, while the bright galaxies have been displaced to the sides, as shown in fig. 1.6. Several solutions have been posed to explain this particular merger, like the collision of three clusters instead of two [83], but there is at the moment no consensus about its origin.

### 1.3.2 The Standard Halo Model

Partially based on the observations of dark matter behaviour at the galactic scale, described in the previous section, it is possible to establish a so-called Standard Halo Model (SHM), which is traditionally used as a benchmark scenario for direct detection searches (to be covered in section 1.3.4.1), in order to be able to compare results among different detectors based on the same assumptions. Under the SHM description, the dark matter in the MW comprises a single-component isothermal and isotropic sphere such that its density follows a power law  $\rho \propto 1/r^2$  [84]. It is also assumed that the solution of the collisionless Boltzmann equation corresponds to a Maxwell-Boltzmann velocity distribution with a dispersion determined by the rotation speed at large radii and truncated at an assumed value of the local escape speed after which the dark matter particles are no longer bound by the gravitational potential of the galaxy [85]

$$f(\vec{v}) = \begin{cases} \frac{1}{\sqrt{2\pi}\sigma} \exp\left(-\frac{|\vec{v}|^2}{2\sigma^2}\right), & \text{for } |\vec{v}| < v_{esc}, \\ 0, & \text{for } |\vec{v}| \geq v_{esc}, \end{cases} \quad (1.23)$$

where  $\sigma = \sqrt{3/2}v_c$ ,  $v_c = (220 \pm 20)$  km/s and  $v_{esc} \approx 544$  km/s.

Cosmological simulations provide however evidence that indicates a significant departure from this velocity distribution [86–88]. One of the major problems is that it is unable to adequately reproduce the anisotropies expected from a complex merger history of actual galaxies [89, 90]. Many alternative models exist in the literature, but considering that no consensus has been reached in terms of how to best describe the anisotropic velocities expected in the MW, we will limit ourselves (most notably in chapter 3) to the simple case of eq. (1.23).

### 1.3.3 The Usual Suspects

From the previous subsection it is already possible to infer some of the conditions that an hypothetical particle must fulfil in order to be a viable dark matter candidate. The complete list is as follows [85]. The particle must:

1. produce the right relic abundance (see eq. (1.22)).
2. be mostly non-relativistic at the time of large scale structure formation.
3. be electrically neutral.<sup>3</sup>
4. be stable or long lived, as we still measure its gravitational effects.
5. be consistent with BBN.
6. leave stellar evolution unchanged.
7. be compatible with self-interaction limits.
8. be compatible with direct and indirect dark matter searches.

The last point will be further explored in section 1.3.4. From the previous list it is clear that no particle in the SM can satisfy all the requirements. Neutrinos are very close and were considered in fact as a viable candidate in the early 80’s. Nevertheless, these light particles would remain relativistic until late times, however it was realised that heavier particles that would decouple earlier could also be successful candidates. A new classification of candidates emerged then and candidates could be categorized in three families: hot, warm and cold dark matter (HDM, WDM and CDM), where the “temperature” was associated to their typical velocity at a particular stage of universe evolution, like recombination [94]. Neutrinos would then be HDM candidates, but as we already mentioned in section 1.3.1.2, they would smooth large scale structures. This is evidenced already in a simulation from 1986 [95], reproduced in fig. 1.7, which shows the

<sup>3</sup>The possibility of having millicharged dark matter is still open [91] and some models exist in this direction [92, 93].

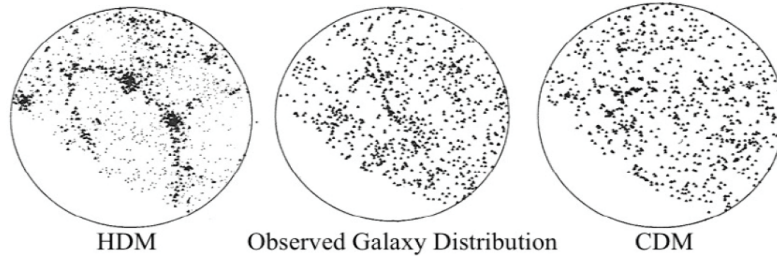


Figure 1.7: Large scale structure distribution simulation for a universe dominated by HDM (left plot) or CDM (right plot) in comparison with the observed distribution measured by CfA Survey. Figure taken from [98], reproduced from [95].

disagreement between the HDM paradigm and the observed universe, ruling out neutrinos as the dominant contribution to dark matter (they do however contribute to a small fraction of it, depending on the value of the sum of their masses  $\sum m_\nu$ , see for example [96, 97]). This is the reason why we need to go beyond the SM (BSM) in order to find the nature of dark matter using as a guidance the properties just listed.

It is worth to mention here that nothing ensures that the dark sector is composed by a single particle species, so it might well be that more than one of the candidates that we are going to list below contribute to dark matter, in the same way in which several kinds of fundamental particles constitute the visible sector. However, we would expect some sort of underlying order behind it, as it happens with the SM.

### 1.3.3.1 WIMPs

Weakly Interacting Massive Particles or WIMPs for short, have been the primary suspects in the dark matter race for a long time, drawing much of the experimental focus (see section 1.3.4). There are two main reasons behind this. The first is that, in order to fulfil item 1. on the list above, using what is considered the simplest production mechanism (thermal production, see section 1.3.4.1), one obtains an average annihilation rate at the time of chemical decoupling of [99]

$$\langle \sigma_{ann} v \rangle = 2.8 \times 10^{-26} \text{ cm}^3 \text{ s}^{-1} \quad (1.24)$$

where  $\sigma_{ann}$  is the annihilation cross section,  $v$  is the velocity of the annihilating WIMP and the angle brackets denote an thermal averaging. The result in eq. (1.24) is more or less what one gets with weak interaction cross sections for particles around the electroweak scale. This coincidence is usually called the “WIMP miracle” and renders the particle a CDM candidate. The second

reason is supersymmetry (SUSY): a theory that introduces a spacetime symmetry relating bosons and fermions, effectively duplicating the particle content of the SM and which has the desirable property of solving the hierarchy problem mentioned in section 1.1. The model has been very popular since its first introduction in the late 70's and due to the fact that it naturally introduces a WIMP (called *neutralino*), it has helped to boost the confidence on WIMPs as the solution to the dark matter problem. Additionally, SUSY requires a discrete symmetry (called *R-parity*) in order to avoid baryon number violating processes. If the neutralino is the lightest supersymmetric particle, then it would also fulfil point 4. on the list. Unfortunately, no experimental evidence of SUSY has been found until now [100], despite the high expectations that the LHC would discover proof of it [101-103]. Regardless, WIMPs still dominate nowadays the dark matter landscape.

### 1.3.3.2 Axions

Axions were originally postulated by Roberto Peccei and Helen Quinn in 1977 in order to solve the *CP* problem [104] mentioned in section 1.1. By promoting the  $\theta$  parameter to a dynamical field and introducing a global symmetry  $U(1)_{\text{PQ}}$  that is spontaneously broken, a new scalar particle appears (the axion as the Goldstone mode, with a small mass if the symmetry is anomalous). The axion acquires interactions with gluons, which generate an axion potential that induces  $\theta = 0$ . The phenomenology of the axion is determined entirely by the symmetry breaking scale  $f_a$ , with its mass given by [105]

$$m_a \approx 6 \times 10^{-10} \text{ eV} \left( \frac{10^{16} \text{ GeV}}{f_a} \right). \quad (1.25)$$

If  $f_a$  is of the order of grand unified theories (GUTs)  $\sim 10^{16}$  GeV, then  $m_a \sim \mu\text{eV}$ . This axion would however overclose the universe [106]. In any case, the method described here is generic and the Goldstone bosons that do not acquire a mass from QCD are called axion-like-particles (ALPs) and in this case their mass depend on additional parameters beside  $f_a$ . ALPs have been constrained from different searches to be in the mass range  $1\mu \text{ eV} < m_a < 3 \text{ meV}$  [107]. This light particles would interact so weakly with normal matter that they would never achieve thermal equilibrium in the early universe, making them a CDM candidate [108].

### 1.3.3.3 Sterile Neutrinos

Sterile neutrinos are particles that do not experience any of the interactions of the SM, meaning that they are singlets under  $G_{\text{SM}}$  in eq. (1.1) (hence *sterile*), but as they are neutrinos, they would still mix with the *active* states  $\nu_\ell$  ( $\ell = e, \mu, \tau$ )



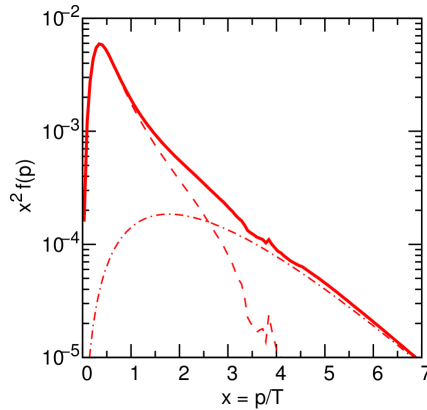


Figure 1.8: Dark matter spectrum for a resonantly produced sterile neutrino with  $m_S = 3$  keV as a function of  $x = p/T$ . The dashed-dotted line represents the spectrum obtained through the Dodelson-Widrow Mechanism, while the dashed line is the Shi-Fuller contribution, with  $L_\alpha = 16$  (see the text). Figure taken from [112], reproduced from [113].

first mentioned in section 1.2.2 (but described in detail in section 1.4). Due to its properties, the mass of this particle is not constrained by the Brout-Englert-Higgs mechanism, and its value can vary in a wide range depending on its particular theoretical function, producing very different phenomenologies [109]. For example, if its very massive ( $m_S \sim 10^{14}$  GeV) we can obtain very light active states with Yukawa coupling is of the same order as those of quarks and charged leptons through the already mentioned type-I seesaw mechanism (described in detail in section 1.4.3). On the other hand, if its mass is in the keV range they would constitute a WDM candidate (although this highly depends on its production mechanism). There is however a lower limit for fermions comprising all dark matter: due to Pauli exclusion principle they cannot be arbitrarily packed in high density regions like galactic centers, which results in the Tremaine-Gunn limit [110] (later updated in [111] using different datasets):

$$m_S > 0.4, \dots, 2 \text{ keV}. \quad (1.26)$$

Other ways to constrain this candidate are going to be described in section 1.3.4.2 and it is also going to be the main topic of chapter 3. On the remainder of this section we will focus on the different production mechanisms available in the literature in order to explain its relic abundance.

We can distinguish three different type of mechanisms that are able to generate these particles in the early universe, despite them being SM singlets:

1. **Production through mixture with active neutrinos:** The most simple scenario for sterile neutrinos production is through the oscillations of ac-

tive states. The process takes place at temperatures below 1 GeV and depends exclusively on  $m_S$  and the mixing angle  $\theta_S$  with active neutrinos, that are in thermal equilibrium as opposed to the sterile states that are never in equilibrium in the early universe. It was first proposed by Dodelson and Widrow in 1993 [114] and later refined to include additional corrections [115–117]. It leads to [118]

$$\Omega_S \sim 0.2 \left( \frac{\sin^2 \theta_S}{3 \times 10^{-9}} \right) \left( \frac{m_S}{3 \text{ keV}} \right)^{1.8}. \quad (1.27)$$

The range of masses and mixing angles required to reproduce eq. (1.22) are unfortunately in tension with the limits imposed by X-ray constraints discussed in section 1.3.4.2. Despite this, and as we will notice in section 3.5, there is no reason *a priori* these type of oscillations are not present, unless the reheating temperature after inflation is low.<sup>4</sup> Production must involve then more than one type of process.

A modification to this scenario was proposed by Shi and Fuller in 1998 [122], who considered the impact to the oscillations in the presence of a lepton asymmetry (an excess of leptons over anti-leptons). Due to the Mikheev-Smirnov-Wolfenstein (MSW) effect [123, 124] the production of sterile neutrinos get enhanced. The MSW effect describes how neutrino oscillations change in dense media like the Sun, for which the formalism of oscillations in vacuum is no longer valid. The lepton asymmetry of the universe today is not known, but the Shi-Fuller mechanism requires a relatively large value, several orders of magnitude larger than the baryon asymmetry observed in the universe today [125]. In this case, the tension with experimental constraints arising from X-rays searches mentioned before diminishes, and resonantly produced sterile neutrinos remain a viable possibility. Finally, it is worth to mention that the momentum distribution of non-thermal sterile neutrinos produced in this scenario is colder than in the Dodelson-Widrow case [122, 126] as it can be seen in the illustrative example of fig. 1.8, where the momentum distribution for a sterile neutrino with a mass of 3 keV is shown as a function of  $x = p/T$  ( $p$  being sterile neutrino momentum and  $T$  the active neutrinos temperature), in the case where the lepton asymmetry parameter, defined as  $L_\alpha := 10^6(n_\nu - n_{\bar{\nu}})/s$  ( $s$  being the entropy density), is 16. This particular case produces a warm-plus-cold dark matter mixture [127].

**2. Production through scalar decays:** As described in detail in chapter 4, many BSM theories predict the existence of additional scalars. If Yukawa

<sup>4</sup>The exact value of this temperature is currently unknown. BBN imposes lower bounds to it  $T_R \gtrsim 4 \text{ MeV}$  [119], while CMB analyses might be able to constrain it, at least in models in which reheating is driven by perturbative processes [120, 121].



interactions among the sterile neutrinos and the additional scalars occur, sterile neutrinos can be produced through the decays of this additional particle. As an illustrative example we can consider one additional scalar  $S$ , singlet under  $G_{\text{SM}}$ , and one sterile neutrino that we call here  $N$  to avoid clutter notation. The interaction can occur through the following generic Lagrangian

$$\mathcal{L}_{NS} = \frac{y_{NS}}{2} \bar{N}^c N S + \text{h.c.} \quad (1.28)$$

Unlike the previous case, the amount of produced neutrinos does not depend on the mixing angle  $\theta_S$  but on the Yukawa coupling  $y_{NS}$ . Depending on the details of the mechanism, the spectrum can be cold or warm and most possibilities remain viable. We will limit ourselves to mention the variations here, which include the  $S$  being the inflaton [128, 129], a scalar that freezes out [130, 131], freezes in [132, 133] or another kind of particle altogether [134, 135].

- 3. Production through new gauge interactions:** Even if the dark matter candidates are sterile from the SM point of view, they can still experience other interactions once extensions to the SM are considered, in which  $G_{\text{SM}}$  is embedded into a bigger symmetry group such as GUTs or other extended models, like in chapter 4. In this case the sterile neutrinos are singlets below the LHC scale, but experience new gauge interactions in the early universe, which allow them to be produced at the right abundance. In general, this is a thermal process as equilibration in the early universe is almost unavoidable when the sterile neutrinos are charged with respect to a gauge symmetry, thus most cases will produce a CDM candidate. An exception to this case occurs when their freeze-out temperature is higher than the maximal temperature of the plasma. For example, if the mass of the new gauge boson is given by  $M_{W_R}$  and  $g_*$  is the number of effective degrees of freedom at production time, the freeze-out temperature of the sterile neutrino is given by [112]

$$T_f \sim g_*^{1/6} \left( \frac{M_{W_R}}{M_W} \right)^{4/3} \times 1 \text{ MeV}, \quad (1.29)$$

which can be pushed higher than the reheating temperature for a sufficiently heavy gauge boson. A general review can be found in [136].

As we have seen, sterile neutrinos can be warm or cold dark matter candidates (or even a mixture of both), depending on the details of its production mechanism. In the CDM case, most cosmological measurements cannot distinguish them from WIMPs, rendering them a somehow less interesting case. However, as we will see in section 1.3.6, WDM particles can help solve some long standing issues with cosmological simulations at small scales.

### 1.3.4 Experimental Approaches

There is a common characteristic in all the evidence (mentioned in section 1.3.1) that we have accumulated in favour of dark matter existence: it all comes from gravity. If it really consists of a new fundamental particle, in order to determine its properties (like mass, spin or cross-section) we need other methods of detection that take a more direct approach. In order to develop this kind of approach, we need to consider that, as evidenced in section 1.3.3, there is no shortage of suspects, spanning many orders of magnitude in mass and with crucially different properties. The obvious problem is that, it is simply impossible to encompass all—or even many—of them with a single detection technique. During the last couple of decades, a wide array of innovative methods have come about, that remind us that we are not looking for a needle in a haystack, but—maybe—a single needle in a bunch of them. In this section we will briefly describe different detection methods depending on the particularities of each candidate, skipping axion detection techniques for not playing an immediate role in the bulk of this thesis.

#### 1.3.4.1 WIMP Detection

Since the masses of WIMPs are assumed to be in the range from a few GeV to  $10^4$  GeV [137] experiments must cover at least 4 orders of magnitude (although perturbative unitarity sets a higher upper bound, around 100 TeV [138]). It is common to classify these searches by the three different ways the diagram in fig. 1.9 can be read. From top to bottom, we find *direct searches* that look for scattering events of dark matter with heavy nuclei in shielded underground laboratories. From left to right, *indirect searches* detect the final products of dark matter annihilation in our galactic neighbourhood, using different kind of telescopes, and finally from right to left we have *collider searches* that try to identify the traces of direct production of dark matter in particle accelerators. The strategies just mentioned can be extrapolated to the search of any dark matter candidate. We will lay emphasis along this thesis on how a complementary interplay between these different approaches can improve the discovery potential of dark matter in a significant way.

#### ★ Direct Detection

The concept of dark matter direct detection can be traced back to 1985 with the suggestion of Mark Goodman and Edward Witten of using the energy deposit due to elastic collisions of WIMPs with atomic nuclei [139]. This rudimentary concept has highly evolved since then and a variety of methods are used to measure the small rates expected from these interactions: they translate the ex-

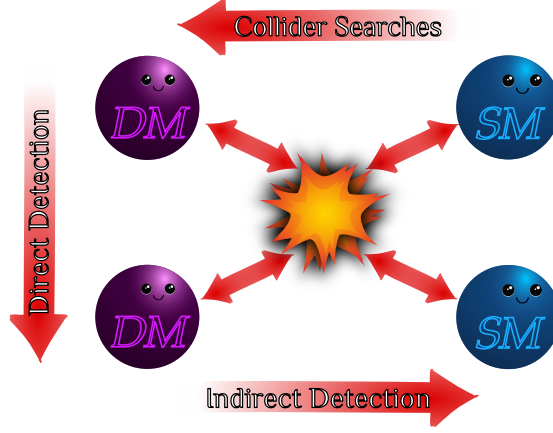


Figure 1.9: Depiction of the three kind of WIMP detection techniques.

pected scattering to ionisation, scintillation, light or phonons.

From the analysis of the movement of clusters of red giants (called red clumps) in our galactic neighbourhood it is possible to infer the local dark matter density, whose value is found to be  $\rho_0 = 0.542 \pm 0.042 \text{ GeV cm}^{-3}$  [140]. If we additionally assume that we (and our carefully designed laboratories) are moving through the dark matter halo with a mean velocity of  $220 \text{ km s}^{-1}$  (the velocity of our solar system with respect to the galactic center) and that dark matter is composed of WIMPs, this would imply that (for a particle of mass  $M_\chi \sim 100 \text{ GeV}$ ) a flux of  $10^5$  dark matter particles crosses Earth every square centimetre per second. Despite this large flux, we expect a small rate due to the weak interactions. The differential event rate is defined as [85]

$$\frac{dR}{dE_r} = \frac{\rho_0}{M_N M_\chi} \int_{v_{\min}}^{v_{\text{esc}}} v f(v) \frac{d\sigma}{dE_r} dv, \quad (1.30)$$

where  $d\sigma/dE_r$  is the differential cross-section for the WIMP-nucleus elastic scattering and  $f(v)$  is the WIMP speed distribution, the lower limit of the integration is the minimum speed that can cause a recoil

$$v_{\min} = \sqrt{\frac{M_N E_r}{2\mu_N^2}}, \quad (1.31)$$

where  $\mu_N = M_N M_\chi / (M_N + M_\chi)$  and the upper limit is the escape velocity: the maximum speed a WIMP can have in the MW before it breaks its gravitational bound,  $v_{\text{esc}} = 544 \text{ km/s}$  [141]. The differential cross section in eq. (1.30) can be separated into a spin-dependent (SD) and a spin-independent (SI) contribution

$$\frac{d\sigma}{dE_r} = \frac{M_N}{2\mu_N^2 v^2} (F_{\text{SD}}^2(E_r) \sigma_0^{\text{SD}} + F_{\text{SI}}^2(E_r) \sigma_0^{\text{SI}}) \quad (1.32)$$

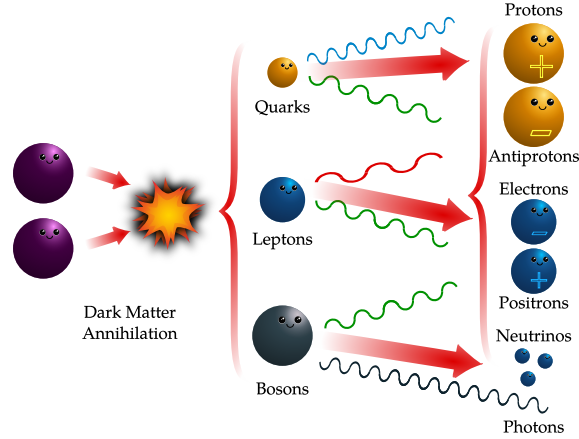


Figure 1.10: Depiction of the kind of particles resulting of dark matter annihilation.

where  $\sigma_0$  and  $F(E_\gamma)$  are the cross section at zero momentum transfer and the form factors respectively. Different models and experiments are sensitive to one part over the other, as we are going to explore in section 2.2.

### ★ Indirect Detection

Indirect detection is based on the following assumption: in regions of the universe in which dark matter is expected to be highly abundant like the galactic center (GC) or dwarf spheroidals (dSphs)<sup>5</sup>, annihilation processes (or decay processes, depending on the lifetime of the particle) should take place leading to lighter SM particles. Usually the details of this interactions are not taken into account. These processes might generate quarks, leptons and bosons that later decay while travelling the interstellar medium (ISM). What detectors finally measure are basically protons, antiprotons, electrons, positrons, neutrinos and photons, as depicted in fig. 1.10.

Due to its nature, the spectrum of annihilation products encodes information about intrinsic particle properties and are able to probe the astrophysical connection of the particles produced. We are going to focus here on the cases in which the final states are photons and neutrinos. The photons coming from dark matter annihilation can be roughly classified in three categories, depending on the stage of the decay in which they are produced. For photons being produced in a primary vertex we obtain *monochromatic lines* which are also essential for sterile neutrino dark matter detection as discussed in section 1.3.4.2. We talk about *internal bremsstrahlung* when the photons are produced radiatively and we

<sup>5</sup>Small, low-luminosity galaxies orbiting the MW. We will describe them in greater detail in section 2.3.1.

get a *continuum spectrum* when they are produced at the end of a cascade. A harder spectrum implies a better signal discrimination, but a softer one implies higher rates. The quantity in which we are interested then is the differential flux, which establishes the number of photons at a given energy bin

$$\frac{d\Phi_\gamma(E_\gamma)}{dE} = \frac{1}{4\pi} \frac{\langle \sigma_{ann} v \rangle}{2M_\chi^2} \frac{dN_\gamma}{dE_\gamma} \cdot J_{ann}, \quad (1.33)$$

where  $dN/dE$  is the number of photons produced per dark matter annihilation and  $J_{ann}$  is the so-called  $J$ -factor encoding the properties of the region of the sky under study, defined as

$$J_{ann} = \int_{\Delta\Omega} d\Omega \int \rho_\chi^2(s) ds, \quad (1.34)$$

where  $s = s(\theta)$  and the integral is computed over the line of sight within the solid angle. Here  $\rho_\chi$  is not the local dark matter density, which is a constant, but the dark matter density profile. There is certain controversy around this function which has not been settled at the moment [142-144] (see also section 1.3.6), however one of the most popular, and the one that we are going to use through this work is the Navarro-Frenk-White (NFW) profile obtained through numerical simulations [145, 146]

$$\rho_\chi(r) = \frac{\rho_s}{r/r_s(1+r/r_s)^2}, \quad (1.35)$$

where  $\rho_s$  and  $r_s$  are characteristic density and the scale radius respectively.

It is worth to mention that a clear understanding of the astrophysical background is essential, due to the fact that the contribution from dark matter to the total gamma flux is expected to be marginal. We will discuss this issue in detail in section 2.3.

The second kind of final product relevant for our analysis are neutrinos. The possible connection between a neutrino flux from the Sun to dark matter was first pointed out in 1986 [147]. It is based on the following logical chain of events: dark matter particles from the halo should scatter off the Sun's dense interior (mostly hydrogen, helium and oxygen), losing energy. Some of these collisions reduce the particle's kinetic energy to the point of becoming gravitationally bound in a closed orbit, ending up eventually in the core of the Sun. Once enough particles have been captured in this way, they would start to annihilate into SM particles, out of which just neutrinos are able to escape the dense medium in which they were produced (a photon takes between  $10^3$  to  $10^5$  years to reach the Sun's surface once it has been produced in its core). This flux of neutrinos has a clear directional signature that allows experimentalists on Earth to distinguish them from the atmospheric background. Using this information it is possible to constrain different characteristics of dark matter models, however

assuming that an equilibrium has been reached between dark matter capture and annihilation, the neutrino flux is mostly used to constrain the cross section of spin-dependent interactions, as we will see in section 2.2.2.3. At the moment the strongest bound on spin-dependent scattering with protons is provided by the IceCube neutrino telescope at high dark matter masses [148], while PICO-60 [149] and Super-Kamiokande [150] yield the leading sensitivity at low masses. See [151] for a review on the current status of these searches.

### ★ Collider Searches

The search for dark matter candidates at colliders, or more specifically at the LHC, highly relies on the assumption that WIMPs interactions with the visible sector are sizeable. An argument in favour of this idea is that, whatever mechanism produced the dark matter relic abundance, it could be inverted in order to generate dark matter particles from collisions of SM particles. The most common production mechanism is the thermal production (already mentioned in section 1.3.3.1), in which dark matter particles interact with ordinary matter until they reach a thermal equilibrium at high temperatures. The relic abundance is then set by the the temperature at which the dark matter annihilation drops below the expansion rate of the universe. At this point, dark matter is said to *freeze-out* as their interactions are insufficient to keep thermal equilibrium. In this framework, the generic expectation is that the interaction would be indeed enough for WIMPs to be produced at the LHC. The produced dark matter particle would be however impossible to measure, and the signal left behind in this case is that of an imbalance on the total transverse momentum of the particles that were measured. This is usually simply called *missing energy* or  $\cancel{E}_T$ . In practice, experimentalists look for signals of dark matter particles being produced along SM particles from initial state radiation (due to the difficulty of recording “nothing”) in what is called *mono-X* +  $\cancel{E}_T$ , where  $X$  can stand for jets, vector bosons or the Higgs boson. Of course the SM presents irreducible backgrounds to these particular searches, like *mono-X* +  $Z(\nu\nu)$ , for which a precise understanding of the SM background is essential.

As it will be mentioned in section 1.3.5, once a framework involving a rich dark matter sector, or the mediator particle between the visible and the dark sector is specified, the LHC provides an essential complementary tool in dark matter searches.

#### 1.3.4.2 Sterile Neutrino Detection

The main efforts in the search for sterile neutrinos as dark matter are focused on identifying emission lines in X-ray spectra. For sterile neutrinos with masses below  $2m_e$ , the main decay channel is  $N \rightarrow \nu_{\ell_1} \nu_{\ell_2} \bar{\nu}_{\ell_2}$  through the diagram

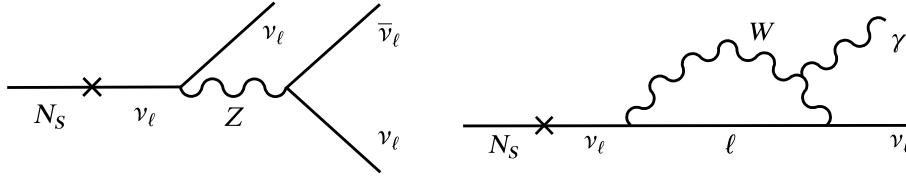


Figure 1.11: Left panel: Main decay channel of sterile neutrinos. Right panel: radiative decay of sterile neutrinos.

depicted in the left panel of fig. 1.11. A subdominant radiative decay channel which represents less than 1% of the decay width is  $N \rightarrow \gamma\nu$ , shown in the right panel of fig. 1.11, with a decay width given by [112, 152, 153]

$$\Gamma_{\gamma\nu} = \frac{9\alpha_{em}G_F^2}{256 \cdot 4\pi^4} \sin^2 \theta M_S^5, \quad (1.36)$$

where  $\alpha_{em} = e^2/4\pi$ ,  $e$  the electromagnetic coupling,  $\theta$  the mixing angle between the sterile and the active states and  $M_s$  the sterile neutrino mass. This non-relativistic decay into two close to massless particles produces a photon with energy  $E_\gamma = M_S/2$ , which translates into an X-ray line for a sterile neutrino with a keV mass. This distinctive signature has been thoroughly searched for, and in 2014 a claim for a line around 3.5 keV has been made [154, 155] with several follow-ups [156, 157], however its existence and dark matter interpretation remains controversial up to now [158–161]. This method of looking for sterile neutrinos is analogous to the indirect detection of WIMPs outlined in the previous section and its non-observation can put tight constraints in the  $\sin^2 \theta - M_S$  plane.

Sterile neutrinos can also be looked for in  $\beta$  decays experiments, that would manifest itself as a spectral distortion in the spectrum [162]. This technique can be compared to WIMP collider searches described in section 1.3.4.1.

Another way to constrain sterile neutrinos, is through their influence in the Lyman- $\alpha$  forest (the pattern of absorption light of distant galaxies when crossing hydrogen rich ISM), see [163] for a recent analysis.

We will see in chapter 3 that it is also possible to look for sterile neutrinos in direct detection experiment, closing the analogies with WIMP searches.

### 1.3.5 Theoretical Approaches

We would like to argue in this subsection how theoretical strategies in the search for dark matter can also be roughly classified in three, in the same spirit as the categorization done in section 1.3.4.1. In this case, it does not depend on the direction in which one reads the diagram, but how much one zooms in or out of it, as depicted in fig. 1.12. If one sees the diagram from far away we obtain

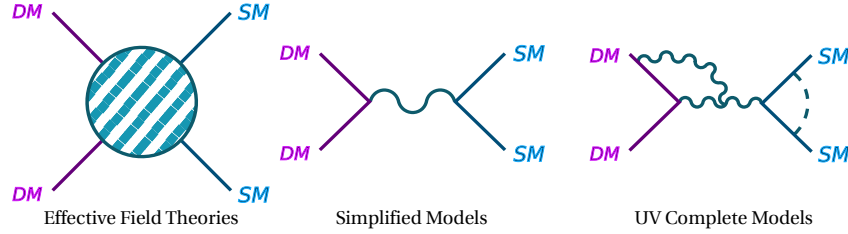


Figure 1.12: Scheme of the three different theoretical approaches.

*Effective Field Theories* (EFTs) that describe the unknown dark matter interactions with the SM in a very economical way, simply analysing systematically all the possible effective operators that can arise from the blob at the left of section 1.3.4.1. Unfortunately, the validity of this approach has been questioned in the context of colliders [164–166]. On the other side of the spectrum, we have *ultraviolet (UV) complete theories* that usually aim to solve more open questions in particle physics than just the dark matter problem. The downside is that these models usually involve a large number of parameters and hence a large number of degeneracies when it comes to compare with experimental results. Right in between we find *simplified models* where we expand the degrees of freedom of the effective operator interaction to include the mediator particle. This approach retains some of the virtues of the other two extreme approaches: a small number of parameters for simpler search strategies and close contact with UV completions which reduce to the simplified models in some particular low energy limit. Moreover, one can also exploit the searches of the mediator particle as a complementary tool to explore the dark sector. This is the approach that we are going to follow in chapter 2 and, despite its appealing features, we will notice there that it is not free of problems. On the other hand, we will take the more ambitious point of view of UV complete theories in chapter 4 where we will obtain in fact a family of models, although the dark matter issue will take there a more incidental nature.

### 1.3.6 Issues with $\Lambda$ CDM

The so-called concordance model, or  $\Lambda$ CDM (where  $\Lambda$  is the cosmological constant), is the currently widely accepted model describing several properties of the observed universe, like the abundance of light elements (through BBN), the large scale structure in the distribution of galaxies and the accelerated expansion of the universe through the cosmological constant (see section 1.3.1.2).

Despite its many achievements, some issues still remain open today especially at small scales (for a recent summary see [167]). Among these, the most important



are

1. The origin of the observed Baryonic Tully Fisher Relation (BTFR) [168].
2. The *cuspid-core problem*: in dark matter dominated galaxies like dSphs or low surface brightness galaxies (LSBs) simulations based on  $\Lambda$ CDM predict a steep density profile towards its center (cuspy), while observations show a flat profile (cored) [142, 169].
3. The *missing satellite problem*: the observed number of satellite galaxies of the MW seems to be at least one order of magnitude too small compared to those predicted by N-body simulations [170, 171].
4. The *too big to fail problem*: not just the number of these subhaloes is too small, but they seem to be not massive and dense enough in comparison with simulations [172].

The BTFR is an empirical power-law relation between the baryonic mass content ( $M_b$ ) in a disk galaxy and its rotation velocity ( $v_r$ )

$$M_b \propto v_r^4. \quad (1.37)$$

This relation stays valid over several orders of magnitude [173] and it was thought to be difficult to explain in the concordance model as it has to assume a proportionality between the galactic baryonic mass and the rotation velocity with their host haloes total virial mass and velocity, respectively. This assumption is not trivial since the observations used for the BTFR provide a very limited baryonic mass and velocity probe compared with equivalent haloes in simulations. Recently, improvements in modelling the baryonic feedback mechanism have allowed the production of realistic galactic rotation disks and the APOSTLE/EAGLE simulation has claimed to have successfully reproduced the BTFR over four decades [174], which seems to bring the problem along the path of a solution.

The cuspid-core problem was noted more than twenty years ago, but still no solution has been widely accepted. Among those proposed, we can identify some from astrophysical origins (in which case there is no need to modify  $\Lambda$ CDM) like “supernovae feedback flattening” of the cusp [175, 176] and “dynamical friction from baryonic clumps” [177, 178], both based in baryonic feedback. Solutions outside the concordance model include the introduction of WDM, mentioned in section 1.3.3.3. If dark matter is composed of light particles with the characteristics of sterile neutrinos, they retain a higher velocity than in the CDM paradigm, small scales cluster less, leading both to flatter profiles and fewer low mass haloes, hinting a solution to solve the other problems at small scales as well.

In order to solve the missing satellite problem, various suppression mechanisms for the visible population have been proposed and it seems that introducing baryon physics to the usual dissipationless dark model has been more effective than in the case of the cusp-core problem [179]. However, eliminating visible satellites from the faint end of the distribution does not exhaust the discrepancies between model and observations as the too big too fail problem puts in evidence. In this case, the proposed solutions go along the same lines as in the cusp-core problem and no consensus has been reached.

## 1.4 Neutrino Physics

Neutrino physics is a particularly wide topic, due to its long history and the potential that these ghostly particles have to explain a wide range of BSM physics, from dark matter and leptogenesis to the appearance of its own still unexplained non-vanishing masses. For brevity's sake we will not be able to cover most of their interesting aspects here, but as neutrinos will play an increasingly central role as we move along with each section of this thesis, we give a brief summary of the open questions in the field, its current status and the phenomenology expected from neutrino extensions of the SM.

### 1.4.1 The Story so Far

We have come a long way since neutrinos were first proposed by Pauli in 1930 as a way to save energy conservation in the puzzling measurements of beta decays. Not long after its first experimental confirmation in 1956 by Cowan and Reines, evidence started to mount pointing to a discrepancy between the measured flux of neutrinos coming from the Sun and the Standard Solar Model prediction. It took more than thirty years to solve the solar neutrino problem and—as always with big problems in science—its resolution led to more questions. In 1998 the Super-Kamiokande atmospheric neutrino experiment [180] obtained the first model independent evidence of neutrino oscillations. Later, in 2002 the Sudbury Neutrino Observatory confirmed this phenomenon [181], which solved the long standing problem by showing that the reason less than the predicted amount of electron-neutrinos from the Sun is measured was because one third of them oscillate into the other two possible flavours on their way to Earth. This discovery had a deep impact in the SM foundations, as an oscillation among neutrino flavours imply that they are massive particles, while on the SM description given in section 1.2.2, no mechanism can generate these small masses.

Neutrino oscillations were first introduced by Bruno Pontecorvo in 1958 [182] and the modern description is based on the following assumption (now largely

confirmed by experiments): neutrinos are produced through weak interactions and therefore as weak eigenstates ( $\nu_e$ ,  $\nu_\mu$  or  $\nu_\tau$ ). On the other hand the mass matrix is not diagonal in the flavour base, which means that the mass eigenstates  $\nu_1$ ,  $\nu_2$  and  $\nu_3$ , resulting from the process of diagonalization, do not correspond to their flavour counterparts. As already mentioned in section 1.2.2, the way in which this is parametrized is through the PMNS matrix that has the same shape as the CKM matrix in eq. (1.18):

$$\begin{bmatrix} \nu_e \\ \nu_\mu \\ \nu_\tau \end{bmatrix} = U_{\text{PMNS}}(\theta_{12}, \theta_{23}, \theta_{13}; \text{phases}) \begin{bmatrix} \nu_1 \\ \nu_2 \\ \nu_3 \end{bmatrix}. \quad (1.38)$$

Accordingly, the probability of finding a neutrino on a given flavour state once it was produced oscillates with time. If the neutrinos are detected a macroscopic distance  $L$  away from the point in which they were produced, the probability of a neutrino  $\nu_\alpha$  to be converted into a  $\nu_\beta$ , in vacuum, is given by

$$P(\nu_\alpha \rightarrow \nu_\beta) = \sum_{i,j} U_{\alpha i}^* U_{\beta i} U_{\alpha j} U_{\beta j}^* \exp\left(i \frac{\Delta m_{ij} L}{2E_\nu}\right), \quad (1.39)$$

where  $\Delta m_{ij} := m_j^2 - m_i^2$ ,  $U_{\alpha i}$  are the elements of the PMNS matrix and  $E_\nu \sim |\vec{p}|$  is the neutrino energy. Oscillations can be described by six independent parameters: two mass differences ( $\Delta m_{12}$  and  $\Delta m_{23}$ ), three Euler angles ( $\theta_{12}$ ,  $\theta_{23}$ ,  $\theta_{13}$ ) and one  $CP$  violating phase  $\delta_{CP}$ <sup>6</sup>. In this convention there are two possibilities for the neutrinos masses hierarchy: normal (NH) if  $m_1 < m_2 < m_3$  or inverted (IH) if  $m_3 < m_1 < m_2$ . The experimental status of these independent parameters can be found in [183-186].

## 1.4.2 Unsolved Mysteries

We have learnt several things concerning neutrino physics in the past decades, however there are many open questions both from the experimental and theoretical point of view that still elude us. We will briefly describe the most relevant ones in this section, to conclude this introduction in the next section with an overview of the seesaw mechanism, as it will play an important role in chapter 4.

- 1. What is the mass hierarchy?** It is currently not possible to determine if the  $\nu_3$  mass eigenstate is heavier (NH) or lighter (IH) than  $\nu_1$  and  $\nu_2$ . We can see a graphical representation of the two possibilities in fig. 1.13, where the flavour components of the three mass eigenstates is also shown, as a

<sup>6</sup>If neutrinos happen to be Majorana particles two additional phases must be considered, as we will see.

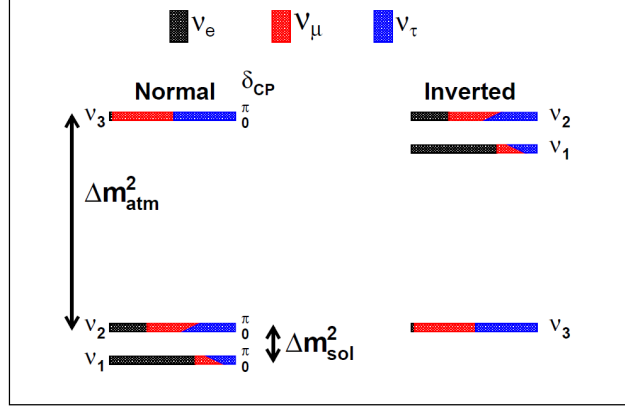


Figure 1.13: Possible neutrino mass hierarchies. The flavour composition is indicated in the mass eigenstates as a function of the unknown phase  $\delta_{CP}$ . Figure taken from [187].

function of the  $CP$  violating phase. It is important to determine which one is the case, as one of the main goals of theoretical neutrino physics is to formulate a particle physics model able to explain the observed pattern of neutrino mixing angles and masses, possibly relating them to the other fermions. Clearly, the specific hierarchy plays a vital role, potentially able to rule out half of the many models aspiring to cover this gap. It also plays an important role in neutrino-less double beta ( $0\nu 2\beta$ ) decay experiments, as we will see. As it is implied in fig. 1.13

$$\Delta m_{atm}^2 := \Delta m_{23}^2 \gg \Delta m_{sol}^2 := \Delta m_{12}^2. \quad (1.40)$$

Due to this, most oscillations experiments can be reasonably well approximated by a 2-flavour component description. In this case eq. (1.39) becomes

$$P(\nu_\alpha \rightarrow \nu_\beta) = \sin^2 2\theta \cdot \sin^2 \left( 1.27 \cdot \frac{\Delta m^2 [\text{eV}^2]}{E_\nu [\text{GeV}]} L [\text{km}] \right) \quad (1.41)$$

and the hierarchy, given by the sign of  $\Delta m^2$  cannot be identified in this case. There are two experimental approaches to remove this ambiguity: the previous equation is valid for oscillations in vacuum, and when matter effects are relevant the MSW resonant transition introduces terms sensitive to the sign of  $\Delta m^2$  (this is exploited in accelerator neutrinos appearance [188] and atmospheric neutrinos experiments [189]). On the other hand, with a detector sensitive enough to measure  $\Delta m_{12}^2$  in such a way that a 3-flavour description is necessary, the same goal can be

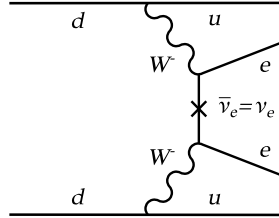


Figure 1.14: Quark level “lobster” diagram for  $0\nu 2\beta$  decay, mediated by a Majorana neutrino.

achieved (reactor antineutrinos experiments use this method [188]). Finally, the matter effects of neutrinos coming from supernova explosions and through Earth can be up to 5%, pointing to an independent way to establish the neutrinos’ hierarchy, once said event is measured [190].

**2. What is the nature of neutrinos?** Due to the fact that neutrinos are neutral fermions (zero electric or colour charge), the possibility that they are equal to its anti-particles, making them Majorana fermions—instead of Dirac like the other SM fermions—remains open. As we will see in the next section, a popular mechanism to generate neutrino masses is the see-saw mechanism. In most versions the neutrinos are Majorana particles, for which the discrimination about the neutrino nature has deep theoretical consequences. In order to shed light on this mystery a common approach is to analyse processes in which the total lepton number might not be conserved. The most studied possibility are experiments in which the  $0\nu 2\beta$  decay of even-even nuclei are expected [191]:

$$(A, Z) \rightarrow (A, Z + 2) + 2e^- . \quad (1.42)$$

As we mentioned, in the Majorana case, the PMNS matrix takes the following form (in the standard parametrization)

$$U_{\text{PMNS}} := \begin{bmatrix} c_{12}c_{13} & s_{12}c_{13} & s_{13}e^{-i\delta} \\ -s_{12}c_{23} - c_{12}s_{23}s_{13}e^{i\delta} & c_{12}c_{23} - s_{12}s_{23}s_{13}e^{i\delta} & s_{23}c_{13} \\ s_{12}s_{23} - c_{12}c_{23}s_{13}e^{i\delta} & -c_{12}s_{23} - s_{12}c_{23}s_{13}e^{i\delta} & c_{23}c_{13} \end{bmatrix} \cdot \mathcal{P}, \quad (1.43)$$

where

$$\mathcal{P} := \text{diag}(1, e^{i\alpha}, e^{i(\beta+\delta)}), \quad (1.44)$$

with  $\alpha$  and  $\beta$  the Majorana  $CP$  violating phases. If  $0\nu 2\beta$  decay processes occur in nature and are produced by light Majorana neutrino exchange<sup>7</sup>,

<sup>7</sup>If this process were to be observed, the issue of neutrino character would not be completely settled as other lepton violating physics cannot be immediately discarded [191].

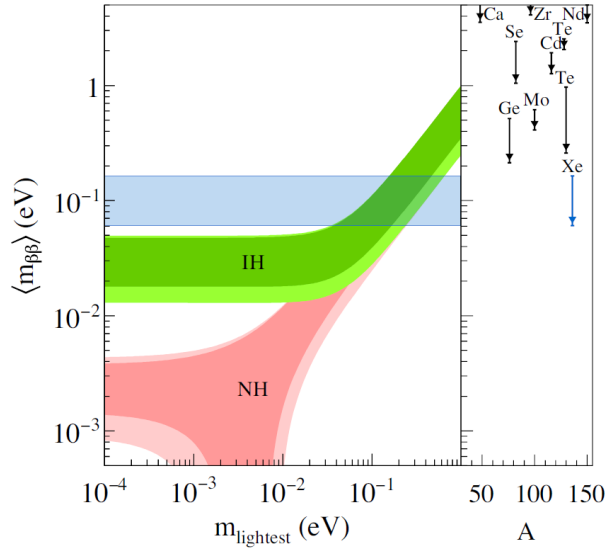


Figure 1.15: Left panel: Bands for the value of the effective mass parameter as a function of the mass of the lightest neutrino, for NH (red band) and IH (green band). The present best experimental upper limits are shown in the blue band. Right panel: Present best upper limits, with uncertainty bars, on  $\langle m_{\beta\beta} \rangle$  from experiments performed on each emitter element, as a function of their mass number  $A$ . Figure taken from [192].

they would be mediated by a diagram like the one shown in fig. 1.14 and are sensitive to the so-called effective Majorana mass parameter

$$\langle m_{\beta\beta} \rangle := \left| \sum_i U_{ei}^2 m_i \right| = |c_{12}^2 c_{13}^2 m_1 + s_{12}^2 c_{13}^2 m_2 e^{i\alpha} + s_{13}^2 m_3 e^{i\beta}|. \quad (1.45)$$

As this parameter can be rewritten in terms of the lightest neutrino mass, these processes are also sensitive to this variable and it is customary to plot its limits as a function of it as in fig. 1.15. This plot, showing the current status of  $0\nu 2\beta$  searches, also evidences that they can help settle the issue related to the neutrino mass hierarchy, as we have anticipated. We can see that these open questions are deeply intertwined.

- 3. What is the absolute mass scale?** Despite knowing the mass differences between the mass eigenstates thanks to oscillation experiments, they cannot provide any information about their individual masses. In particular we do not know the value of the lightest neutrino mass, which sets the absolute mass scale. There are three known ways to probe this parameter: the end-point part of the electron spectrum in Tritium  $\beta$ -decay [193],

the observation of large-scale structures in the early universe [194] and, as we already saw, if neutrinos are Majorana particles, through  $0\nu 2\beta$  searches [195, 196].

- 4. What is the value of the CP-violating phase(s)?** Thanks to the robust evidence of a non-zero value of  $\theta_{13}$  found in the Daya Bay [197, 198], RENO [199] and Double Chooz [200] experiments, a window was open to probe the Dirac phase of  $U_{\text{PMNS}}$ . Recent global fits point to a non-zero value for  $\sin \delta$  using a combination of long baseline accelerator and short baseline reactor data. The fits point to values of  $\delta$  close to  $3\pi/2$ , while the  $CP$  conserving cases are disfavoured at  $\sim 2.5\sigma$  [183–186]. The magnitude of  $CP$  violation is traditionally parametrized with the so-called Jarlskog invariant  $J_{CP}$  [201] defined as

$$J_{CP} := \Im [U_{\mu 3} U_{e 3}^* U_{e 2} U_{\mu 2}^*] = \frac{1}{8} \cos \theta_{13} \sin 2\theta_{12} \sin 2\theta_{23} \sin 2\theta_{13} \sin \delta. \quad (1.46)$$

For the current best fits of these parameters, we obtain  $J_{CP} \approx -0.030$ . This value must be compared with the same invariant in the quark sector [202]

$$J_{CP}^{\text{quarks}} = (3.04_{-0.20}^{+0.21}) \times 10^{-5}. \quad (1.47)$$

On the other hand, the Majorana phases  $\alpha$  and  $\beta$  cannot be probed in oscillation experiments, but as pointed out,  $0\nu 2\beta$  experiments aim to probe their values once positive signals are measured. The importance behind the realization of  $CP$  violation in the lepton sector is that it constitutes an essential ingredient of a tantalizing mechanism to explain the observed baryon asymmetry of the universe (BAU) through a mechanism called Leptogenesis [203, 204].

Two additional questions can be posed, closer to the theoretical aspects of neutrino physics than to its experimental side: *what is the mechanism of neutrino mass generation?* and *are there more neutrino states?* We will partially address these issues on the next section.

### 1.4.3 The Riddle of the Mass

The SM, as far as it was presented in section 1.2.2, cannot account for neutrino masses. This is due to the absence of right-handed neutrinos and the minimal Higgs content. Additionally, the lack of neutrino masses in the SM is a result that not just holds to all orders in perturbation theory, but also when non-perturbative effects are taken into account, because of the accidental  $B - L$  symmetry present in the model [205]. It seems then that in order to generate neutrino masses, we have to either consider additional states or break the  $B - L$

symmetry, or both, which means in any case BSM physics.

If the mechanism that grants neutrinos their small masses occurs at a scale  $\Lambda$ , it could show up at small scales as a non-renormalizable dimension 5 operator known as the Weinberg operator [206]

$$\mathcal{L} \supset \frac{1}{2} \frac{\lambda_{\alpha\beta}}{\Lambda} (L_\alpha H)^T (L_\beta H), \quad (1.48)$$

with  $\alpha, \beta = e, \mu, \tau$  and  $H$  the Higgs doublet. This operator generates the mass matrix

$$m_\nu = \frac{\lambda_{\alpha\beta} \langle H \rangle^2}{\Lambda}. \quad (1.49)$$

If we assume  $\lambda_{\alpha\beta} \sim 1$  (see section 1.1 for comments about this assumption), then it follows that  $\Lambda \sim 10^{15}$  GeV in order to obtain  $m_\nu \sim 0.05$  eV, which satisfies current limits [64].

Another possibility is to simply introduce a right-handed neutrino  $N_R$  which allows the Yukawa coupling

$$\mathcal{L} \supset y_\nu \bar{L} H N_R + \text{h.c.} \quad (1.50)$$

generating, after SSB, the following Dirac mass term

$$m_D = y_\nu \langle H \rangle. \quad (1.51)$$

In this case we need  $y_\nu \sim 10^{-13}$  to generate the right neutrino masses. As we have discussed, this has historically been seen as unnatural. However, the right-handed neutrino can also have Majorana masses

$$\mathcal{L} \supset \frac{1}{2} M_R \bar{N}_R^c N_R + \text{h.c.} \quad (1.52)$$

Once the mass matrix is diagonalized, we obtain for the active states a mass matrix given by

$$m_\nu = -m_D^T M_R^{-1} m_D, \quad (1.53)$$

where  $M_R$  plays the role of the cutoff scale  $\Lambda$  of the Weinberg operator. This is known as the seesaw type-I mechanism [207–210], which is probably the most popular framework to generate neutrino masses. If, instead of right-handed neutrinos, we generate eq. (1.48) by adding scalar Higgs triplets we obtain the seesaw type-II [211–213], and the seesaw type-III if we add fermion triplets [214]. Another common possibility are radiative mechanisms with new particles in the loops [215–217].



## References

- [1] D. Hanneke, S. Fogwell and G. Gabrielse, *New Measurement of the Electron Magnetic Moment and the Fine Structure Constant*, *Phys. Rev. Lett.* **100** (2008) 120801 [[arXiv:0801.1134](#)].
- [2] K.S. Babu, E. Ma and J.W.F. Valle, *Underlying  $A(4)$  symmetry for the neutrino mass matrix and the quark mixing matrix*, *Phys. Lett.* **B552** (2003) 207 [[hep-ph/0206292](#)].
- [3] A. Strumia and F. Vissani, *Neutrino masses and mixings and...*, [hep-ph/0606054](#).
- [4] S.F. King, A. Merle, S. Morisi, Y. Shimizu and M. Tanimoto, *Neutrino Mass and Mixing: from Theory to Experiment*, *New J. Phys.* **16** (2014) 045018 [[arXiv:1402.4271](#)].
- [5] C.A. Baker et al., *An Improved experimental limit on the electric dipole moment of the neutron*, *Phys. Rev. Lett.* **97** (2006) 131801 [[hep-ex/0602020](#)].
- [6] R.D. Peccei, *The Strong CP problem and axions*, *Lect. Notes Phys.* **741** (2008) 3 [[hep-ph/0607268](#)].
- [7] **ATLAS, CMS** Collaboration, G. Aad et al., *Combined Measurement of the Higgs Boson Mass in  $pp$  Collisions at  $\sqrt{s} = 7$  and 8 TeV with the ATLAS and CMS Experiments*, *Phys. Rev. Lett.* **114** (2015) 191803 [[arXiv:1503.0758](#)].
- [8] M. Schmaltz and D. Tucker-Smith, *Little Higgs review*, *Ann. Rev. Nucl. Part. Sci.* **55** (2005) 229 [[hep-ph/0502182](#)].
- [9] G. 't Hooft, *Naturalness, chiral symmetry, and spontaneous chiral symmetry breaking*, *NATO Sci. Ser. B* **59** (1980) 135.
- [10] S.L. Glashow, J. Iliopoulos and L. Maiani, *Weak Interactions with Lepton-Hadron Symmetry*, *Phys. Rev.* **D2** (1970) 1285.
- [11] S. Hossenfelder, *Screams for Explanation: Finetuning and Naturalness in the Foundations of Physics*, [arXiv:1801.0217](#).
- [12] G. Breit, E.U. Condon and R.D. Present, *Theory of Scattering of Protons by Protons*, *Phys. Rev.* **50** (1936) 825.
- [13] B. Cassen and E.U. Condon, *On nuclear forces*, *Phys. Rev.* **50** (1936) 846.

- [14] T. Nakano and K. Nishijima, *Charge Independence for V-particles*, *Prog. Theor. Phys.* **10** (1953) 581.
- [15] T.D. Lee and C.N. Yang, *Question of Parity Conservation in Weak Interactions*, *Phys. Rev.* **104** (1956) 254.
- [16] C.S. Wu, E. Ambler, R.W. Hayward, D.D. Hoppes and R.P. Hudson, *Experimental Test of Parity Conservation in Beta Decay*, *Phys. Rev.* **105** (1957) 1413.
- [17] J.H. Christenson, J.W. Cronin, V.L. Fitch and R. Turlay, *Evidence for the  $2\pi$  Decay of the  $K_2^0$  Meson*, *Phys. Rev. Lett.* **13** (1964) 138.
- [18] S. Weinberg, *The Making of the standard model*, *Eur. Phys. J.* **C34** (2004) 5 [[hep-ph/0401010](#)].
- [19] C.N. Yang and R.L. Mills, *Conservation of Isotopic Spin and Isotopic Gauge Invariance*, *Phys. Rev.* **96** (1954) 191.
- [20] P.W. Higgs, *Broken Symmetries and the Masses of Gauge Bosons*, *Phys. Rev. Lett.* **13** (1964) 508.
- [21] F. Englert and R. Brout, *Broken Symmetry and the Mass of Gauge Vector Mesons*, *Phys. Rev. Lett.* **13** (1964) 321.
- [22] J. Goldstone, *Field Theories with Superconductor Solutions*, *Nuovo Cim.* **19** (1961) 154.
- [23] J. Goldstone, A. Salam and S. Weinberg, *Broken Symmetries*, *Phys. Rev.* **127** (1962) 965.
- [24] S. Weinberg, *A Model of Leptons*, *Phys. Rev. Lett.* **19** (1967) 1264.
- [25] A. Salam, *Weak and Electromagnetic Interactions*, *Conf. Proc.* **C680519** (1968) 367.
- [26] **ATLAS** Collaboration, G. Aad et al., *Observation of a new particle in the search for the Standard Model Higgs boson with the ATLAS detector at the LHC*, *Phys. Lett.* **B716** (2012) 1 [[arXiv:1207.7214](#)].
- [27] **CMS** Collaboration, S. Chatrchyan et al., *Observation of a new boson at a mass of 125 GeV with the CMS experiment at the LHC*, *Phys. Lett.* **B716** (2012) 30 [[arXiv:1207.7235](#)].
- [28] M. Gell-Mann, *The Eightfold Way: A Theory of strong interaction symmetry*, .
- [29] Y. Ne'eman, *Derivation of strong interactions from a gauge invariance*, *Nucl. Phys.* **26** (1961) 222.

- [30] M. Gell-Mann, *A Schematic Model of Baryons and Mesons*, *Phys. Lett.* **8** (1964) 214.
- [31] G. Zweig, *An SU(3) model for strong interaction symmetry and its breaking. Version 1*, .
- [32] G. Zweig, *An SU(3) model for strong interaction symmetry and its breaking. Version 2*, in *Developments in the Quark Theory of Hadrons. Vol. 1. 1964 - 1978* (D.B. Lichtenberg and S.P. Rosen, eds.), p. 22. Hadronic Press, 1980, 1964.
- [33] D.J. Gross and F. Wilczek, *Ultraviolet Behavior of Nonabelian Gauge Theories*, *Phys. Rev. Lett.* **30** (1973) 1343.
- [34] H.D. Politzer, *Reliable Perturbative Results for Strong Interactions?*, *Phys. Rev. Lett.* **30** (1973) 1346.
- [35] J.D. Bjorken, *Asymptotic Sum Rules at Infinite Momentum*, *Phys. Rev.* **179** (1969) 1547.
- [36] M. Breidenbach, J.I. Friedman, H.W. Kendall, E.D. Bloom, D.H. Coward, H.C. DeStaebler, J. Drees, L.W. Mo and R.E. Taylor, *Observed Behavior of Highly Inelastic electron-Proton Scattering*, *Phys. Rev. Lett.* **23** (1969) 935.
- [37] S. Weinberg, *Nonabelian Gauge Theories of the Strong Interactions*, *Phys. Rev. Lett.* **31** (1973) 494.
- [38] D.J. Gross and F. Wilczek, *Asymptotically Free Gauge Theories - I*, *Phys. Rev.* **D8** (1973) 3633.
- [39] H. Fritzsch, M. Gell-Mann and H. Leutwyler, *Advantages of the Color Octet Gluon Picture*, *Phys. Lett.* **47B** (1973) 365.
- [40] K. Nishijima, *Charge Independence Theory of V Particles*, *Prog. Theor. Phys.* **13** (1955) 285.
- [41] M. Gell-Mann, *The interpretation of the new particles as displaced charge multiplets*, *Nuovo Cim.* **4** (1956) 848.
- [42] M. Kobayashi and T. Maskawa, *CP Violation in the Renormalizable Theory of Weak Interaction*, *Prog. Theor. Phys.* **49** (1973) 652.
- [43] N. Cabibbo, *Unitary Symmetry and Leptonic Decays*, *Phys. Rev. Lett.* **10** (1963) 531.
- [44] G. Bertone and D. Hooper, *A History of Dark Matter*, *Submitted to: Rev. Mod. Phys.* (2016) [[arXiv:1605.0490](https://arxiv.org/abs/1605.0490)].

- [45] J.H. Oort, *The force exerted by the stellar system in the direction perpendicular to the galactic plane and some related problems*, *Bulletin of the Astronomical Institutes of the Netherlands* **6** (Aug., 1932) 249.
- [46] E. Hubble and M.L. Humason, *The Velocity-Distance Relation among Extra-Galactic Nebulae*, *Astrophysical Journal* **74** (July, 1931) 43.
- [47] F. Zwicky, *Die Rotverschiebung von extragalaktischen Nebeln*, *Helv. Phys. Acta* **6** (1933) 110. [Gen. Rel. Grav.41,207(2009)].
- [48] F. Zwicky, *Republication of: The redshift of extragalactic nebulae*, *General Relativity and Gravitation* **41** (Jan., 2009) 207.
- [49] M. Schwarzschild, *Mass distribution and mass-luminosity ratio in galaxies*, *Astronomical Journal* **59** (Sept., 1954) 273.
- [50] V.C. Rubin and W.K. Ford, Jr., *Rotation of the Andromeda Nebula from a Spectroscopic Survey of Emission Regions*, *Astrophysical Journal* **159** (Feb., 1970) 379.
- [51] K.C. Freeman, *On the Disks of Spiral and SO Galaxies*, *Astrophysical Journal* **160** (June, 1970) 811.
- [52] M.S. Roberts and A.H. Rots, *Comparison of Rotation Curves of Different Galaxy Types*, *Astronomy and Astrophysics* **26** (Aug., 1973) 483.
- [53] J. Einasto, A. Kaasik and E. Saar, *Dynamic evidence on massive coronas of galaxies*, *Nature* **250** (July, 1974) 309.
- [54] J.P. Ostriker, P.J.E. Peebles and A. Yahil, *The size and mass of galaxies, and the mass of the universe*, *Astrophysical Journal Letters* **193** (Oct., 1974) L1.
- [55] R.A. Alpher, H. Bethe and G. Gamow, *The origin of chemical elements*, *Phys. Rev.* **73** (1948) 803.
- [56] R.A. Alpher and R.C. Herman, *On the Relative Abundance of the Elements*, *Physical Review* **74** (Dec., 1948) 1737.
- [57] A.A. Penzias and R.W. Wilson, *A Measurement of excess antenna temperature at 4080-Mc/s*, *Astrophys. J.* **142** (1965) 419.
- [58] R.H. Dicke, P.J.E. Peebles, P.G. Roll and D.T. Wilkinson, *Cosmic Black-Body Radiation*, *Astrophys. J.* **142** (1965) 414.
- [59] D.J. Fixsen, *The Temperature of the Cosmic Microwave Background*, *Astrophys. J.* **707** (2009) 916 [[arXiv:0911.1955](https://arxiv.org/abs/0911.1955)].

- [60] **COBE** Collaboration, G.F. Smoot et al., *Structure in the COBE differential microwave radiometer first year maps*, *Astrophys. J.* **396** (1992) L1.
- [61] **WMAP** Collaboration, D.N. Spergel et al., *First year Wilkinson Microwave Anisotropy Probe (WMAP) observations: Determination of cosmological parameters*, *Astrophys. J. Suppl.* **148** (2003) 175 [[astro-ph/0302209](#)].
- [62] **Planck** Collaboration, P.A.R. Ade et al., *Planck 2013 results. XVI. Cosmological parameters*, *Astron. Astrophys.* **571** (2014) A16 [[arXiv:1303.5076](#)].
- [63] R.K. Sachs and A.M. Wolfe, *Perturbations of a Cosmological Model and Angular Variations of the Microwave Background*, *Astrophysical Journal* **147** (Jan., 1967) 73.
- [64] **Planck** Collaboration, P.A.R. Ade et al., *Planck 2015 results. XIII. Cosmological parameters*, *Astron. Astrophys.* **594** (2016) A13 [[arXiv:1502.0158](#)].
- [65] J. Huchra, M. Davis, D. Latham and J. Tonry, *A survey of galaxy redshifts. IV - The data*, *Astrophysical Journal Supplement Series* **52** (June, 1983) 89.
- [66] M.J. Geller and J.P. Huchra, *Groups of galaxies. III - The CfA survey*, *Astrophysical Journal Supplement Series* **52** (June, 1983) 61.
- [67] **SDSS** Collaboration, K.N. Abazajian et al., *The Seventh Data Release of the Sloan Digital Sky Survey*, *Astrophys. J. Suppl.* **182** (2009) 543 [[arXiv:0812.0649](#)].
- [68] A.H. Guth, *The Inflationary Universe: A Possible Solution to the Horizon and Flatness Problems*, *Phys. Rev.* **D23** (1981) 347.
- [69] A.D. Linde, *A New Inflationary Universe Scenario: A Possible Solution of the Horizon, Flatness, Homogeneity, Isotropy and Primordial Monopole Problems*, *Phys. Lett.* **108B** (1982) 389.
- [70] **SDSS** Collaboration, W.J. Percival et al., *Baryon Acoustic Oscillations in the Sloan Digital Sky Survey Data Release 7 Galaxy Sample*, *Mon. Not. Roy. Astron. Soc.* **401** (2010) 2148 [[arXiv:0907.1660](#)].
- [71] V. Springel et al., *Simulating the joint evolution of quasars, galaxies and their large-scale distribution*, *Nature* **435** (2005) 629 [[astro-ph/0504097](#)].
- [72] V. Springel, C.S. Frenk and S.D.M. White, *The large-scale structure of the Universe*, *Nature* **440** (2006) 1137 [[astro-ph/0604561](#)].

- [73] K. Jedamzik and M. Pospelov, *Big Bang Nucleosynthesis and Particle Dark Matter*, *New J. Phys.* **11** (2009) 105028 [[arXiv:0906.2087](#)].
- [74] K. Freese, *Status of Dark Matter in the Universe*, *Int. J. Mod. Phys.* **1** (2017) 325 [[arXiv:1701.0184](#)].
- [75] M. Markevitch, A.H. Gonzalez, L. David, A. Vikhlinin, S. Murray, W. Forman, C. Jones and W. Tucker, *A Textbook example of a bow shock in the merging galaxy cluster 1E0657-56*, *Astrophys. J.* **567** (2002) L27 [[astro-ph/0110468](#)].
- [76] D. Clowe, A. Gonzalez and M. Markevitch, *Weak lensing mass reconstruction of the interacting cluster 1E0657-558: Direct evidence for the existence of dark matter*, *Astrophys. J.* **604** (2004) 596 [[astro-ph/0312273](#)].
- [77] D. Clowe, M. Bradac, A.H. Gonzalez, M. Markevitch, S.W. Randall, C. Jones and D. Zaritsky, *A direct empirical proof of the existence of dark matter*, *Astrophys. J.* **648** (2006) L109 [[astro-ph/0608407](#)].
- [78] R. Thompson, R. Dav'e and K. Nagamine, *The rise and fall of a challenger: the Bullet Cluster in  $\Lambda$ CDM cold dark matter simulations*, *Mon. Not. Roy. Astron. Soc.* **452** (2015) 3030 [[arXiv:1410.7438](#)].
- [79] S.W. Randall, M. Markevitch, D. Clowe, A.H. Gonzalez and M. Bradac, *Constraints on the Self-Interaction Cross-Section of Dark Matter from Numerical Simulations of the Merging Galaxy Cluster 1E 0657-56*, *Astrophys. J.* **679** (2008) 1173 [[arXiv:0704.0261](#)].
- [80] R. Massey, T. Kitching and J. Richard, *The dark matter of gravitational lensing*, *Rept. Prog. Phys.* **73** (2010) 086901 [[arXiv:1001.1739](#)].
- [81] M. Bradac, S.W. Allen, T. Treu, H. Ebeling, R. Massey, R.G. Morris, A. von der Linden and D. Applegate, *Revealing the properties of dark matter in the merging cluster MACSJ0025.4-1222*, *Astrophys. J.* **687** (2008) 959 [[arXiv:0806.2320](#)].
- [82] A. Mahdavi, H.y. Hoekstra, A.y. Babul, D.y. Balam and P. Capak, *A Dark Core in Abell 520*, *Astrophys. J.* **668** (2007) 806 [[arXiv:0706.3048](#)].
- [83] M. Girardi, R. Barrena, W. Boschin and E. Ellingson, *Cluster Abell 520: a perspective based on member galaxies. A cluster forming at the crossing of three filaments?*, *Astron. Astrophys.* **491** (2008) 379 [[arXiv:0809.3139](#)].
- [84] J. Binney and S. Tremaine, *Galactic Dynamics: Second Edition*, Princeton University Press (2008).

- [85] G. Bertone et al., *Particle Dark Matter: Observations, Models and Searches*, Cambridge Univ. Press, Cambridge (2010).
- [86] J. Stadel, D. Potter, B. Moore, J. Diemand, P. Madau, M. Zemp, M. Kuhlen and V. Quilis, *Quantifying the heart of darkness with GHALO - a multi-billion particle simulation of our galactic halo*, *Mon. Not. Roy. Astron. Soc.* **398** (2009) L21 [[arXiv:0808.2981](#)].
- [87] J. Diemand, M. Kuhlen, P. Madau, M. Zemp, B. Moore, D. Potter and J. Stadel, *Clumps and streams in the local dark matter distribution*, *Nature* **454** (2008) 735 [[arXiv:0805.1244](#)].
- [88] V. Springel, J. Wang, M. Vogelsberger, A. Ludlow, A. Jenkins, A. Helmi, J.F. Navarro, C.S. Frenk and S.D.M. White, *The Aquarius Project: the subhalos of galactic halos*, *Mon. Not. Roy. Astron. Soc.* **391** (2008) 1685 [[arXiv:0809.0898](#)].
- [89] C. Kelso, C. Savage, M. Valluri, K. Freese, G.S. Stinson and J. Bailin, *The impact of baryons on the direct detection of dark matter*, *JCAP* **1608** (2016) 071 [[arXiv:1601.0472](#)].
- [90] A.M. Green, *Astrophysical uncertainties on direct detection experiments*, *Mod. Phys. Lett.* **A27** (2012) 1230004 [[arXiv:1112.0524](#)].
- [91] K. Kadota, T. Sekiguchi and H. Tashiro, *A new constraint on millicharged dark matter from galaxy clusters*, [arXiv:1602.0400](#).
- [92] C. Kouvaris, *Composite Millicharged Dark Matter*, *Phys. Rev.* **D88** (2013) 015001 [[arXiv:1304.7476](#)].
- [93] R. Barkana, N.J. Outmezguine, D. Redigolo and T. Volansky, *Signs of Dark Matter at 21-cm?*, [arXiv:1803.0309](#).
- [94] J.R. Bond, G. Efstathiou and J. Silk, *Massive Neutrinos and the Large Scale Structure of the Universe*, *Phys. Rev. Lett.* **45** (1980) 1980.
- [95] Chicago Univ. Press, , (Chicago, IL), Chicago Univ. Press, 1986.
- [96] J. Lesgourgues and S. Pastor, *Massive neutrinos and cosmology*, *Phys. Rept.* **429** (2006) 307 [[astro-ph/0603494](#)].
- [97] I.G. McCarthy, S. Bird, J. Schaye, J. Harnois-Deraps, A.S. Font and L. Van Waerbeke, *The BAHAMAS project: the CMB-large-scale structure tension and the roles of massive neutrinos and galaxy formation*, *Mon. Not. Roy. Astron. Soc.* **476** (2018) 2999 [[arXiv:1712.0241](#)].
- [98] A. Ibarra, *Neutrinos and dark matter*, *AIP Conf. Proc.* **1666** (2015) 140004.

- [99] G. Jungman, M. Kamionkowski and K. Griest, *Supersymmetric dark matter*, *Phys. Rept.* **267** (1996) 195 [[hep-ph/9506380](#)].
- [100] **ATLAS, CMS** Collaboration, C. Seitz, *Searches for strong production of supersymmetry at ATLAS and CMS*, in *5th Large Hadron Collider Physics Conference (LHCP 2017) Shanghai, China, May 15-20, 2017*, 2017. [arXiv:1710.0532](#).
- [101] I. Hinchliffe, F.E. Paige, M.D. Shapiro, J. Soderqvist and W. Yao, *Precision SUSY measurements at CERN LHC*, *Phys. Rev.* **D55** (1997) 5520 [[hep-ph/9610544](#)].
- [102] K.L. Chan, U. Chattopadhyay and P. Nath, *Naturalness, weak scale supersymmetry and the prospect for the observation of supersymmetry at the Tevatron and at the CERN LHC*, *Phys. Rev.* **D58** (1998) 096004 [[hep-ph/9710473](#)].
- [103] F.E. Paige, *Supersymmetry signatures at the CERN LHC*, in *Supersymmetry, supergravity and supercolliders. Proceedings, Theoretical Advanced Study Institute in elementary particle physics, TASI97, Boulder, USA, June 2-27, 1997*, p. 435, 1997. [hep-ph/9801254](#).
- [104] R.D. Peccei and H.R. Quinn, *CP Conservation in the Presence of Instantons*, *Phys. Rev. Lett.* **38** (1977) 1440.
- [105] P.W. Graham and S. Rajendran, *New Observables for Direct Detection of Axion Dark Matter*, *Phys. Rev.* **D88** (2013) 035023 [[arXiv:1306.6088](#)].
- [106] M.P. Hertzberg, M. Tegmark and F. Wilczek, *Axion Cosmology and the Energy Scale of Inflation*, *Phys. Rev.* **D78** (2008) 083507 [[arXiv:0807.1726](#)].
- [107] **Particle Data Group** Collaboration, K.A. Olive et al., *Review of Particle Physics*, *Chin. Phys.* **C38** (2014) 090001.
- [108] L. Bergstrom, *Dark Matter Candidates*, *New J. Phys.* **11** (2009) 105006 [[arXiv:0903.4849](#)].
- [109] M. Drewes, *The Phenomenology of Right Handed Neutrinos*, *Int. J. Mod. Phys.* **E22** (2013) 1330019 [[arXiv:1303.6912](#)].
- [110] S. Tremaine and J.E. Gunn, *Dynamical Role of Light Neutral Leptons in Cosmology*, *Phys. Rev. Lett.* **42** (1979) 407.
- [111] A. Boyarsky, O. Ruchayskiy and D. Iakubovskiy, *A Lower bound on the mass of Dark Matter particles*, *JCAP* **0903** (2009) 005 [[arXiv:0808.3902](#)].



- [112] M. Drewes et al., *A White Paper on keV Sterile Neutrino Dark Matter*, *JCAP* **1701** (2017) 025 [[arXiv:1602.0481](#)].
- [113] A. Boyarsky, O. Ruchayskiy and M. Shaposhnikov, *The Role of sterile neutrinos in cosmology and astrophysics*, *Ann. Rev. Nucl. Part. Sci.* **59** (2009) 191 [[arXiv:0901.0011](#)].
- [114] S. Dodelson and L.M. Widrow, *Sterile-neutrinos as dark matter*, *Phys. Rev. Lett.* **72** (1994) 17 [[hep-ph/9303287](#)].
- [115] A.D. Dolgov and S.H. Hansen, *Massive sterile neutrinos as warm dark matter*, *Astropart. Phys.* **16** (2002) 339 [[hep-ph/0009083](#)].
- [116] K. Abazajian, G.M. Fuller and M. Patel, *Sterile neutrino hot, warm, and cold dark matter*, *Phys. Rev.* **D64** (2001) 023501 [[astro-ph/0101524](#)].
- [117] K. Abazajian, G.M. Fuller and W.H. Tucker, *Direct detection of warm dark matter in the X-ray*, *Astrophys. J.* **562** (2001) 593 [[astro-ph/0106002](#)].
- [118] A. Kusenko, *Sterile neutrinos: The Dark side of the light fermions*, *Phys. Rept.* **481** (2009) 1 [[arXiv:0906.2968](#)].
- [119] S. Hannestad, *What is the lowest possible reheating temperature?*, *Phys. Rev.* **D70** (2004) 043506 [[astro-ph/0403291](#)].
- [120] J. Martin, C. Ringeval and V. Vennin, *Observing Inflationary Reheating*, *Phys. Rev. Lett.* **114** (2015) 081303 [[arXiv:1410.7958](#)].
- [121] M. Drewes, *What can the CMB tell about the microphysics of cosmic reheating?*, *JCAP* **1603** (2016) 013 [[arXiv:1511.0328](#)].
- [122] X.D. Shi and G.M. Fuller, *A New dark matter candidate: Nonthermal sterile neutrinos*, *Phys. Rev. Lett.* **82** (1999) 2832 [[astro-ph/9810076](#)].
- [123] L. Wolfenstein, *Neutrino Oscillations in Matter*, *Phys. Rev.* **D17** (1978) 2369.
- [124] S.P. Mikheev and A.Yu. Smirnov, *Resonance Amplification of Oscillations in Matter and Spectroscopy of Solar Neutrinos*, *Sov. J. Nucl. Phys.* **42** (1985) 913.
- [125] A. Boyarsky, J. Lesgourgues, O. Ruchayskiy and M. Viel, *Realistic sterile neutrino dark matter with keV mass does not contradict cosmological bounds*, *Phys. Rev. Lett.* **102** (2009) 201304 [[arXiv:0812.3256](#)].
- [126] C.T. Kishimoto, G.M. Fuller and C.J. Smith, *Coherent Active-Sterile Neutrino Flavor Transformation in the Early Universe*, *Phys. Rev. Lett.* **97** (2006) 141301 [[astro-ph/0607403](#)].

- [127] A. Boyarsky, J. Lesgourgues, O. Ruchayskiy and M. Viel, *Lyman-alpha constraints on warm and on warm-plus-cold dark matter models*, *JCAP* **0905** (2009) 012 [[arXiv:0812.0010](#)].
- [128] T. Asaka, M. Shaposhnikov and A. Kusenko, *Opening a new window for warm dark matter*, *Phys. Lett.* **B638** (2006) 401 [[hep-ph/0602150](#)].
- [129] F. Bezrukov and D. Gorbunov, *Light inflaton Hunter's Guide*, *JHEP* **05** (2010) 010 [[arXiv:0912.0390](#)].
- [130] A. Kusenko, *Sterile neutrinos, dark matter, and the pulsar velocities in models with a Higgs singlet*, *Phys. Rev. Lett.* **97** (2006) 241301 [[hep-ph/0609081](#)].
- [131] A. Kusenko, B.P. Mandal and A. Mukherjee, *Delayed pulsar kicks from the emission of sterile neutrinos*, *Phys. Rev.* **D77** (2008) 123009 [[arXiv:0801.4734](#)].
- [132] M. Klasen and C.E. Yaguna, *Warm and cold fermionic dark matter via freeze-in*, *JCAP* **1311** (2013) 039 [[arXiv:1309.2777](#)].
- [133] A. Merle, V. Niro and D. Schmidt, *New Production Mechanism for keV Sterile Neutrino Dark Matter by Decays of Frozen-In Scalars*, *JCAP* **1403** (2014) 028 [[arXiv:1306.3996](#)].
- [134] D. Boyanovsky, *Clustering properties of a sterile neutrino dark matter candidate*, *Phys. Rev.* **D78** (2008) 103505 [[arXiv:0807.0646](#)].
- [135] B. Shuve and I. Yavin, *Dark matter progenitor: Light vector boson decay into sterile neutrinos*, *Phys. Rev.* **D89** (2014) 113004 [[arXiv:1403.2727](#)].
- [136] A.V. Patwardhan, G.M. Fuller, C.T. Kishimoto and A. Kusenko, *Diluted equilibrium sterile neutrino dark matter*, *Phys. Rev.* **D92** (2015) 103509 [[arXiv:1507.0197](#)].
- [137] L. Baudis, *Dark matter searches*, *Annalen Phys.* **528** (2016) 74 [[arXiv:1509.0086](#)].
- [138] K. Griest and M. Kamionkowski, *Unitarity Limits on the Mass and Radius of Dark Matter Particles*, *Phys. Rev. Lett.* **64** (1990) 615.
- [139] M.W. Goodman and E. Witten, *Detectability of Certain Dark Matter Candidates*, *Phys. Rev.* **D31** (1985) 3059.
- [140] O. Bienaymé et al., *Weighing the local dark matter with RAVE red clump stars*, *Astron. Astrophys.* **571** (2014) A92 [[arXiv:1406.6896](#)].

- [141] K. Choi, C. Rott and Y. Itow, *Impact of the dark matter velocity distribution on capture rates in the Sun*, *JCAP* **1405** (2014) 049 [[arXiv:1312.0273](#)].
- [142] B. Moore, *Evidence against dissipationless dark matter from observations of galaxy haloes*, *Nature* **370** (1994) 629.
- [143] A. Pontzen and F. Governato, *How supernova feedback turns dark matter cusps into cores*, *Mon. Not. Roy. Astron. Soc.* **421** (2012) 3464 [[arXiv:1106.0499](#)].
- [144] F. Governato, A. Zolotov, A. Pontzen, C. Christensen, S.H. Oh, A.M. Brooks, T. Quinn, S. Shen and J. Wadsley, *Cuspy No More: How Outflows Affect the Central Dark Matter and Baryon Distribution in Lambda CDM Galaxies*, *Mon. Not. Roy. Astron. Soc.* **422** (2012) 1231 [[arXiv:1202.0554](#)].
- [145] J.F. Navarro, C.S. Frenk and S.D.M. White, *The Structure of cold dark matter halos*, *Astrophys. J.* **462** (1996) 563 [[astro-ph/9508025](#)].
- [146] J.F. Navarro, C.S. Frenk and S.D.M. White, *A Universal density profile from hierarchical clustering*, *Astrophys. J.* **490** (1997) 493 [[astro-ph/9611107](#)].
- [147] M. Srednicki, K.A. Olive and J. Silk, *High-Energy Neutrinos from the Sun and Cold Dark Matter*, *Nucl. Phys.* **B279** (1987) 804.
- [148] **IceCube** Collaboration, M.G. Aartsen et al., *Search for annihilating dark matter in the Sun with 3 years of IceCube data*, *Eur. Phys. J.* **C77** (2017) 146 [[arXiv:1612.0594](#)].
- [149] **PICO** Collaboration, C. Amole et al., *Dark Matter Search Results from the PICO-60 C<sub>3</sub>F<sub>8</sub> Bubble Chamber*, *Phys. Rev. Lett.* **118** (2017) 251301 [[arXiv:1702.0766](#)].
- [150] **Super-Kamiokande** Collaboration, K. Choi et al., *Search for neutrinos from annihilation of captured low-mass dark matter particles in the Sun by Super-Kamiokande*, *Phys. Rev. Lett.* **114** (2015) 141301 [[arXiv:1503.0485](#)].
- [151] P. Scott, *Neutrino telescope searches for dark matter in the Sun*, in *Rencontres du Vietnam: Neutrinos 2017 Quy Nhon, Vietnam, July 16-22, 2017*, 2017. [[arXiv:1710.0519](#)].
- [152] R. Shrock, *Decay  $L^0 \rightarrow \nu_l \gamma$  in gauge theories of weak and electromagnetic interactions*, *Phys. Rev.* **D9** (1974) 743.

- [153] R.E. Shrock, *Electromagnetic Properties and Decays of Dirac and Majorana Neutrinos in a General Class of Gauge Theories*, *Nucl. Phys.* **B206** (1982) 359.
- [154] E. Bulbul, M. Markevitch, A. Foster, R.K. Smith, M. Loewenstein and S.W. Randall, *Detection of An Unidentified Emission Line in the Stacked X-ray spectrum of Galaxy Clusters*, *Astrophys. J.* **789** (2014) 13 [[arXiv:1402.2301](#)].
- [155] A. Boyarsky, O. Ruchayskiy, D. Iakubovskiy and J. Franse, *Unidentified Line in X-Ray Spectra of the Andromeda Galaxy and Perseus Galaxy Cluster*, *Phys. Rev. Lett.* **113** (2014) 251301 [[arXiv:1402.4119](#)].
- [156] A. Boyarsky, J. Franse, D. Iakubovskiy and O. Ruchayskiy, *Checking the Dark Matter Origin of a 3.53 keV Line with the Milky Way Center*, *Phys. Rev. Lett.* **115** (2015) 161301 [[arXiv:1408.2503](#)].
- [157] T.E. Jeltema and S. Profumo, *Discovery of a 3.5 keV line in the Galactic Centre and a critical look at the origin of the line across astronomical targets*, *Mon. Not. Roy. Astron. Soc.* **450** (2015) 2143 [[arXiv:1408.1699](#)].
- [158] M.E. Anderson, E. Churazov and J.N. Bregman, *Non-Detection of X-Ray Emission From Sterile Neutrinos in Stacked Galaxy Spectra*, *Mon. Not. Roy. Astron. Soc.* **452** (2015) 3905 [[arXiv:1408.4115](#)].
- [159] L. Gu, J. Kaastra, A.J.J. Raassen, P.D. Mullen, R.S. Cumbee, D. Lyons and P.C. Stancil, *A novel scenario for the possible X-ray line feature at 3.5 keV: Charge exchange with bare sulfur ions*, *Astron. Astrophys.* **584** (2015) L11 [[arXiv:1511.0655](#)].
- [160] C. Shah, S. Dobrodey, S. Bernitt, R. Steinbruegge, J.R.C. López-Urrutia, L. Gu and J. Kaastra, *Laboratory measurements compellingly support charge-exchange mechanism for the 'dark matter'  $\sim 3.5$  keV X-ray line*, *Astrophys. J.* **833** (2016) 52 [[arXiv:1608.0475](#)].
- [161] K.N. Abazajian, *Sterile neutrinos in cosmology*, *Phys. Rept.* **711-712** (2017) 1 [[arXiv:1705.0183](#)].
- [162] S. Mertens, T. Lasserre, S. Groh, G. Drexlin, F. Glueck, A. Huber, A.W.P. Poon, M. Steidl, N. Steinbrink and C. Weinheimer, *Sensitivity of Next-Generation Tritium Beta-Decay Experiments for keV-Scale Sterile Neutrinos*, *JCAP* **1502** (2015) 020 [[arXiv:1409.0920](#)].
- [163] M. Viel, G.D. Becker, J.S. Bolton and M.G. Haehnelt, *Warm dark matter as a solution to the small scale crisis: New constraints from high redshift*

- Lyman- $\alpha$  forest data*, *Phys. Rev.* **D88** (2013) 043502  
[arXiv:1306.2314].
- [164] J. Goodman and W. Shepherd, *LHC Bounds on UV-Complete Models of Dark Matter*, arXiv:1111.2359.
- [165] G. Busoni, A. De Simone, T. Jacques, E. Morgante and A. Riotto, *On the Validity of the Effective Field Theory for Dark Matter Searches at the LHC Part III: Analysis for the  $t$ -channel*, *JCAP* **1409** (2014) 022  
[arXiv:1405.3101].
- [166] O. Buchmueller, M.J. Dolan and C. McCabe, *Beyond Effective Field Theory for Dark Matter Searches at the LHC*, *JHEP* **01** (2014) 025  
[arXiv:1308.6799].
- [167] A. Del Popolo and M. Le Delliou, *Small scale problems of the  $\Lambda$ CDM model: a short review*, *Galaxies* **5** (2017) 17 [arXiv:1606.0779].
- [168] S.S. McGaugh, *A Novel Test of the Modified Newtonian Dynamics with Gas Rich Galaxies*, *Phys. Rev. Lett.* **106** (2011) 121303 [arXiv:1102.3913].  
[Erratum: *Phys. Rev. Lett.*107,229901(2011)].
- [169] R.A. Flores and J.R. Primack, *Observational and theoretical constraints on singular dark matter halos*, *Astrophys. J.* **427** (1994) L1  
[astro-ph/9402004].
- [170] B. Moore, T.R. Quinn, F. Governato, J. Stadel and G. Lake, *Cold collapse and the core catastrophe*, *Mon. Not. Roy. Astron. Soc.* **310** (1999) 1147  
[astro-ph/9903164].
- [171] A.A. Klypin, A.V. Kravtsov, O. Valenzuela and F. Prada, *Where are the missing Galactic satellites?*, *Astrophys. J.* **522** (1999) 82  
[astro-ph/9901240].
- [172] M. Boylan-Kolchin, J.S. Bullock and M. Kaplinghat, *Too big to fail? The puzzling darkness of massive Milky Way subhaloes*, *Mon. Not. Roy. Astron. Soc.* **415** (2011) L40 [arXiv:1103.0007].
- [173] D.V. Stark, S.S. McGaugh and R.A. Swaters, *A First Attempt to Calibrate the Baryonic Tully-Fisher Relation with Gas Dominated Galaxies*, *Astron. J.* **138** (2009) 392 [arXiv:0905.4528].
- [174] L.V. Sales et al., *The low-mass end of the baryonic Tully-Fisher relation*, *Mon. Not. Roy. Astron. Soc.* **464** (2017) 2419 [arXiv:1602.0215].

- [175] F. Governato et al., *At the heart of the matter: the origin of bulgeless dwarf galaxies and Dark Matter cores*, *Nature* **463** (2010) 203 [[arXiv:0911.2237](#)].
- [176] S. Mashchenko, H.M.P. Couchman and J. Wadsley, *Cosmological puzzle resolved by stellar feedback in high redshift galaxies*, *Nature* **442** (2006) 539 [[astro-ph/0605672](#)].
- [177] A. Del Popolo, *The Cusp/Core problem and the Secondary Infall Model*, *Astrophys. J.* **698** (2009) 2093 [[arXiv:0906.4447](#)].
- [178] A. El-Zant, I. Shlosman and Y. Hoffman, *Dark halos: the flattening of the density cusp by dynamical friction*, *Astrophys. J.* **560** (2001) 636 [[astro-ph/0103386](#)].
- [179] T. Goerdt and A. Burkert, *The co-planarity of satellite galaxies delivered by randomly aligned cold mode accretion streams*, [arXiv:1307.2102](#).
- [180] **Super-Kamiokande** Collaboration, Y. Fukuda et al., *Evidence for oscillation of atmospheric neutrinos*, *Phys. Rev. Lett.* **81** (1998) 1562 [[hep-ex/9807003](#)].
- [181] **SNO** Collaboration, Q.R. Ahmad et al., *Direct evidence for neutrino flavor transformation from neutral current interactions in the Sudbury Neutrino Observatory*, *Phys. Rev. Lett.* **89** (2002) 011301 [[nucl-ex/0204008](#)].
- [182] B. Pontecorvo, *Inverse beta processes and nonconservation of lepton charge*, *Sov. Phys. JETP* **7** (1958) 172. [*Zh. Eksp. Teor. Fiz.*34,247(1957)].
- [183] I. Esteban, M.C. Gonzalez-Garcia, M. Maltoni, I. Martinez-Soler and T. Schwetz, *Updated fit to three neutrino mixing: exploring the accelerator-reactor complementarity*, *JHEP* **01** (2017) 087 [[arXiv:1611.0151](#)].
- [184] P.F. de Salas, D.V. Forero, C.A. Ternes, M. Tortola and J.W.F. Valle, *Status of neutrino oscillations 2018: first hint for normal mass ordering and improved CP sensitivity*, [arXiv:1708.0118](#).
- [185] F. Capozzi, E. Di Valentino, E. Lisi, A. Marrone, A. Melchiorri and A. Palazzo, *Global constraints on absolute neutrino masses and their ordering*, *Phys. Rev.* **D95** (2017) 096014 [[arXiv:1703.0447](#)].
- [186] S. Gariazzo, M. Archidiacono, P.F. de Salas, O. Mena, C.A. Ternes and M. Tortola, *Neutrino masses and their ordering: Global Data, Priors and Models*, *JCAP* **1803** (2018) 011 [[arXiv:1801.0494](#)].

- [187] X. Qian and P. Vogel, *Neutrino Mass Hierarchy*, *Prog. Part. Nucl. Phys.* **83** (2015) 1 [[arXiv:1505.0189](#)].
- [188] P. Huber, M. Lindner, M. Rolinec, T. Schwetz and W. Winter, *Prospects of accelerator and reactor neutrino oscillation experiments for the coming ten years*, *Phys. Rev.* **D70** (2004) 073014 [[hep-ph/0403068](#)].
- [189] D. Franco, C. Jollet, A. Kouchner, V. Kulikovskiy, A. Meregaglia, S. Perasso, T. Pradier, A. Tonazzo and V. Van Elewyck, *Mass hierarchy discrimination with atmospheric neutrinos in large volume ice/water Cherenkov detectors*, *JHEP* **04** (2013) 008 [[arXiv:1301.4332](#)].
- [190] A.S. Dighe, M.T. Keil and G.G. Raffelt, *Detecting the neutrino mass hierarchy with a supernova at IceCube*, *JCAP* **0306** (2003) 005 [[hep-ph/0303210](#)].
- [191] W. Rodejohann, *Neutrino-less Double Beta Decay and Particle Physics*, *Int. J. Mod. Phys.* **E20** (2011) 1833 [[arXiv:1106.1334](#)].
- [192] J. Engel and J. Menéndez, *Status and Future of Nuclear Matrix Elements for Neutrinoless Double-Beta Decay: A Review*, *Rept. Prog. Phys.* **80** (2017) 046301 [[arXiv:1610.0654](#)].
- [193] E.W. Otten and C. Weinheimer, *Neutrino mass limit from tritium beta decay*, *Rept. Prog. Phys.* **71** (2008) 086201 [[arXiv:0909.2104](#)].
- [194] K.N. Abazajian et al., *Cosmological and Astrophysical Neutrino Mass Measurements*, *Astropart. Phys.* **35** (2011) 177 [[arXiv:1103.5083](#)].
- [195] S.M. Bilenky, C. Giunti, J.A. Grifols and E. Masso, *Absolute values of neutrino masses: Status and prospects*, *Phys. Rept.* **379** (2003) 69 [[hep-ph/0211462](#)].
- [196] H. Pas and T.J. Weiler, *Absolute neutrino mass determination*, *Phys. Rev.* **D63** (2001) 113015 [[hep-ph/0101091](#)].
- [197] **Daya Bay** Collaboration, F.P. An et al., *Observation of electron-antineutrino disappearance at Daya Bay*, *Phys. Rev. Lett.* **108** (2012) 171803 [[arXiv:1203.1669](#)].
- [198] **Daya Bay** Collaboration, F.P. An et al., *Spectral measurement of electron antineutrino oscillation amplitude and frequency at Daya Bay*, *Phys. Rev. Lett.* **112** (2014) 061801 [[arXiv:1310.6732](#)].
- [199] **RENO** Collaboration, J.K. Ahn et al., *Observation of Reactor Electron Antineutrino Disappearance in the RENO Experiment*, *Phys. Rev. Lett.* **108** (2012) 191802 [[arXiv:1204.0626](#)].

- [200] **Double Chooz** Collaboration, Y. Abe et al., *Indication of Reactor  $\bar{\nu}_e$  Disappearance in the Double Chooz Experiment*, *Phys. Rev. Lett.* **108** (2012) 131801 [[arXiv:1112.6353](#)].
- [201] C. Jarlskog, *A Basis Independent Formulation of the Connection Between Quark Mass Matrices, CP Violation and Experiment*, *Z. Phys.* **C29** (1985) 491.
- [202] **Particle Data Group** Collaboration, C. Patrignani et al., *Review of Particle Physics*, *Chin. Phys.* **C40** (2016) 100001.
- [203] M. Fukugita and T. Yanagida, *Baryogenesis Without Grand Unification*, *Phys. Lett.* **B174** (1986) 45.
- [204] L. Covi, E. Roulet and F. Vissani, *CP violating decays in leptogenesis scenarios*, *Phys. Lett.* **B384** (1996) 169 [[hep-ph/9605319](#)].
- [205] R.N. Mohapatra and A.Y. Smirnov, *Neutrino Mass and New Physics*, *Ann. Rev. Nucl. Part. Sci.* **56** (2006) 569 [[hep-ph/0603118](#)].
- [206] S. Weinberg, *Baryon and Lepton Nonconserving Processes*, *Phys. Rev. Lett.* **43** (1979) 1566.
- [207] P. Minkowski,  *$\mu \rightarrow e\gamma$  at a Rate of One Out of  $10^9$  Muon Decays?*, *Phys. Lett.* **67B** (1977) 421.
- [208] T. Yanagida, *HORIZONTAL SYMMETRY AND MASSES OF NEUTRINOS*, *Conf. Proc.* **C7902131** (1979) 95.
- [209] R.N. Mohapatra and G. Senjanovic, *Neutrino Mass and Spontaneous Parity Violation*, *Phys. Rev. Lett.* **44** (1980) 912.
- [210] M. Gell-Mann, P. Ramond and R. Slansky, *Complex Spinors and Unified Theories*, *Conf. Proc.* **C790927** (1979) 315 [[arXiv:1306.4669](#)].
- [211] M. Magg and C. Wetterich, *Neutrino Mass Problem and Gauge Hierarchy*, *Phys. Lett.* **94B** (1980) 61.
- [212] G. Lazarides, Q. Shafi and C. Wetterich, *Proton Lifetime and Fermion Masses in an  $SO(10)$  Model*, *Nucl. Phys.* **B181** (1981) 287.
- [213] R.N. Mohapatra and G. Senjanovic, *Neutrino Masses and Mixings in Gauge Models with Spontaneous Parity Violation*, *Phys. Rev.* **D23** (1981) 165.
- [214] R. Foot, H. Lew, X.G. He and G.C. Joshi, *Seesaw Neutrino Masses Induced by a Triplet of Leptons*, *Z. Phys.* **C44** (1989) 441.



- 
- [215] A. Zee, *A Theory of Lepton Number Violation, Neutrino Majorana Mass, and Oscillation*, *Phys. Lett.* **93B** (1980) 389. [Erratum: *Phys. Lett.* 95B,461(1980)].
- [216] A. Zee, *Quantum Numbers of Majorana Neutrino Masses*, *Nucl. Phys.* **B264** (1986) 99.
- [217] K.S. Babu, *Model of 'Calculable' Majorana Neutrino Masses*, *Phys. Lett.* **B203** (1988) 132.



# 2

## Simplified Models and Complementarity

### 2.1 Introduction

As we briefly discussed in section 1.3.5, simplified models of dark matter are designed in such a way that they only involve a few extra particles and interactions. They are usually intended to represent the low energy limit of a more general scenario in which most of the heavy states have been integrated out, leaving behind the dark matter particle and its mediator to the visible sector. As the complete model does not need to be unique, simplified models enable experimentalists/phenomenologists to cover a wide range in theory space.

Once a model of study has been established, the next stage is to determine its phenomenology. In this chapter we will consider in detail the experimental consequences of two such models. First, in section 2.2, we consider a Majorana fermion as the dark matter candidate and a  $Z'$  as its only mediator to the visible sector. We will see that all of the experimental techniques reviewed in section 1.3.4.1 are able to impose limits to this setup, with the exception of  $\gamma$ -telescopes. Coincidentally, these are the only type of detectors that need to be considered when constraining the model presented in section 2.3, where the mediator is a heavy right-handed neutrino that, due to its nature, has very feeble interactions with the SM particles. Throughout this section we will highlight the complementary potential that different experimental probes have when it comes to tackle simplified models.

## 2.2 The Dark Sequential $Z'$ Portal

In this section we will explore the phenomenology of a simplified model in which the dark matter particle is a Majorana fermion and the mediator is a vector boson with the same couplings as the SM  $Z$  boson. Majorana dark matter has been explored in different contexts in a number of papers [1-3], but here we restrict ourselves to a minimal extension of the SM which includes a Majorana fermion  $\chi$ , singlet under  $G_{\text{SM}}$ , as the sole constituent of dark matter. This choice has already some distinctive phenomenological consequences: in the context of direct detection, the SI interactions discussed in section 1.3.4.1 vanish at leading order, leaving a dominant contribution of the SD WIMP-nucleon scattering cross-section ( $\sigma_{\chi N}^{\text{SD}}$ ). The portal to the SM in this case will be provided by a spin-1  $Z'$ . These additional massive gauge bosons usually appear as a natural consequence of the SSB of enlarged symmetry groups (most commonly  $U(1)$  symmetries) and their couplings are dictated by the specific group choice. Since we aim to work in a minimal framework, we choose the couplings of  $Z'$  to be the same as those of the electroweak  $Z$  boson, a setup usually referred to as the sequential standard model (SSM). Hence the model has only three free parameters: the dark matter and the mediator masses,  $M_\chi$  and  $M_{Z'}$ , and the coupling of  $Z'$  to dark matter,  $g_\chi$ .

In order to constrain this model, we will cover the three approaches discussed in section 1.3.4.1: direct detection, indirect detection and collider searches. In this case however, and in stark contrast with the model we will present in section 2.3, indirect detection experiments like Fermi-LAT, H.E.S.S. or MAGIC do not have a sensitivity comparable to the other constraints considered, as discussed in detail in section 2.2.2. That being said, indirect detection of dark matter annihilating to neutrinos, as mentioned in section 1.3.4.1, has the special property of being sensitive to the WIMP-nucleon scattering processes occurring in the Sun's interior once equilibrium of solar capture and annihilation has been reached. Hence, limits coming from the IceCube neutrino detector are shown to be competitive with other Earth-based experiments like Liquid Xenon and Bubble Chamber detectors.

### 2.2.1 The Model

As we want  $Z'$  to be the only mediator of interactions between dark matter and SM particles, we need to assume that there is no mass nor kinetic mixing between  $Z$  and  $Z'$ . This can be achieved if the SM Higgs boson is not charged under the UV group whose breaking generates the massive gauge boson. We will not go deeper here as we are interested in the phenomenological aspects of

this framework for the moment. The interactions are then described by

$$\mathcal{L}_{int} = \left[ g_\chi \chi \gamma^\mu \gamma^5 \chi + \sum_{f \in \text{SM}} \bar{f} \gamma^\mu (g_{fv} + g_{fa} \gamma^5) f \right] Z'_\mu, \quad (2.1)$$

where the sum is over all the SM fermions and the factors  $g_{fv}$  and  $g_{fa}$  are given by,

$$\begin{aligned} g_{uv} &= \frac{-e}{4} \left( \frac{5}{3} \tan \theta_W - \cot \theta_W \right), & g_{ua} &= \frac{-e}{4} (\tan \theta_W + \cot \theta_W), \\ g_{dv} &= \frac{e}{4} \left( \frac{1}{3} \tan \theta_W - \cot \theta_W \right), & g_{da} &= \frac{e}{4} (\tan \theta_W + \cot \theta_W), \\ g_{\ell v} &= \frac{e}{4} (3 \tan \theta_W - \cot \theta_W), & g_{\ell a} &= \frac{e}{4} (\tan \theta_W + \cot \theta_W), \\ g_{\nu v} &= \frac{e}{4} (\tan \theta_W + \cot \theta_W), & g_{\nu a} &= \frac{-e}{4} (\tan \theta_W + \cot \theta_W), \end{aligned} \quad (2.2)$$

with  $u$ ,  $d$ ,  $\ell$  and  $\nu$  the up-type, down-type quarks, charged leptons and neutrinos respectively,  $e$  the electromagnetic coupling and  $\theta_W$  the Weinberg angle defined in eq. (1.11). We see in eq. (2.1) that the  $\chi$  vector currents do not appear, because of its Majorana nature.

## 2.2.2 The Constraints

### 2.2.2.1 Relic Abundance

From the list that we presented in section 1.3.3, related to the properties a good dark matter candidate must fulfil, probably the most important is to be able to reproduce the measured relic abundance:  $\Omega_{dm} h^2 = 0.1188 \pm 0.0010$ .

In order to obtain the relevant Feynman diagrams involved in thermal production, we can rewrite the Lagrangian of the model given in eq. (2.1) in terms of effective operators, as

$$\bar{f} \gamma^\mu f \chi \gamma_\mu \gamma^5 \chi \quad \text{and} \quad \bar{f} \gamma^\mu \gamma^5 f \chi \gamma_\mu \gamma^5 \chi. \quad (2.3)$$

They in turn generate the annihilations channels shown in fig. 2.1. In the left panel of fig. 2.1 we have an  $s$ -channel annihilation mediated by a  $Z'$  while in the right panel a  $t$ -channel annihilation to  $Z' Z'$  is shown.

The numerical calculation of the relic density is performed using the package `MicrOmegas` 4.3.2 [4, 5], the result of which can be seen as black isocontours in the  $M_{Z'} - M_\chi$ -plane labelled as  $\Omega h^2$  *allowed region* in figs. 2.5 to 2.7, where we summarise our results for three different values of  $g_\chi$ . To obtain analytical approximations, we perform a velocity expansion following the appendix

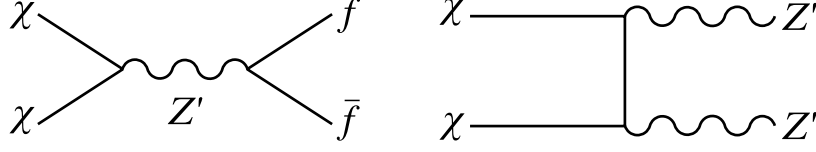


Figure 2.1: Feynman diagrams relevant for dark matter annihilation. Left panel: the  $Z'$  boson mediates s-channel annihilations to SM fermions. Right panel: t-channel decay to  $Z'$  pairs.

found in [6].<sup>1</sup> This leads to

$$\begin{aligned}
\langle\sigma v\rangle_{ff} &= \sum_f n_c^f \frac{2\sqrt{M_\chi^2 - m_f^2}}{\pi M_\chi M_{Z'}^4 (M_{Z'}^2 - 4M_\chi^2)^2} \left[ g_{fa}^2 g_\chi^2 m_f^2 (M_{Z'}^2 - 4M_\chi^2)^2 \right] \\
&\quad - \frac{v^2}{6\pi M_\chi M_{Z'}^4 \sqrt{M_\chi^2 - m_f^2} (M_{Z'}^2 - 4M_\chi^2)^3} \left[ g_{fa}^2 [-g_\chi^2 (M_{Z'}^2 - 4M_\chi^2) \right. \\
&\quad \times (23m_f^4 M_{Z'}^4 - 192m_f^2 M_\chi^6 - 4m_f^2 M_\chi^2 M_{Z'}^2 (30m_f^2 + 7M_{Z'}^2) \\
&\quad \left. + 8M_\chi^4 (30m_f^4 + 12m_f^2 M_{Z'}^2 + M_{Z'}^4))] \right] \\
&\quad + M_{Z'}^4 (g_{fv})^2 [4g_\chi^2 (M_f^4 + m_f^2 M_\chi^2 - 2M_\chi^4) (M_{Z'}^2 - 4M_\chi^2)] \Big], \tag{2.4}
\end{aligned}$$

$$\begin{aligned}
\langle\sigma v\rangle_{Z'Z'} &= \frac{g_\chi^4}{\pi M_\chi^2} \left(1 - \frac{M_{Z'}^2}{M_\chi^2}\right)^{\frac{3}{2}} \left(1 - \frac{M_{Z'}^2}{2M_\chi^2}\right)^{-2} \\
&\quad + \frac{g_\chi^4 v^2}{3\pi M_\chi^2} \sqrt{1 - \frac{M_{Z'}^2}{M_\chi^2}} \left(1 - \frac{M_{Z'}^2}{2M_\chi^2}\right)^{-4} \left(\frac{23}{16} \frac{M_{Z'}^6}{M_\chi^6} \right. \\
&\quad \left. - \frac{59}{8} \frac{M_{Z'}^4}{M_\chi^4} + \frac{43}{4} \frac{M_{Z'}^2}{M_\chi^2} + 2 - 12 \frac{M_\chi^2}{M_{Z'}^2} + 8 \frac{M_\chi^4}{M_{Z'}^4}\right) \tag{2.5}
\end{aligned}$$

Here  $n_c^f$  is the color factor, while  $g_{fv}$  and  $g_{fa}$  have been defined in eq. (2.2), taking  $f = u, d, e, \mu, \tau, \nu$ . In the first expression the sum runs over all final states that are kinematically accessible for a given value of the DM mass  $M_\chi$ . There are some remarks in order concerning the velocity expansions in eqs. (2.4) and (2.5):

- We can see in the expansion of  $\langle\sigma v\rangle_{ff}$  that the first term is velocity independent, but it is however helicity suppressed being dependent on  $m_f^2/M_{Z'}^4$ . This means that the s-wave term is highly suppressed unless

<sup>1</sup>The reason for using a full numerical calculation for the relic abundance instead of the simpler velocity expansion formulae is that the latter fail around the critical  $M_\chi \sim M_{Z'}/2$  resonance region [7].

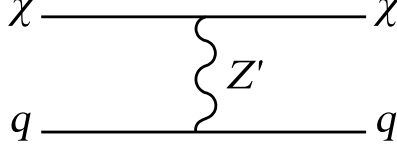


Figure 2.2: Feynman diagram relevant for direct detection. The dark matter scattering off nucleons occurs via  $t$ -channel  $Z'$  exchange.

top quarks are kinematically available. For this reason the p-wave term, which is velocity dependent, is dominant during thermal freeze-out when  $v \sim 0.3$  but is also highly suppressed today when  $v \sim 10^{-3}$ . This explains why indirect detection is suppressed in this framework. The annihilation into fermions can only be efficient today for  $M_\chi \gtrsim m_{top} \sim 200$  GeV, a mass range in which indirect detection probes are less sensitive concerning thermal dark matter.

- When decays to  $Z'$  pairs become kinematically allowed,  $\langle \sigma v \rangle_{Z'Z'}$  must be considered. The s-wave term, being dependent on  $1/M_\chi^2$  is subdominant, while the p-wave term is proportional to  $M_\chi^2/M_{Z'}^4$ . The annihilation grows then unbounded with  $M_\chi$ , which is a pathological behaviour. The reason behind this lies in the fact that we are considering a simplified model. Such behaviour will be analysed in detail in section 2.2.2.5.

### 2.2.2.2 Direct Detection

The first operator in eq. (2.3) generates a SI WIMP-nucleon interaction which is however velocity suppressed [8], thus we concentrate on the second operator generating SD interactions. These are mediated by the  $Z'$  boson as depicted in fig. 2.2 and described by the following cross section

$$\sigma_{\chi N}^{\text{SD}} = \frac{12\mu_{\chi N}^2}{\pi} \frac{g_\chi^2}{M_{Z'}^4} [g_{ua}\Delta_u^N + g_{da}(\Delta_d^N + \Delta_s^N)]^2 \quad \text{with } N = p, n, \quad (2.6)$$

where  $\mu_{\chi N}$  is the WIMP-nucleon reduced mass while  $\Delta_q^N$  are the quark spin fractions for each nucleon  $N$ , whose values can be found in [9].

The sensitivity of a given detector to  $\chi - p$  or  $\chi - n$  interactions is entirely dependent of the detector material of said detector. If this material presents an unpaired proton, it will be more sensitive to SD interactions to protons ( $SD_p$ ) like in the PICO-60 experiment whose detector consists of octafluoropropane,  $C_3F_8$ . The same is true for detectors with unpaired neutrons, being more sensitive to SD interactions to neutrons ( $SD_n$ ), like liquid xenon (LXe) experiments such as LUX or XENON1T. We discuss here these particular experiments and the constraints they offer.

The PICO-60 experiment consists of a superheated bubble chamber filled with  $52.2 \pm 0.5$  kg of  $C_3F_8$  operated at SNOLAB in Sudbury, Canada. It currently sets the strongest bounds on  $SD_p$  based on an exposure of 1167 kg-days of data taken between November 2016 and January 2017 and exclude a  $SD_p$  cross section of  $3.4 \times 10^{-41}$  cm<sup>2</sup> for a 30 GeV DM mass [10]. The limit imposed by this dataset can be seen as straight yellow lines in figs. 2.5 to 2.7. The LUX experiment is a dual phase time projection chamber (TPC), detecting energy depositions through the resulting ionization and scintillation in the 250 kg LXe target material (for more details see section 3.2) and operating at the Sanford Underground Research Facility in South Dakota, USA. Using 129.5 kg-year exposure, it excludes a  $SD_n$  cross section of  $1.6 \times 10^{-41}$  cm<sup>2</sup> for a 35 GeV DM mass [11]. This limit is represented by a green dashed line in figs. 2.5 to 2.7. Finally, the XENONIT experiment is also a dual phase TPC using  $1042 \pm 12$  kg fiducial mass of LXe operated at the Laboratori Nazionali del Gran Sasso (LNGS) in Italy. As the collaboration has not yet released data based on  $SD_n$  searches, we use a projection based on properly scaled XENON100 data [12]. As the XENONIT projected limit with 2 year-ton exposure is expected to improve the limits on SI cross sections by two orders of magnitude [13] we assumed the same scaling for the  $SD_n$ . This is shown as a light green line in figs. 2.5 to 2.7 while projected limits based on the 34 day-ton exposure dataset [14] are shown in dark green. The direct detection limits are simply straight lines in a log-log plot because the cross section in eq. (2.6) scales with the fourth power of  $M_{Z'}$ .

### 2.2.2.3 Indirect Detection

As already discussed in section 2.2.2, dark matter capture in the Sun can produce competitive limits due to its later annihilation into SM particles from which neutrinos can reach Earth. The amount of dark matter captured depends on the scattering of WIMPs off hydrogen, helium and oxygen while the annihilation is given by the expansion in eqs. (2.4) and (2.5) for  $v \sim 10^{-3}$  (dark matter velocity in the solar system). Once the equilibrium between these two processes is reached, we can drop the neutrino flux dependence on the annihilation and cast limits on the scattering cross section, even if the annihilation rate cannot be accessed through conventional indirect detection techniques. A residual dependence remains however, due to the fact that the annihilations final states modify the neutrino flux. With this taken into account, the capture rate can be written as [15]

$$C_{\text{DM}} = 10^{20} \text{s}^{-1} \left( \frac{1 \text{ TeV}}{M_\chi} \right)^2 \frac{2.77 \sigma_{SD_p} + 4270 \sigma_{SI_p}}{10^{-40} \text{cm}^{-2}} \quad (2.7)$$

for DM masses above 1 TeV.

As it can be seen from this equation, the observed flux of neutrinos on Earth



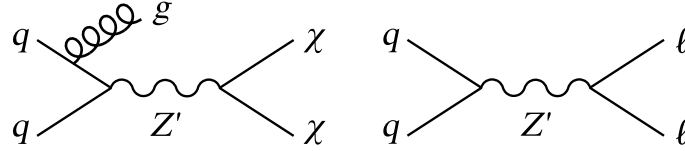


Figure 2.3: Feynman diagrams relevant for collider probes. Left panel: mono-jet searches for dark matter, where the  $Z'$  decays invisibly with a jet being radiated from the initial state. Right panel: resonant production of the  $Z'$  gauge boson. It is not sensitive to dark matter, but it restricts the  $Z'$  mass, which has a great impact on this particular model.

can be used to put constraints in both SI and SD interactions. Even more, those coming from SI interactions are stronger due to the larger factor in eq. (2.7): the limits imposed by the IceCube experiment for SI cross sections exclude values below  $10^{-43} \text{ cm}^2$  while for  $SD_p$  cross sections below  $10^{-40} \text{ cm}^2$  for  $M_\chi = 100 \text{ GeV}$  in the  $WW$  channel. Despite this, limits imposed by direct detection experiments on SI interactions like those coming from LUX or XENON1T are around  $10^{-45} \text{ cm}^2$  and hence, just the  $SD_p$  limits will be relevant. We will be probing then the same quantity as in section 2.2.2.2 (namely  $\sigma_{SD}$ ). This bound is shown as a blue dashed line in figs. 2.5 to 2.7. The irregular behaviour of this area can be explained by threshold effects near the top quark and the electroweak gauge bosons masses.

#### 2.2.2.4 Collider Searches

The dark matter limits obtained at colliders like the LHC come, as mentioned in section 2.2.2, from mono- $X$  searches. The most constraining are in this case those in which  $X$  are jets, as depicted in the left panel of fig. 2.3. We will also explore the impact of vector mediator searches at the LHC, providing complementary bounds. In order to do so, we include dilepton searches, whose tree-level diagram is shown in the right panel of fig. 2.3.

The mono-jet searches are, due to its nature, strongest for large values of  $g_\chi$  and valid just when the process is kinematically allowed, i.e. for  $M_\chi < M_{Z'}/2$ . This behaviour is evidenced in the red area shown in figs. 2.5 to 2.7, which provides rather weak exclusion limits. On the other hand, the dilepton limits turn out to be the most restrictive. They are based on ATLAS searches for the Sequential SM  $Z'$  decaying into charged leptons with an integrated luminosity of  $36.1 \text{ fb}^{-1}$  and 13 TeV center-of-mass-energy [16]. This limit can be seen in fig. 2.4, where the dielectron and the dimuon data has been combined. It has a wide uncertainty (gray area) because the sequential  $Z'$  presents a rather large decay width. The lower bound for  $Z'$  goes then from 4.3 to 4.8 TeV.

A modification to the ATLAS limit must be introduced, because our framework introduces an additional particle. Indeed, when  $2M_\chi > M_{Z'}$  a new channel

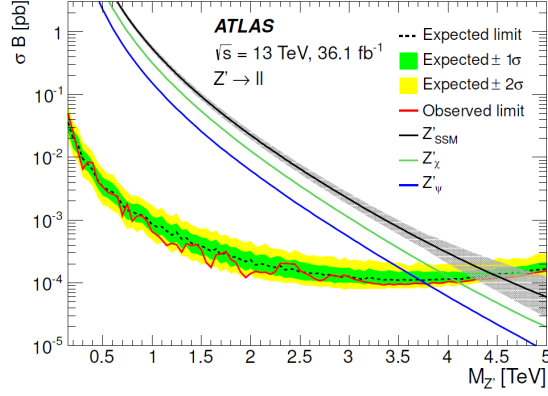


Figure 2.4: Upper 95% CL limits on the  $Z'$  production cross-section times branching ratio to two leptons of a single flavour as a function of  $Z'$  pole mass, measured by ATLAS. Results are shown for the combined dilepton channel. The Sequential SM, relevant for this work, is shown as a black line. Figure taken from [16].

opens, modifying the sequential  $Z'$  decay width in the following way [17]

$$\Gamma_{Z'} = \sum_{f \in \text{SM}} \theta(M_{Z'} - 2m_f) \frac{n_c M_{Z'}}{12\pi} \sqrt{1 - \frac{4m_f^2}{M_{Z'}^2}} \left[ g_{fv}^2 \left( 1 + \frac{2m_f^2}{M_{Z'}^2} \right) + g_{fa}^2 \left( 1 - \frac{4m_f^2}{M_{Z'}^2} \right) \right] \\ \theta(M_{Z'} - 2M_\chi) \frac{M_{Z'}}{12\pi} \sqrt{1 - \frac{4M_\chi^2}{M_{Z'}^2}} g_\chi^2 \left( 1 - \frac{4M_\chi^2}{M_{Z'}^2} \right), \quad (2.8)$$

where  $g_{fv}$  and  $g_{fa}$  are given in eq. (2.2) and  $\theta$  is the unit step function. The branching ratio on which the bounds are based ( $\text{Br}(Z'_{\text{SSM}} \rightarrow \ell\ell)$ ) becomes then

$$\frac{\Gamma(Z' \rightarrow \ell\ell)}{\Gamma(Z' \rightarrow ff)} \Rightarrow \frac{\Gamma(Z' \rightarrow \ell\ell)}{\Gamma(Z' \rightarrow ff) + \Gamma(Z' \rightarrow \chi\chi)} \\ = \frac{\Gamma(Z' \rightarrow \ell\ell)}{\Gamma(Z' \rightarrow ff)} (1 - \text{Br}(Z' \rightarrow \chi\chi)) \quad (2.9) \\ = \text{Br}(Z'_{\text{SSM}} \rightarrow \ell\ell) [1 - \text{Br}(Z' \rightarrow \chi\chi)]$$

where  $f$  is a SM fermion.

The LHC limits can be seen in figs. 2.5 and 2.6 as blue solid lines, from where it is clear that the effect of eq. (2.9) is stronger for higher values of  $g_\chi$ . In fig. 2.7 the limit is shown in blue dot-dashed because  $g_\chi = 4\pi$  is large enough to potentially break the narrow width approximation used to derive the ATLAS limits, hence this limit must not be taken at face value. Finally, we also show, in dotted dark blue, projected limits based on 14 TeV center-of-mass energy and an integrated

luminosity of  $1000 \text{ fb}^{-1}$ .<sup>2</sup> In case of null results, it would rule out masses up to  $M_\chi \approx 6.7 \text{ TeV}$ .

### 2.2.2.5 Perturbativity

We mentioned briefly in section 2.2.2.1 that the cross section of dark matter annihilation to  $Z'$  pairs exhibits an odd behaviour, scaling with  $M_\chi^2$ . This phenomenon is produced by a contribution of the longitudinal degrees of freedom of  $Z'$ , as discussed in [18, 19], which grows with  $s \sim 4M_\chi^2$ . Amplitudes increasing with the center-of-mass energy are a clear sign of unitarity violation and we must assess consequently the limit at which perturbativity breaks down in this particular framework. Following [18], we can express this limit as

$$\sqrt{s} < \frac{\pi M_{Z'}^2}{g_\chi^2 M_\chi}, \quad (2.10)$$

which can be in turn formulated, in the non-relativistic limit relevant for the DM relic density, as

$$M_\chi < \sqrt{\frac{\pi M_{Z'}^2}{2g_\chi^2}}. \quad (2.11)$$

This condition implies that, for the region above the black dashed line in figs. 2.5 to 2.7 additional degrees of freedom that unitarize the theory must be taken into account. In particular, for a UV-complete model in which the additional massive gauge boson arises from the SSB of a higher symmetry, the missing degree of freedom corresponds to the respective Higgs boson. This new scalar mediates the annihilation to  $Z'Z'$  via an  $s$ -channel diagram, restoring unitarity, as discussed in [20].

## 2.2.3 The Results

We will discuss in this section the insights that can be extracted from the results shown in figs. 2.5 to 2.7, in which all the bounds previously presented are shown in the  $M_{Z'} - M_\chi$ -plane, for three different values of the WIMP- $Z'$  coupling ( $g_\chi = 0.1, 1, 4\pi$ ). Concerning the relic abundance represented as black isocontours, we can see that for  $g_\chi = 0.1$ , it can be achieved just through annihilation to SM fermions around the resonance  $M_\chi \sim M_{Z'}/2$ , while for  $g_\chi = 1$  the annihilation to  $Z'$  pairs also contributes significantly. Finally for  $g_\chi = 4\pi$  this last process is too efficient, producing too small values for  $\Omega h^2$  around the resonant region. The right values can still be obtained through the annihilation to SM fermions, in this case away from the resonance.

<sup>2</sup><http://collider-reach.web.cern.ch/?rts1=13&lumi1=3.2&rts2=13&lumi2=13.3&pdf=MSTW2008nnlo68cl.LHgrid>

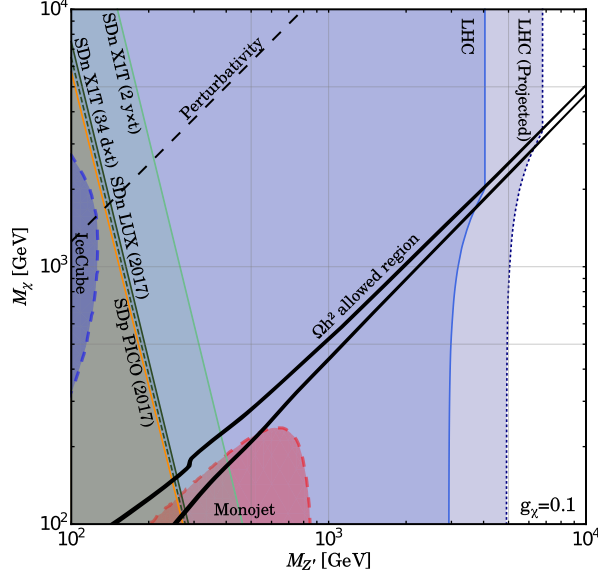


Figure 2.5: Exclusion limits for  $g_\chi = 0.1$ . The black solid curve outlines the region of parameter space with the correct relic density. From left to right: in blue dashed the parameter space excluded by IceCube; the orange solid line represents the current bound from PICO; the green dashed line the current bound from LUX on SD scattering off neutrons with 129.5 kg-year exposure; the solid green line the projected bound from XENONIT on SD scattering off neutrons with  $34 d \times t$  of exposure; further right in light green, we show the projected sensitivity from XENONIT on SD scattering off neutrons with  $2 y \times t$  exposure; the region above the black dashed line delimits the non-perturbative regime; the red dashed curve depicts the parameter space excluded by LHC based on mono-jet data; blue vertical solid (dotted) lines delimit the current (projected) LHC exclusion regions derived from dilepton data.

For the bounds coming from the LHC, we can see that dilepton bounds are considerably dominant with respect to those coming from mono-jets. The reason behind this is that the first channel has a low and well-understood background, while jets tend to present a complicated scenario with high signal-to-noise ratio. In fact, dilepton searches represent the most stringent limits in this particular framework, showing that mediator searches in simplified models are a powerful tool. This limit gets weakened for WIMP masses below the resonance for the reasons discussed in section 2.2.2.4 and it depends on the coupling constant  $g_\chi$ . For  $g_\chi = 0.1$  (fig. 2.5) the effect is negligible, while for the extreme case of  $g_\chi = 4\pi$  (fig. 2.7) the exclusion bound goes down to  $M_{Z'} \sim 1$  TeV. At this point others limits coming from colliders should be taken into account, like the dielectron production cross section at LEP [21], ruling out  $Z'$  masses around 1.8 TeV for this particular case. At any rate, direct detection experiments are the most competitive in this regime, with the projected limits of XENONIT able to

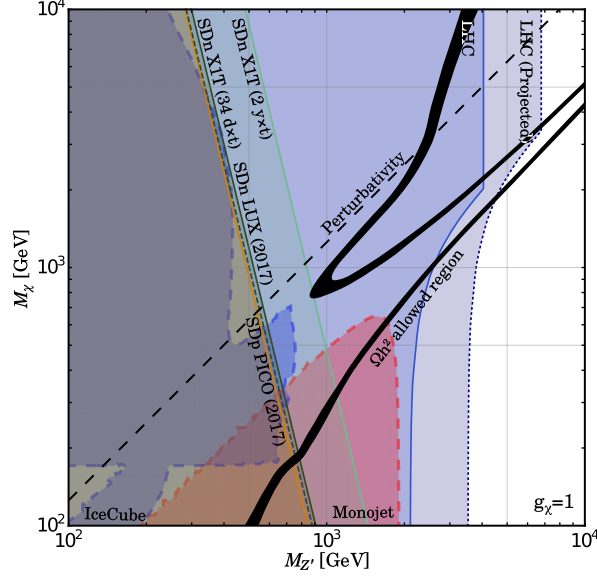


Figure 2.6: Exclusion limits for  $g_\chi = 1$ . The black solid curve outlines the region of parameter space with the correct relic density. From left to right: in blue dashed the parameter space excluded by IceCube; the orange solid line represents the current bound from PICO; the green dashed line the current bound from LUX on SD scattering off neutrons with 129.5 kg-year exposure; the solid green line the projected bound from XENONIT on SD scattering off neutrons with 34  $d \times t$  of exposure; further right in light green, we show the projected sensitivity from XENONIT on SD scattering off neutrons with  $2 y \times t$  exposure; the region above the black dashed line delimits the non-perturbative regime; the red dashed curve depicts the parameter space excluded by LHC based on mono-jet data; blue vertical solid (dotted) lines delimit the current (projected) LHC exclusion regions derived from dilepton data.

exclude  $M_{Z'} \lesssim 3.5$  TeV.

To conclude this section, we will discuss the possible consequences of considering a UV-complete model in which the discussed setup might be embedded. As mentioned before, the simplest route is to enlarge  $G_{\text{SM}}$  with an additional  $U(1)'$  gauge group. The first immediate consequence of this is, in order to get a theoretically consistent model, we need to make sure that no anomalies arise. By construction, the charges of SM fermions do not introduce any anomalies, being the same as the SM hypercharge. On the other hand the introduction of  $\chi$ , charged under  $U(1)'$ , would introduce anomalies for which at least one additional state is required [22]. The consequences of this extra degree of freedom are model dependant, and we assume here that is considerably heavier than the other states.

Another relevant consequence arises when the mass generation mechanism for  $\chi$  and  $Z'$  is considered, the simplest option being, as already mentioned, a SSB

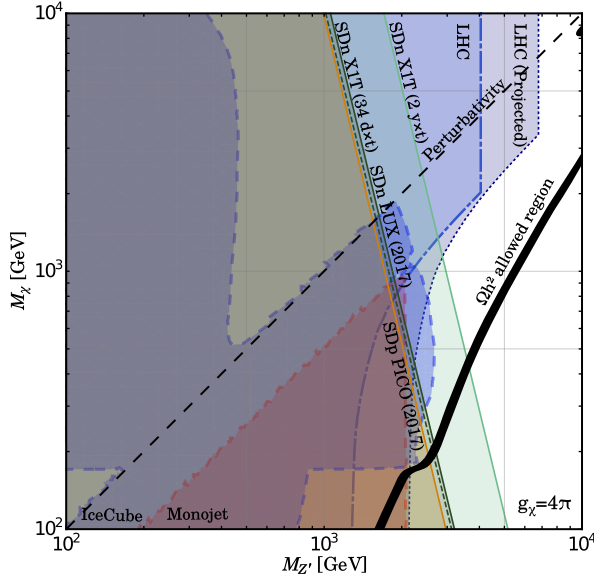


Figure 2.7: Exclusion limits for  $g_\chi = 4\pi$ . The black solid curve outlines the region of parameter space with the correct relic density. From left to right: in blue dashed the parameter space excluded by IceCube; the orange solid line represents the current bound from PICO; the green dashed line the current bound from LUX on SD scattering off neutrons with 129.5 kg-year exposure; the green solid line the projected bound from XENON1T on SD scattering off neutrons with  $34 d \times t$  of exposure; further right in light green, we show the projected sensitivity from XENON1T on SD scattering off neutrons with  $2 y \times t$  exposure; the region above the black dashed line delimits the non-perturbative regime; the red dashed curve depicts the parameter space excluded by LHC based on mono-jet data; blue vertical dot-dashed (dotted) lines delimit the current (projected) LHC exclusion regions derived from dilepton data.

of  $U(1)'$  through the vev of a scalar singlet  $S$ . If this would be the case, the scalar field can have a strong impact on dark matter phenomenology if its mass is comparable to  $M_\chi$ . It could for example, become an additional portal to the SM, modify the relic density by becoming an final state of dark matter annihilation or induce SI interactions of  $\chi$  with nucleons radiatively [18]. We need to assume again that this state is decoupled from the relevant phenomenology. On top of that, it is also necessary to assume that the coupling  $\lambda_{HS}$  of an unavoidable Higgs portal  $\lambda_{HS}|H|^2S^2$  is also negligible.

Finally, we have assumed throughout this analysis that no mass mixing exists between the gauge bosons  $Z$  and  $Z'$ . If the Higgs boson is not charged under  $U(1)'$  a mass mixing would be forbidden at tree level. However at loop level it can still be generated by SM fermion loops [23] or by a higher order operator like  $Z'_\mu H^\dagger D^\mu H$ . This mixing would impact the relic abundance by introducing new annihilation channels like  $WW$ ,  $ZZ$ ,  $ZZ'$  and  $Zh$  final states. A quantita-

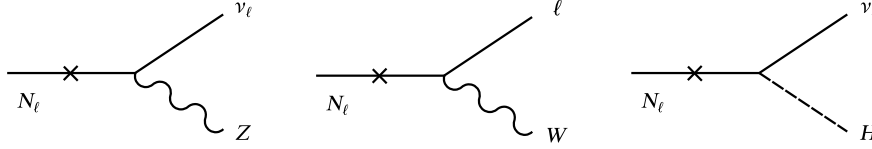


Figure 2.8: Feynman diagrams for two-body decays of the right-handed neutrinos.

tive evaluation is again model dependent, but at any rate the extent of a  $Z - Z'$  mixing is highly constrained by electroweak precision tests (EWPT) [24, 25]. For simplicity's sake, we neglect said mixing in this work.

## 2.3 The Neutrino Portal

We have seen in the previous section that, when it comes to simplified models, the mediator searches can be as constraining as the dark matter searches themselves. Here we consider an entirely different kind of portal and focus on its properties and phenomenological consequences rather than on the details of the dark matter candidate.

In this section we assume that dark matter is a WIMP which interacts exclusively with heavy right-handed neutrinos, making the latter the only possible connection with the visible sector. By doing this, we abandon the common assumption of indirect detection searches discussed in section 1.3.4.1, namely that the product of dark matter annihilations are SM particles.

As commented in section 1.4.3, right-handed neutrinos offer a rich phenomenology and are integral parts of a wide variety of BSM models. Due to this, a direct connection to the dark matter puzzle can naturally arise in a UV-complete theory, which we explore here under the conjecture that the additional leptons constitute the main dark matter annihilation mode. We dedicate this section then to analyse Fermi-LAT [26, 27] and H.E.S.S. [28] gamma ray data in order to constrain said assumption. Our results will consist on limits on the velocity-averaged cross section  $\langle\sigma v\rangle$  (see for example **★ Indirect Detection** in section 1.3.4.1) as a function of the right-handed neutrino and dark matter masses.

### 2.3.1 The Method

In order to make a connection to the visible sector, we assume here that the heavy right-handed neutrinos,  $N_\ell$ , mix with the active neutrinos. Such, usually small, mixing angles can be obtained through the seesaw type-I mechanism discussed in section 1.4.3 and, when kinematically allowed, generate the following two-body decay widths [29, 30]

$$\begin{aligned}
\Gamma(N_\ell \rightarrow Z\nu_\ell) &= \frac{\alpha_W}{16M_W^2} |C_{\nu_\ell N}|^2 M_N^3 \left(1 + \frac{2M_Z^2}{M_N^2}\right) \left(1 - \frac{M_Z^2}{M_N^2}\right)^2 \theta(M_N - M_Z), \\
\Gamma(N_\ell \rightarrow W\ell) &= \frac{\alpha_W}{16M_W^2} |B_{\ell N}|^2 M_N^3 \left(1 + \frac{2M_W^2}{M_N^2}\right) \left(1 - \frac{M_W^2}{M_N^2}\right)^2 \theta(M_N - M_W), \\
\Gamma(N_\ell \rightarrow H\nu_\ell) &= \frac{\alpha_W}{16M_W^2} |C_{\nu_\ell N}|^2 M_N^3 \left(1 - \frac{M_H^2}{M_N^2}\right)^2 \theta(M_N - M_H),
\end{aligned} \tag{2.12}$$

where  $\alpha_W = g^2/4\pi$  and  $B_{\ell N}(C_{\nu_\ell N})$  represent the mixing matrices entering the charged (neutral) currents. There is an overall 1/2 factor, as we assume that the heavy state is a Majorana fermion. We show these processes in fig. 2.8.

When  $M_N < M_W$ , none of the channels in eq. (2.12) is available, and we have to rely instead on the three body decays of the type shown in the left panel of fig. 1.11. We can separate these contributions into neutral-current (NC) decays [31, 32]

$$\begin{aligned}
\Gamma(N_\ell \rightarrow \nu_\ell \nu_{\ell'} \bar{\nu}_{\ell'}) &= \frac{\alpha_W^2}{192\pi M_W^4} |C_{\nu_\ell N}|^2 M_N^5, \\
\Gamma(N_\ell \rightarrow \nu_\ell \ell' \ell') &= \frac{\alpha_W^2}{192\pi M_W^4} |C_{\nu_\ell N}|^2 M_N^5 \left(\frac{1}{4} + \sin^2 \theta_W + 2 \sin^4 \theta_W\right), \\
\Gamma(N_\ell \rightarrow \nu_\ell u_i \bar{u}_i) &= \frac{\alpha_W^2}{192\pi M_W^4} |C_{\nu_\ell N}|^2 M_N^5 \left(\frac{1}{4} - \frac{1}{3} \sin^2 \theta_W + \frac{2}{9} \sin^4 \theta_W\right), \\
\Gamma(N_\ell \rightarrow \nu_\ell d_j \bar{d}_j) &= \frac{\alpha_W^2}{192\pi M_W^4} |C_{\nu_\ell N}|^2 M_N^5 \left(\frac{1}{4} - \frac{2}{3} \sin^2 \theta_W + \frac{8}{9} \sin^4 \theta_W\right),
\end{aligned} \tag{2.13}$$

and charged-current (CC) decays

$$\begin{aligned}
\Gamma(N_\ell \rightarrow \ell \nu_{\ell'} \ell') &= \frac{\alpha_W^2}{192\pi M_W^4} |B_{\ell N}|^2 M_N^5, \\
\Gamma(N_\ell \rightarrow \ell u_i \bar{d}_i) &= 3 \left(1 + \frac{\alpha_s}{\pi}\right) \frac{\alpha_W^2}{192\pi M_W^4} |B_{\ell N}|^2 M_N^5,
\end{aligned} \tag{2.14}$$

where  $g_s = \sqrt{4\pi\alpha_s}$  is the strong coupling constant,  $u_i = (u, c)$ ,  $d_j = (d, s, b)$  in eq. (2.13) and  $d_i = (d, s)$  in eq. (2.14) because of kinematics. Notice that the conjugated case of some of these processes also need to be taken into account. We have furthermore included for completeness the radiative decay shown in the right panel of fig. 1.11. Its decay width, given in eq. (1.36), can be rewritten here as

$$\Gamma(N_\ell \rightarrow \gamma \nu_\ell) = \frac{9\alpha_{em}\alpha_W^2}{512\pi^2 M_W^4} |C_{\nu_\ell N}|^2 M_N^5. \tag{2.15}$$

In this analysis we are going to assume the so-called ‘‘one-flavour approximation’’ (a term borrowed from the Leptogenesis community), where the right-handed neutrino mixes with just one lepton flavour at a time, implying that



$B_{\ell N} = C_{\nu_\ell N}$ . As we have discussed in section 1.3.4.1, the gamma-ray flux in which we are interested can be written as

$$\frac{d\Phi_\gamma}{dE}(E_\gamma) = \frac{1}{4\pi} \frac{\langle \sigma_{ann} v \rangle}{2M_\chi^2} \frac{dN_\gamma}{dE_\gamma} \cdot J_{ann}, \quad (2.16)$$

and the relevant quantity from the particle physics side is the energy spectrum, which depends on the branching ratio of the different hypothetical decay channels. This implies that, in the approximation this work is based on, no dependence appears on the mixing angle between the sterile and active neutrinos. The appearance of this mixing angle is a common feature arising in laboratory searches that—due to its small values—greatly hinders these experimental efforts, as we will see in chapter 3. In any event, the one-flavour approximation is largely justified, as the energy spectra obtained depend very weakly on the final lepton flavour, as we will see.

In order to obtain the corresponding  $dN_\gamma/dE_\gamma$  for this particular framework, we used the MonteCarlo simulation program `Pythia 8.219` [33] and modelled dark matter annihilation as a resonance  $\mathcal{D}$  that decays exclusively to right-handed neutrinos, with  $M_{\mathcal{D}} = 2M_\chi$ , following [34, 35]. We integrated eqs. (2.12) to (2.15) with their respective kinematic limits in order to explore the  $M_N = [10, 10^3]$  GeV mass range (see appendix A.1 for further details), to obtain the characteristic continuous spectrum of indirect detection searches shown in fig. 2.9. In these figures we plot the spectra  $x dN_\gamma/dx$  as a function of the energy fraction  $x = E_\gamma/M_\chi$  for  $M_\chi = 100$  GeV ( $M_\chi = 1$  TeV) in the upper (lower) panel. The purple and green curves represent two benchmark annihilation channels used in literature:  $\chi\chi \rightarrow b\bar{b}$  and  $\chi\chi \rightarrow W^+W^-$  obtained through the *PPPC for Dark Matter Identification* code described in [34] (and re-obtained using our own code to check for robustness). These curves can be compared to our results in orange and yellow for  $M_N = 90$  GeV and  $M_N = 10$  GeV ( $M_N = 500$  GeV and  $M_N = 50$  GeV) in the upper (lower) panel respectively. We can see that the right-handed neutrino annihilation channel yields a similar spectrum at high energies, while at low energies it displays a harder spectrum than the usual channels, when the gauge bosons are produced off-shell (upper panel). In both of these plots we assume the final leptons to belong to the first family ( $\ell = e$ ). In fig. 2.10 we compare the spectra for the three leptonic families for  $M_\chi = 1$  TeV and  $M_N = 500$  GeV. The similarities among them justify the adopted one-flavour approximation and reveal that the only significant difference among them corresponds to the slightly harder spectrum in the  $\ell = \tau$  case, for higher energies.

The astrophysics side of eq. (2.16) is represented by the  $J$ -factor, which integrates the intervening matter along the line of sight, as discussed in section 1.3.4.1, and is characteristic for each source studied. Due to this, in order to not be sensitive to the particularities of each source, we will adopt a joint-likelihood analysis,

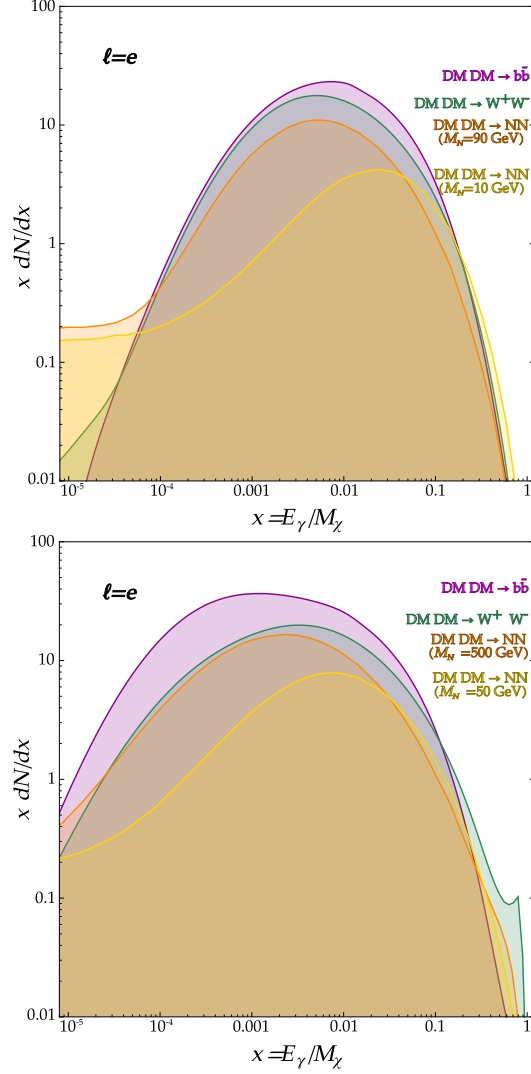


Figure 2.9: Gamma spectra for the annihilation of a dark matter particle with mass  $M_\chi = 100 \text{ GeV}$  (upper-panel) and  $M_\chi = 1000 \text{ GeV}$  (lower panel) into different final states. For simplicity we show just the case in which  $N$  mixes exclusively with  $\ell = e$ . Magenta and green curves represent the final states of  $b\bar{b}$  and  $W^+W^-$ . Upper panel: Orange and yellow curves account for annihilations into right-handed neutrinos with  $M_N = 90 \text{ GeV}$  and  $M_N = 10 \text{ GeV}$  respectively. Lower Panel: Orange and yellow curves account for annihilations into right-handed neutrinos with  $M_N = 500 \text{ GeV}$  and  $M_N = 50 \text{ GeV}$  respectively.

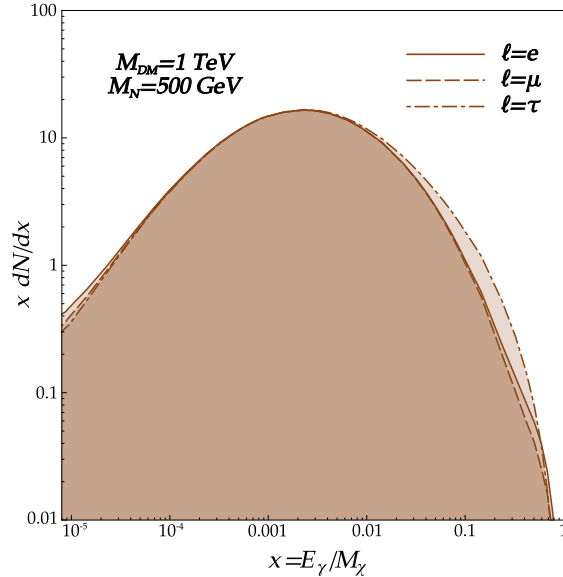


Figure 2.10: The energy spectrum for  $M_{DM} = 1 \text{ TeV}$  and  $M_N = 500 \text{ GeV}$ , for different final state leptons. One can see there is only a mild difference between them, with the final state  $\tau$  leading to a harder gamma-ray yield, i.e. larger  $dN/dE$ , as expected since they lead to a relatively more efficient hadronization process.

as detailed in the next section. As for the sources, we will pick regions of our galactic neighbourhood believed to contain a high concentration of dark matter: dSphs and the GC. Dwarf spheroidals consist of low-luminosity galaxies orbiting larger galaxies like the MW or Andromeda. With typical masses around  $10^7 M_\odot$ , most of it in the form of dark matter [36], their  $M/L$  tend to be very high due to their low surface brightness, some having values higher than the MW [37]. Due to this, they have very low backgrounds that the Fermi Large Area Telescope (Fermi-LAT) exploits in search for dark matter signals. It has registered, for 6 six years between 2008 and 2014, the gamma-spectrum of dozens of these objects that due to their high latitude show low diffuse gamma-ray emissions [26, 27]. On the hand, we have the galactic center, where most of the dark matter in our galaxy lies [38, 39], but which is subject to strong backgrounds. This is true especially at the very center, where a high flux gamma-ray source is measured coincident with the position of the supermassive black hole Sgr A\* [40]. Accordingly, the High Energy Stereoscopic System (H.E.S.S.) has performed an analysis based on 112h of live time (taken between 2004 and 2008) of a circle around the GC (with  $1^\circ$  radius), excluding the Galactic plane (a band of  $0.6^\circ$  width) [28]. We will provide details about these datasets and their analyses in the following section.

## 2.3.2 The Constraints

We detail in this subsection the properties of each dataset and the assumptions made by both collaborations, which are relevant for our study. We also describe the joint-likelihood analysis that performed in order to obtain sensible constraints.

### 2.3.2.1 Fermi-LAT Dataset

The Fermi Gamma-ray Space Telescope was launched in 2008 to perform gamma-ray observations from low Earth orbit using the LAT. Since then it has been registering events continuously. We will use for this work the `PASS 8` event-level analysis of 25 dSphs reported in [27], which collects data taken between 2008 and 2014, enhancing the previous analysis [26] in several aspects including—but not restricted to—improved effective area and energy reach, and more accurate Monte Carlo simulations of the detector and the environment. The events will be restricted to those in the 500 MeV and 500 GeV energy range coming from a squared region of interest (ROI) of  $10^\circ \times 10^\circ$  around the studied dSphs. From the total 25 dSphs, just 15 were analysed using the criteria of no overlapping ROIs and kinematically determined  $J$ -factors. The list of dSphs observed by Fermi-LAT, their distance from Earth and their respective  $J$ -factors are given in table 2.1, where the upper block contains those used for this study. The  $J$ -factors are calculated using eq. (1.34), assuming an NFW density profile and integrating over a solid angle of  $\Delta\Omega \sim 2.4 \times 10^{-4}$  sr. The location on the sky of these astronomical objects can be seen in the white circles shown in fig. 2.11.

The Fermi Collaboration has modelled the expected diffuse background using a structured Galactic component and a spatially isotropic component that represents both extragalactic emission and residual particle contamination.<sup>3</sup> From the energy binned Poisson maximum-likelihood analysis performed with the Fermi Science Tools made available by the collaboration<sup>4</sup>, it is possible to reproduce the constraints obtained for each dSph. However, in order to avoid spurious effects coming from the characteristics of a given dSph, we carry out a joint-likelihood analysis, following the Supplemental Material in [27] and implemented using the `GAMBIT` module `gamLike` (see appendix A.2 for a brief description of these packages).

If we treat the  $J$ -factors as nuisance parameters, it is possible to define the

<sup>3</sup><http://fermi.gsfc.nasa.gov/ssc/data/access/lat/BackgroundModels.html>

<sup>4</sup>[http://www-glast.stanford.edu/pub\\_data/1048/](http://www-glast.stanford.edu/pub_data/1048/)

<i>name</i>	<i>abbreviation</i>	<i>distance</i> [kpc]	$\log_{10}(J_{obs})$ [ $\log_{10}[\text{GeV}^2 \text{ cm}^{-5}]$ ]
Bootes I	Boo I	66	$18.8 \pm 0.22$
Canes Venatici II	CVn II	160	$17.9 \pm 0.25$
Carina	Car	105	$18.1 \pm 0.23$
Coma Berenices	Com	44	$19.0 \pm 0.25$
Draco	Dra	76	$18.8 \pm 0.16$
Fornax	For	147	$18.2 \pm 0.21$
Hercules	Her	132	$18.1 \pm 0.25$
Leo II	Leo II	233	$17.6 \pm 0.18$
Leo IV	Leo IV	154	$17.9 \pm 0.28$
Sculptor	Scl	86	$18.6 \pm 0.18$
Segue 1	Seg 1	23	$19.5 \pm 0.29$
Sextans	Sex	86	$18.4 \pm 0.27$
Ursa Major II	UMa II	32	$19.3 \pm 0.28$
Ursa Minor	UMi	76	$18.8 \pm 0.19$
Willman 1	Wil 1	38	$19.1 \pm 0.31$
Bootes II	Boo II	42	×
Bootes III	Boo III	47	×
Canes Venatici I	CVn I	218	$17.7 \pm 0.26$
Canis Major	CMA	7	×
Leo I	Leo I	254	$17.7 \pm 0.18$
Leo V	Leo V	178	×
Pisces II	Psc II	182	×
Sagittarius	Sgr	26	×
Segue 2	Seg 2	35	×
Ursa Major I	UMa I	97	$18.3 \pm 0.24$

*Table 2.1: Milky Way dSphs observed by Fermi-LAT, their distance from Earth and associated J-factors. The upper block comprises those used for the analysis performed in this section.*

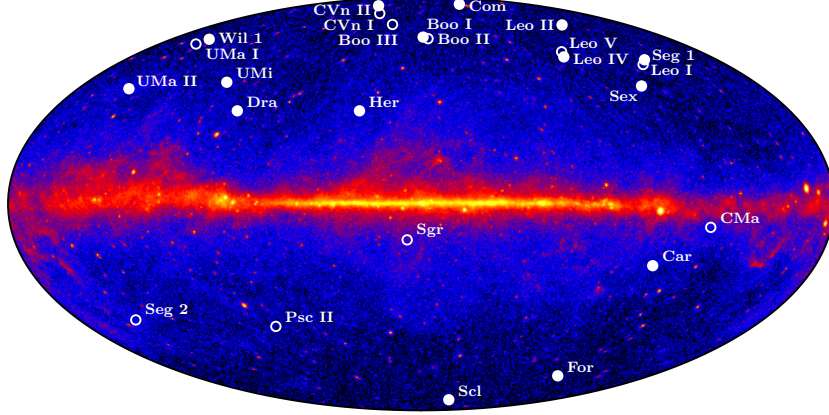


Figure 2.11: Location of the dSphs listed in table 2.1 overlaid on a 4-year LAT counts map (for  $E > 1$  GeV). Those used in this analysis are shown as filled circles, while those not considered are shown as open circles. Figure taken from [26].

respective likelihood function as

$$\mathcal{L}_J(J_i|J_{obs,i}, \sigma_i) = \frac{1}{\ln(10)J_{obs,i}\sqrt{2\pi}\sigma_i} \times \exp\left\{-\frac{(\log_{10}(J_i) - \log_{10}(J_{obs,i}))^2}{2\sigma_i^2}\right\},$$

where  $J_{obs,i}$  is the measured  $J$ -factor with error  $\sigma_i$  of a dSph  $i$  and  $J_i$  is its true  $J$ -factor value. Now, if  $\mu$  are the parameters of the dark matter model (like the dark matter mass or the annihilation cross section) and  $\theta_i$  comprises the set of nuisance parameters from the LAT analysis ( $\alpha_i$ ) and the  $J$ -factor of the dSph  $i$ , we can redefine the likelihood function as

$$\tilde{\mathcal{L}}_i(\mu, \theta_i = \{\alpha_i, J_i\}|D_i) = \mathcal{L}_i(\mu, \theta_i|D_i)\mathcal{L}_J(J_i|J_{obs,i}, \sigma_i), \quad (2.17)$$

where  $D_i$  is the gamma-ray data. In order to decrease uncertainty on the direction measurement, it can be subdivided into four different types of point-spread function (PSF) event types ( $D_{i,j}$ ). The joint-likelihood corresponds then to the total product given by

$$\mathcal{L}_i(\mu, \theta_i|D_i) = \prod_j \mathcal{L}_i(\mu, \theta_i|D_{i,j}). \quad (2.18)$$

In order to obtain 95% C.L. upper limits on the annihilation cross section, we perform a test statistic (TS) defined as [41]

$$\text{TS} = -2 \ln \left( \frac{\mathcal{L}(\mu_0, \hat{\theta}|D)}{\mathcal{L}(\hat{\mu}, \hat{\theta}|D)} \right) \quad (2.19)$$

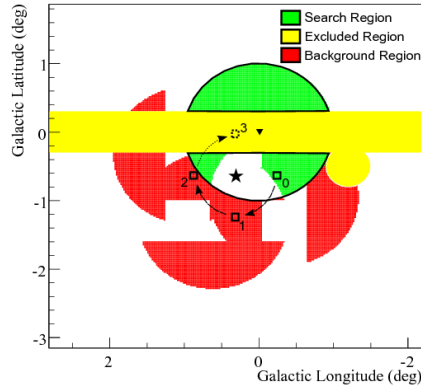


Figure 2.12: Definition of the ROI (green) around the GC (black triangle), excluded area (yellow) and area used for background control (red). In particular the process for background subtraction for a particular telescope pointing position (star) is illustrated: the background control for pixel 0 is obtained from pixels 1 and 2, while pixel 3 is excluded. Each pixel has a size of  $0.02^\circ \times 0.02^\circ$ . Figure taken from [28].

where  $\mu_0$  are the parameters of the null hypothesis (i.e. no dark matter) and  $\hat{\mu}$  and  $\hat{\theta}$  are the best-fit parameters under the dark matter hypothesis. The limits on  $\langle\sigma v\rangle$  can be obtained by imposing TS bigger than 2.71. This procedure can reproduce the Fermi results, as shown in [42] and was used to obtain the blue curves in figs. 2.14 to 2.16.

### 2.3.2.2 H.E.S.S. Dataset

H.E.S.S. is an array of five Imaging Atmospheric Cherenkov Telescopes, located in the Khomas highlands of Namibia, four of them with a dish of 12 m diameter (H.E.S.S. phase I, operating since 2003) and a larger one of 28 m diameter (H.E.S.S. phase II, operating since 2012). They possess a gamma-ray sensitivity between 0.03 and 100 TeV.

For this analysis the ROI is defined as a circular area around the GC with a radius of  $R_{on} = 1^\circ$ . Due to local astrophysical contamination sources however, the analysis is restricted to galactic latitudes such that  $|b| > 0.3^\circ$ , excluding the galactic plane as depicted in fig. 2.12.

The flux of events passing the standard cuts defined in [43] for the source and the background regions are shown in fig. 2.13. In order to re-obtain the number of events we can simply multiply the data from this figure by the exposure time (112h in this case), the effective area provided by the python code `Gammapy`<sup>5</sup>

<sup>5</sup><https://gammapy.readthedocs.io/en/latest/>

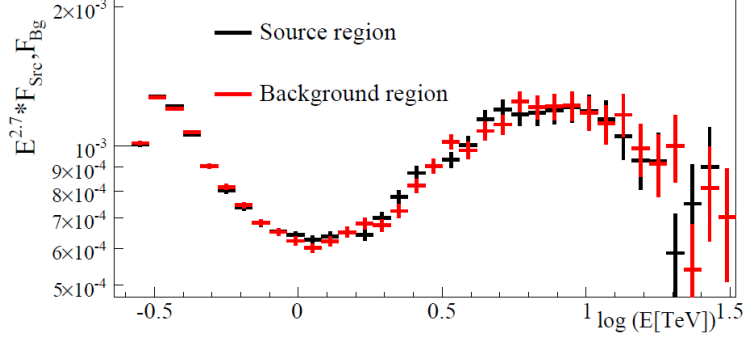


Figure 2.13: Reconstructed differential flux  $F_{Src/Bg}$ , weighted with  $E^{2.7}$  for better visibility, obtained for the source and background regions as defined in the fig. 2.12. Figure taken from [28].

and the  $J$ -factors obtained in [28] (equal to  $\bar{J}_{src} = 1604 \times \rho_E^2 \times d_E$  and  $\bar{J}_{bg} = 697 \times \rho_E^2 \times d_E$  for source and background regions respectively, using an NFW profile). Following [44] we can define the total likelihood function, for spatial bins  $i$  and the energy bins  $j$  as

$$\mathcal{L}(M_\chi, \langle \sigma v \rangle) = \prod_{i,j} \mathcal{L}_{i,j}^{src}(M_\chi, \langle \sigma v \rangle) \times \prod_i \mathcal{L}_i^{bg}(M_\chi, \langle \sigma v \rangle), \quad (2.20)$$

where the individual likelihoods for source and background can be found in [45]. From here, we can perform again a TS. In this case the analogous of eq. (2.19) is

$$\text{TS} = -2 \ln \left( \frac{\mathcal{L}(M_\chi, \langle \sigma v \rangle)}{\mathcal{L}_{max}(M_\chi, \langle \sigma v \rangle)} \right) \quad (2.21)$$

which follows an approximate  $\chi^2$  distribution with one degree of freedom. This procedure can be validated by comparing the results obtained by the H.E.S.S. collaboration, as it was done in [42] for different final state annihilations. The collaboration has recently released a new dataset analysing 254h of exposure of the GC which led to an improvement of the previous analysis by a factor of 5 for masses over 400 GeV [46]. Considering that for masses below this value the most constraining limits come from the Fermi-LAT dataset, we will use the [28] dataset, but rescaled properly to match the current results published in [46]. The final results for dark matter annihilation into right-handed neutrinos using this procedure can be seen as the red curves in figs. 2.14 to 2.16.



### 2.3.3 The Results

In figs. 2.14 to 2.16 we present our limits on  $\langle\sigma v\rangle$  for dark matter annihilating into heavy sterile neutrino states, as a function of the dark matter mass  $M_\chi$  for three different cases of right-handed neutrino masses:  $M_N = 10, 10^2, 10^3$  GeV in straight, dashed and dot-dashed lines respectively. As discussed in the previous section, we have used the Fermi-LAT (in blue) and the H.E.S.S. dataset (in red) in order to obtain these bounds. The horizontal black dotted line depicts the canonical thermal cross section ( $3 \times 10^{-26} \text{ cm}^3 \text{ s}^{-1}$ ) that reproduces the right relic abundance for a WIMP. It is worth to mention however that, as it was pointed out in [47], a more precise calculation yields  $5 \times 10^{-26} \text{ cm}^3 \text{ s}^{-1}$  at masses  $< 10$  GeV and  $2 \times 10^{-26} \text{ cm}^3 \text{ s}^{-1}$  at higher masses, so this line should not be taken at face value. The results are presented for the three possible leptonic final states. No significant difference can be found between fig. 2.14 and fig. 2.15; a natural consequence of the similar behaviour between decays to  $\ell = e$  and  $\ell = \mu$  exhibited by  $xdN/dx$  in fig. 2.10. By inspecting the same figure, it is also natural that the case  $\ell = \tau$  yields stronger bounds for higher values of  $M_\chi$  and  $M_N$ .

Independently of the leptonic flavour or the right-handed neutrino mass, the limits imposed by the Fermi-LAT dataset are stronger for dark matter masses below 500 GeV, while those stemming from the H.E.S.S. dataset are always stronger for masses above 1 TeV. In the intermediate mass range, it depends on the value of  $M_N$ . This complementarity can be understood in terms of the telescopes' energy thresholds: Fermi-LAT uses for its analysis photons in the energy range 500 MeV to 500 GeV, which means that a good part of the photons radiated by the dark matter annihilation of particles in the TeV scale would be lost to this detector, limiting its sensitivity. The opposite effect occurs for H.E.S.S. as we have used here their measured photon flux for energies higher than 400 GeV.

In conclusion we have analysed a method to probe dark matter annihilations to heavy right-handed neutrinos, imposing constraints on the thermally averaged cross section as a function of the masses of the particles involved using the Fermi-LAT measurements of dSphs and H.E.S.S. measurements of the GC, ruling out the thermal annihilation cross section for dark matter masses below 200 GeV. In the adopted one-flavour approximation, we have been able to impose these constraints independently of the mixing angles between the sterile and the active neutrino states, introducing an orthogonal way to constrain these states, under the assumptions here presented. As we will see in chapter 3 these mixing angles are usually a limiting factor when studying sterile neutrinos.

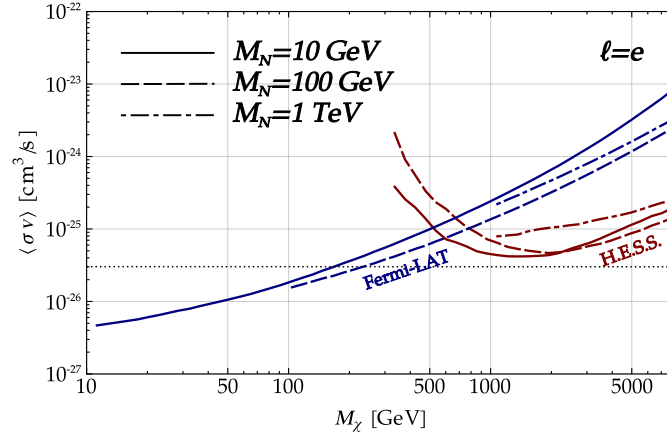


Figure 2.14: Upper limit on  $\langle\sigma v\rangle$  as a function of the dark matter mass ( $M_\chi$ ) for the electron right-handed neutrino final state. Blue curves represent the limits obtained using Fermi-LAT data, while red are those obtained using H.E.S.S. data. Solid, dashed and dot-dashed curves are for  $M_N = 10, 10^2, 10^3$  GeV respectively. The horizontal dotted line shows the thermal cross section  $\sim 3 \times 10^{-26} \text{ cm}^3 \text{ s}^{-1}$ .

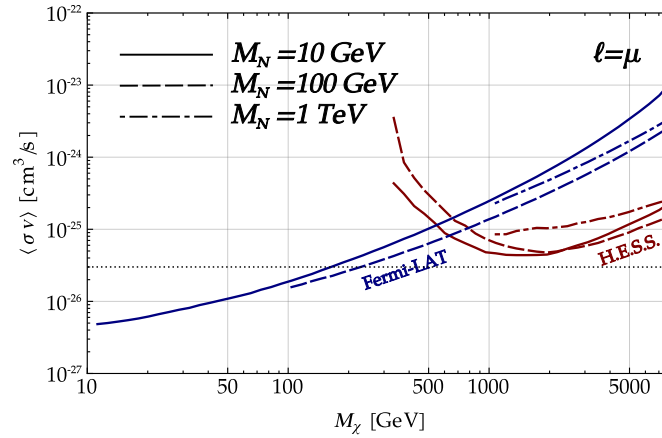


Figure 2.15: Upper limit on  $\langle\sigma v\rangle$  as a function of the dark matter mass ( $M_\chi$ ) for the muon right-handed neutrino final state. Blue curves represent the limits obtained using Fermi-LAT data, while red are those obtained using H.E.S.S. data. Solid, dashed and dot-dashed curves are for  $M_N = 10, 10^2, 10^3$  GeV respectively. The horizontal dotted line shows the thermal cross section  $\sim 3 \times 10^{-26} \text{ cm}^3 \text{ s}^{-1}$ .

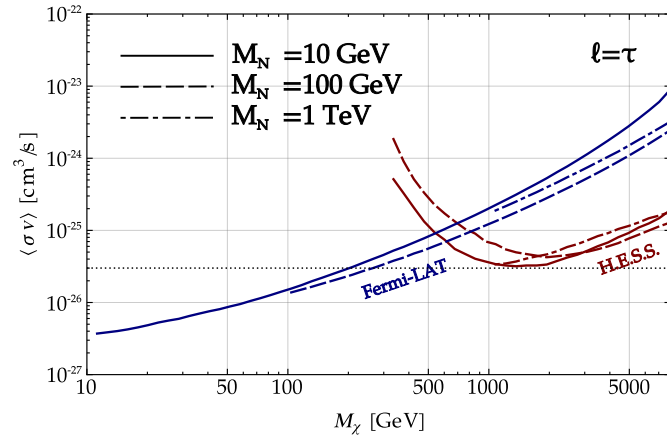


Figure 2.16: Upper limit on  $\langle \sigma v \rangle$  as a function of the dark matter mass ( $M_\chi$ ) for tau right-handed neutrino final state. Blue curves represent the limits obtained using Fermi-LAT data, while red are those obtained using H.E.S.S. data. Solid, dashed and dot-dashed curves are for  $M_N = 10, 10^2, 10^3$  GeV respectively. The horizontal dotted line shows the thermal cross section  $\sim 3 \times 10^{-26}$  cm<sup>3</sup> s<sup>-1</sup>.

## References

- [1] J. Goodman, M. Ibe, A. Rajaraman, W. Shepherd, T.M.P. Tait and H.B. Yu, *Constraints on Light Majorana dark Matter from Colliders*, *Phys. Lett.* **B695** (2011) 185 [[arXiv:1005.1286](#)].
- [2] M. Garny, A. Ibarra, S. Rydbeck and S. Vogl, *Majorana Dark Matter with a Coloured Mediator: Collider vs Direct and Indirect Searches*, *JHEP* **06** (2014) 169 [[arXiv:1403.4634](#)].
- [3] T. Nomura, H. Okada and Y. Orikasa, *Radiative Seesaw Model with Degenerate Majorana Dark Matter*, *Phys. Rev.* **D93** (2016) 113008 [[arXiv:1603.0463](#)].
- [4] G. Belanger, F. Boudjema, A. Pukhov and A. Semenov, *micrOMEGAs 3: A program for calculating dark matter observables*, *Comput. Phys. Commun.* **185** (2014) 960 [[arXiv:1305.0237](#)].
- [5] D. Barducci, G. Belanger, J. Bernon, F. Boudjema, J. Da Silva, S. Kraml, U. Laa and A. Pukhov, *Collider limits on new physics within micrOMEGAs 4.3*, *Comput. Phys. Commun.* **222** (2018) 327 [[arXiv:1606.0383](#)].
- [6] G. Arcadi, Y. Mambrini and F. Richard, *Z-portal dark matter*, *JCAP* **1503** (2015) 018 [[arXiv:1411.2985](#)].
- [7] K. Griest and D. Seckel, *Three exceptions in the calculation of relic abundances*, *Phys. Rev.* **D43** (1991) 3191.
- [8] H. An, X. Ji and L.T. Wang, *Light Dark Matter and Z' Dark Force at Colliders*, *JHEP* **07** (2012) 182 [[arXiv:1202.2894](#)].
- [9] H.Y. Cheng and C.W. Chiang, *Revisiting Scalar and Pseudoscalar Couplings with Nucleons*, *JHEP* **07** (2012) 009 [[arXiv:1202.1292](#)].
- [10] **PICO** Collaboration, C. Amole et al., *Dark Matter Search Results from the PICO-60 C<sub>3</sub>F<sub>8</sub> Bubble Chamber*, *Phys. Rev. Lett.* **118** (2017) 251301 [[arXiv:1702.0766](#)].
- [11] **LUX** Collaboration, D.S. Akerib et al., *Limits on spin-dependent WIMP-nucleon cross section obtained from the complete LUX exposure*, *Phys. Rev. Lett.* **118** (2017) 251302 [[arXiv:1705.0338](#)].
- [12] **XENON100** Collaboration, E. Aprile et al., *Limits on spin-dependent WIMP-nucleon cross sections from 225 live days of XENON100 data*, *Phys. Rev. Lett.* **111** (2013) 021301 [[arXiv:1301.6620](#)].

- [13] **XENON** Collaboration, E. Aprile et al., *Physics reach of the XENON1T dark matter experiment*, *JCAP* **1604** (2016) 027 [[arXiv:1512.0750](#)].
- [14] **XENON** Collaboration, E. Aprile et al., *First Dark Matter Search Results from the XENON1T Experiment*, *Phys. Rev. Lett.* **119** (2017) 181301 [[arXiv:1705.0665](#)].
- [15] A. Ibarra, M. Totzauer and S. Wild, *Higher order dark matter annihilations in the Sun and implications for IceCube*, *JCAP* **1404** (2014) 012 [[arXiv:1402.4375](#)].
- [16] **ATLAS** Collaboration, M. Aaboud et al., *Search for new high-mass phenomena in the dilepton final state using 36 fb<sup>1</sup> of proton-proton collision data at  $\sqrt{s} = 13$  TeV with the ATLAS detector*, *JHEP* **10** (2017) 182 [[arXiv:1707.0242](#)].
- [17] G. Arcadi, Y. Mambrini, M.H.G. Tytgat and B. Zaldivar, *Invisible Z' and dark matter: LHC vs LUX constraints*, *JHEP* **03** (2014) 134 [[arXiv:1401.0221](#)].
- [18] F. Kahlhoefer, K. Schmidt-Hoberg, T. Schwetz and S. Vogl, *Implications of unitarity and gauge invariance for simplified dark matter models*, *JHEP* **02** (2016) 016 [[arXiv:1510.0211](#)].
- [19] J. Shu, *Unitarity Bounds for New Physics from Axial Coupling at LHC*, *Phys. Rev.* **D78** (2008) 096004 [[arXiv:0711.2516](#)].
- [20] M. Duerr, F. Kahlhoefer, K. Schmidt-Hoberg, T. Schwetz and S. Vogl, *How to save the WIMP: global analysis of a dark matter model with two s-channel mediators*, *JHEP* **09** (2016) 042 [[arXiv:1606.0760](#)].
- [21] P. Langacker, *The Physics of Heavy Z' Gauge Bosons*, *Rev. Mod. Phys.* **81** (2009) 1199 [[arXiv:0801.1345](#)].
- [22] J. Ellis, M. Fairbairn and P. Tunney, *Anomaly-Free Dark Matter Models are not so Simple*, *JHEP* **08** (2017) 053 [[arXiv:1704.0385](#)].
- [23] B. Holdom, *Two U(1)'s and Epsilon Charge Shifts*, *Phys. Lett.* **166B** (1986) 196.
- [24] J. Kumar and J.D. Wells, *CERN LHC and ILC probes of hidden-sector gauge bosons*, *Phys. Rev.* **D74** (2006) 115017 [[hep-ph/0606183](#)].
- [25] E.J. Chun, J.C. Park and S. Scopel, *Dark matter and a new gauge boson through kinetic mixing*, *JHEP* **02** (2011) 100 [[arXiv:1011.3300](#)].

- [26] **Fermi-LAT** Collaboration, M. Ackermann et al., *Dark matter constraints from observations of 25 Milky Way satellite galaxies with the Fermi Large Area Telescope*, *Phys. Rev.* **D89** (2014) 042001 [[arXiv:1310.0828](#)].
- [27] **Fermi-LAT** Collaboration, M. Ackermann et al., *Searching for Dark Matter Annihilation from Milky Way Dwarf Spheroidal Galaxies with Six Years of Fermi Large Area Telescope Data*, *Phys. Rev. Lett.* **115** (2015) 231301 [[arXiv:1503.0264](#)].
- [28] **H.E.S.S.** Collaboration, A. Abramowski et al., *Search for a Dark Matter annihilation signal from the Galactic Center halo with H.E.S.S.*, *Phys. Rev. Lett.* **106** (2011) 161301 [[arXiv:1103.3266](#)].
- [29] W. Buchmuller and C. Greub, *Electroproduction of Majorana neutrinos*, *Phys. Lett.* **B256** (1991) 465.
- [30] A. Pilaftsis, *Radiatively induced neutrino masses and large Higgs neutrino couplings in the standard model with Majorana fields*, *Z. Phys.* **C55** (1992) 275 [[hep-ph/9901206](#)].
- [31] A. Atre, T. Han, S. Pascoli and B. Zhang, *The Search for Heavy Majorana Neutrinos*, *JHEP* **05** (2009) 030 [[arXiv:0901.3589](#)].
- [32] B. Shuve and M.E. Peskin, *Revision of the LHCb Limit on Majorana Neutrinos*, *Phys. Rev.* **D94** (2016) 113007 [[arXiv:1607.0425](#)].
- [33] T. Sjostrand, S. Mrenna and P.Z. Skands, *A Brief Introduction to PYTHIA 8.1*, *Comput. Phys. Commun.* **178** (2008) 852 [[arXiv:0710.3820](#)].
- [34] M. Cirelli, M. Kadastik, M. Raidal and A. Strumia, *Model-independent implications of the  $e^+$ , anti-proton cosmic ray spectra on properties of Dark Matter*, *Nucl. Phys.* **B813** (2009) 1 [[arXiv:0809.2409](#)]. [Addendum: *Nucl. Phys.*B873,530(2013)].
- [35] M. Cirelli, G. Corcella, A. Hektor, G. Hutsi, M. Kadastik, P. Panci, M. Raidal, F. Sala and A. Strumia, *PPPC 4 DM ID: A Poor Particle Physicist Cookbook for Dark Matter Indirect Detection*, *JCAP* **1103** (2011) 051 [[arXiv:1012.4515](#)]. [Erratum: *JCAP*1210,E01(2012)].
- [36] M. Mateo, *Dwarf galaxies of the Local Group*, *Ann. Rev. Astron. Astrophys.* **36** (1998) 435 [[astro-ph/9810070](#)].
- [37] L.S. Sparke and J.S. Gallagher, *Galaxies in the universe.*, United Kingdom: Cambridge University Press. (2016).

- [38] V. Springel, S.D.M. White, C.S. Frenk, J.F. Navarro, A. Jenkins, M. Vogelsberger, J. Wang, A. Ludlow and A. Helmi, *Prospects for detecting supersymmetric dark matter in the Galactic halo*, *Nature* **456N7218** (2008) 73.
- [39] J. Diemand, M. Kuhlen, P. Madau, M. Zemp, B. Moore, D. Potter and J. Stadel, *Clumps and streams in the local dark matter distribution*, *Nature* **454** (2008) 735 [[arXiv:0805.1244](#)].
- [40] **H.E.S.S.** Collaboration, F. Acero, *Localising the VHE gamma-ray source at the Galactic Centre*, *Mon. Not. Roy. Astron. Soc.* **402** (2010) 1877 [[arXiv:0911.1912](#)].
- [41] W.A. Rolke, A.M. Lopez and J. Conrad, *Limits and confidence intervals in the presence of nuisance parameters*, *Nucl. Instrum. Meth.* **A551** (2005) 493 [[physics/0403059](#)].
- [42] S. Profumo, F.S. Queiroz and C.E. Yaguna, *Extending Fermi-LAT and H.E.S.S. Limits on Gamma-ray Lines from Dark Matter Annihilation*, *Mon. Not. Roy. Astron. Soc.* **461** (2016) 3976 [[arXiv:1602.0850](#)].
- [43] **H.E.S.S.** Collaboration, F. Aharonian et al., *Observations of the Crab Nebula with H.E.S.S.*, *Astron. Astrophys.* **457** (2006) 899 [[astro-ph/0607333](#)].
- [44] **H.E.S.S.** Collaboration, V. Lefranc and E. Moulin, *Dark matter search in the inner Galactic halo with H.E.S.S. I and H.E.S.S. II*, *PoS ICRC2015* (2016) 1208 [[arXiv:1509.0412](#)].
- [45] G. Cowan, K. Cranmer, E. Gross and O. Vitells, *Asymptotic formulae for likelihood-based tests of new physics*, *Eur. Phys. J.* **C71** (2011) 1554 [[arXiv:1007.1727](#)]. [Erratum: *Eur. Phys. J.*C73,2501(2013)].
- [46] **H.E.S.S.** Collaboration, H. Abdallah et al., *Search for dark matter annihilations towards the inner Galactic halo from 10 years of observations with H.E.S.S.*, *Phys. Rev. Lett.* **117** (2016) 111301 [[arXiv:1607.0814](#)].
- [47] G. Steigman, B. Dasgupta and J.F. Beacom, *Precise Relic WIMP Abundance and its Impact on Searches for Dark Matter Annihilation*, *Phys. Rev.* **D86** (2012) 023506 [[arXiv:1204.3622](#)].





*A theorist's only real hazard is stabbing himself with a pencil while attacking a bug that crawls out of his calculations.*

Leon M. Lederman

# 3

## Direct Detection of Sterile Neutrinos as Dark Matter Candidates

### 3.1 Introduction

If in the previous chapter we stressed the importance of the possible mediator particle in the case of WIMPs as dark matter particles, we focus here on the candidate itself. Departing from the WIMP paradigm, motivated by the arguments discussed in section 1.3.6, we consider the possibility of sterile neutrinos constituting the bulk of dark matter. We reviewed the theoretical aspects of this candidate in section 1.3.3.3, while in section 1.3.4.2 we mentioned some of the experimental techniques that have been developed to obtain signals of this elusive particle. In this chapter we focus our attention on the possibility of directly measuring sterile neutrino signals, presenting a novel method to constrain the sterile neutrino parameters using data coming from underground laboratories. These LXe experiments are originally tuned to detect interactions of the detector material with WIMPs, and their functioning principle is explained in section 3.2. The key process in which this new detection technique is based is described in section 3.3, while the constraints imposed by it is analysed in detail in section 3.5.

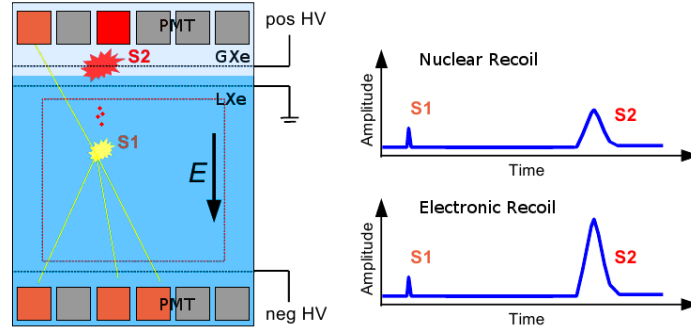


Figure 3.1: Left panel: Scheme of a TPC depicting the primary or scintillation signal ( $S1$ ) and the ionization or secondary signal ( $S2$ ). Right panel: Representation of the amplitude difference between ERs and NRs. Figure taken from [1].

## 3.2 Direct Detection in LXe Experiments

We briefly discussed LXe detectors in section 2.2.2.2, but in this section we describe the detection principle in detail as it is essential to discuss the procedure proposed in the next section.

The LXe inside the detector (which is kept at a temperature of  $-95^\circ\text{C}$  and  $\sim 2$  bar of pressure) can experience two different types of scattering: Electron Recoil (ER), from the interaction with  $\beta$ - and  $\gamma$ -rays and Nuclear Recoil (NR) from the interaction with neutrons or WIMPs. In both of these cases two effects can be exploited in order to obtain an approximate tridimensional reconstruction of the scattering, the excitation and ionization of the xenon atoms. The excitation forms an excimer that later decay emitting scintillation light at  $\sim 178\text{ nm}$  [1] which can be registered by radio pure photomultiplier tubes (PMTs) located in the upper and lower parts of the tank. This first signal is called  $S1$ . The ionized electrons, on the other hand, can be extracted in the upper part of the tank by applying an electromagnetic field. These drifted electrons interact later with xenon atoms in gaseous phase generating a secondary signal called  $S2$  proportional to the liberated charge which is also registered by the PMTs. This is the working principle behind TPCs, first suggested in 1970 [2] and later adapted for dark matter detection. They currently impose the strongest constraints on the cross section of dark matter with nucleons, with the leading experiments being XENONIT [3], LUX [4] and PandaX [5].

The working principle just described, depicted in the left panel of fig. 3.1, allows experimentalists to efficiently reconstruct the interaction point inside the detector (which is essential for *fiducialization*), while additionally providing several ways of background discrimination. In order to distinguish ERs from NRs

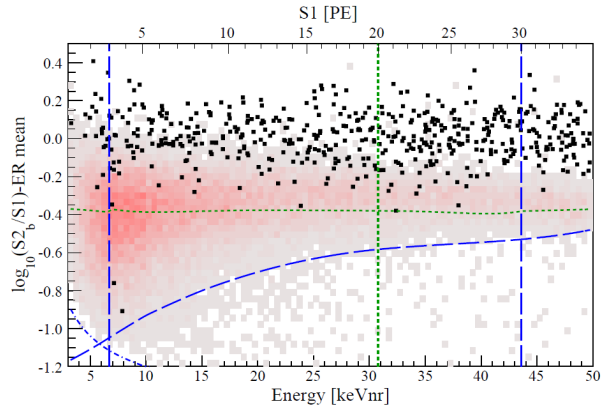


Figure 3.2: Event distribution in the discrimination parameter space  $\log_{10}(S2_b/S1)$  from 225 Live Days of XENON100 Data (black squares) as a function of the recoil energy (in keV) or the amplitude of the primary signal  $S1$  (in number of photoelectrons). The horizontal green dashed line rejects 99.75% of the ERs (upper region) from the NRs (lower region). The red and gray squares indicate the NR neutron calibration. Additional energy cuts are also displayed; more information can be found in the original source [6].

it is possible to use the fact that they produce a different charge-to-light ratio, as shown in the right panel of fig. 3.1. Cuts can be imposed then to define the signal region as shown in fig. 3.2. In this particular case the upper half represents the rejected ER events for the XENON100 experiment, after 225 days of data taking [6]. After this discrimination cut, the background events coming from neutrons interacting with the material are still present. Most of these come from the walls of the detector, for which an inner fiducial volume is defined, out of which events are excluded. A fraction of those neutron events that make it to the inner volume can still be eliminated by rejecting multiple scatter events, displaying more than one secondary signal for a given  $S1$ . Those events left constitute the irreducible background. In the case shown in fig. 3.2, for example,  $1.0 \pm 0.2$  events are expected, while 2 are measured.

### 3.3 Sterile Neutrinos and Bound Electrons

As established in the previous section, in the context of WIMP searches ERs constitute a source of background arising mainly from the intrinsic  $\beta$  decays of the traces of elements that still remain in the detector material after the purification process, such as  $^{222}\text{Rn}$  and  $^{85}\text{Kr}$ ; and from the  $\gamma$ -rays reaching the experiment despite the active and passive shielding. However, the information regarding ERs can still be used to probe non-conventional aspects of dark matter

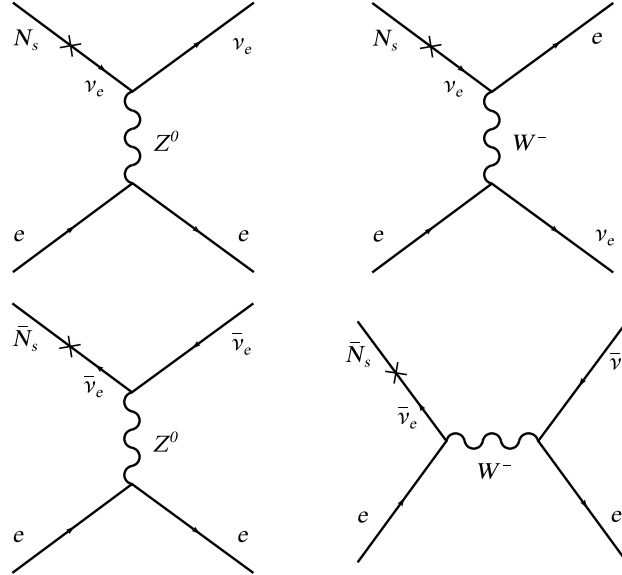


Figure 3.3: Feynman diagrams for the interaction between sterile (anti)neutrinos and electrons. The NC diagrams are presented in the left side, while those in the right side represent the CC interactions.

physics, like in [7] where this data is used to exclude leptophilic models that could explain the DAMA/LIBRA modulation signal [8], or like in [9] where it was used to constrain axions and ALPs exploiting the so-called axio-electric effect. Here we use the results obtained in [9] to obtain limits on another well motivated candidate: keV-scale sterile neutrinos.

This work is based on the inelastic CC+NC scattering  $N_S e^- \rightarrow \nu_e e^-$  and  $\bar{N}_S e^- \rightarrow \bar{\nu}_e e^-$ , shown in fig. 3.3, where a sterile (anti)neutrino  $N_S$  ( $\bar{N}_S$ ) mixing with an active state scatters an electron from a xenon atom. We analyse first the simpler case of the scattering off free electrons, to move later to the more realistic case of bound electrons, that require a special treatment. We assume here that dark matter is composed exclusively of sterile neutrinos with masses in the keV range, disregarding the specific production mechanism (some of them mentioned in section 1.3.3.3). If we adopt as a benchmark scenario the SHM discussed in section 1.3.2, the velocity of these particles in the MW is Maxwell-Boltzmann distributed around  $v \approx 200$  km/s (or  $\beta \approx 10^{-3}$ ). They are then non-relativistic and their energy is essentially their inertial mass  $E_S = m_S \sim$  keV. In the general case, the differential cross section between a sterile neutrino with momentum  $p_S = (E_S, \vec{p}_S)$  and an electron at rest such that  $p_e = (m_e, \vec{0})$

as a function of the scattered electron kinetic energy  $E_k$  is given by

$$\begin{aligned} \frac{d\sigma_{\text{free}}}{dE_k} = & 2 \frac{G_F^2}{\pi} |U_{S\ell}|^2 \frac{m_e}{|\vec{p}_S|^2} \left[ g_1^2 E_S \left( E_S + \frac{m_S^2}{2m_e} \right) \right. \\ & + g_2^2 (E_S - E_k) \left( E_S - E_k + \frac{m_S^2}{2m_e} \right) \\ & \left. - g_1 g_2 (m_e E_k + \frac{1}{2} m_S^2) \right]. \end{aligned} \quad (3.1)$$

The total cross section is the sum of the  $\nu_e e^-$  and  $\bar{\nu}_e e^-$  final states, although it is dominated by the  $\nu_e e^-$  channel. The difference between both final states is given by the definitions<sup>1</sup>

$$\begin{aligned} g_1^\nu &= g_2^{\bar{\nu}} := 1 + \frac{1}{2}(g_V + g_A), \\ g_2^\nu &= g_1^{\bar{\nu}} := \frac{1}{2}(g_V - g_A) \end{aligned} \quad (3.2)$$

with  $g_V = -\frac{1}{2} + 2 \sin^2 \theta_W$  and  $g_A = -\frac{1}{2}$ . The factor  $|U_{S\ell}|^2$  stands for the squared of the matrix element mixing sterile and active neutrinos ( $\nu_e$  in this particular case, although the case  $\ell = \mu, \tau$  can also be constrained through NC interactions as we will see), and it will be one of the free parameters to constrain in this model. As already mentioned in section 2.3, the appearance of the mixing angle is characteristic of these kind of processes and highly suppress them, as it is expected to be very small.

Eq. (3.1) cannot constitute the whole story due to the fact that electrons in the detector material are present as bound states. The coherence of the process dictates the importance of this fact. For example the authors in [10] analyse the case of a 5 keV sterile neutrino and consider, as a broad approximation, a coherent inelastic sterile neutrino-atom scattering, disregarding bound electrons. However we will examine in this work sterile neutrinos in the [10,50] keV mass range, which have correspondingly wavelengths around  $\mathcal{O}(10^{-8} - 10^{-9})$  cm. The atomic radius of the xenon atom is on the other hand  $\sim 1.1 \times 10^{-8}$  cm, implying that this case corresponds to incoherent scattering and the individual bound electrons must be taken into account. We will see that the scattering off bound electrons leads to larger recoil energies (although with lower cross sections) in comparison with the free electron case (see for example fig. 3.4), which will be essential for this analysis. At any rate, in order to obtain recoil energies above thresholds required for the experiments here considered (and discussed in section 3.4), masses higher than 20 keV are needed when considering the electrons as free states, hence entering the incoherent regime as it was just discussed.

<sup>1</sup>The values  $g_1^\nu$  and  $g_2^\nu$  must be used in eq. (3.1) for the scattering to neutrinos, while  $g_1^{\bar{\nu}}$  and  $g_2^{\bar{\nu}}$  for the scattering to anti-neutrinos.

electronic state $t$	1s	2s	2p	3s	3p	3d	4s	4p	4d	5s	4p
number of electrons	2	2	6	2	6	10	2	6	10	2	6
$\varepsilon_t$ (eV)	3456	5453	4893	1149	961	681	213	146	68	23	12

Table 3.1: Binding energy  $\varepsilon$  for the different electronic states  $t$  in xenon. Values taken from [11].

In order to describe the interaction with bound electrons we follow a similar procedure to that outlined in [11], adequately accounting for the non-zero mass of the incoming particle. The details of the calculation are properly described in appendix B. Suffice it to say here that in order to consider all the atomic wave functions we used the Roothan-Hartree-Fock method, using the experimental data on xenon atoms coming from [12]. If we define an effective mass for the bound electron

$$\tilde{m} := E_B^2 - |\vec{p}_B|^2, \quad (3.3)$$

where  $\vec{p}_B$  corresponds to the bound electron momentum and  $E_B = m_e - \varepsilon$  to its energy ( $\varepsilon$  being the binding energy, see table 3.1) and consider that a bound electron in the  $t = 1s, 2s, 2p, \dots, 5p$  state has angular variables  $(\theta_t, \phi_t)$ , the differential cross section between neutrinos and bound electrons, in the atom rest frame, is given by

$$\frac{d\sigma_t}{dE_k} = \int \frac{p_B^2 dp_B d(\cos \theta_t) d\phi_t}{(2\pi)^3} \frac{|\tilde{R}_t(\vec{p}_B)|^2}{4\pi} \frac{|\mathcal{M}|^2}{4E_S E_B |\beta - p_B/\tilde{m}|} \frac{1}{8\pi\lambda^{1/2}(s, m_S^2, \tilde{m}^2)} \left| \frac{du}{dE_k} \right|, \quad (3.4)$$

where the squared amplitude is given in eq. (B.4),  $\frac{du}{dE_k}$  in eq. (B.18), the radial wave functions of the bound electrons  $\tilde{R}_t(\vec{p}_B)$  defined in eq. (B.23) and

$$\lambda(a, b, c) := a^2 + b^2 + c^2 - 2ab - 2bc - 2ca \quad (3.5)$$

is the Källén function, with  $s$  and  $u$  the usual Mandelstam variables.

Eq. (3.4) needs to be integrated numerically, in this case using the program Mathematica 10.4 [13]. In fig. 3.4 we present an example of this calculation in comparison with the free electron case for a given choice of parameters, in this case  $m_S = 40$  keV and  $|U_{Se}|^2 = 10^{-6}$ . The threshold condition for the process to occur in the different bound states is given by  $E_S > \varepsilon_t$ . This is evidenced in fig. 3.4, where the most tightly bound electron in the 1s shell has a narrower kinematically allowed energy range in comparison to the more loosely bound states.

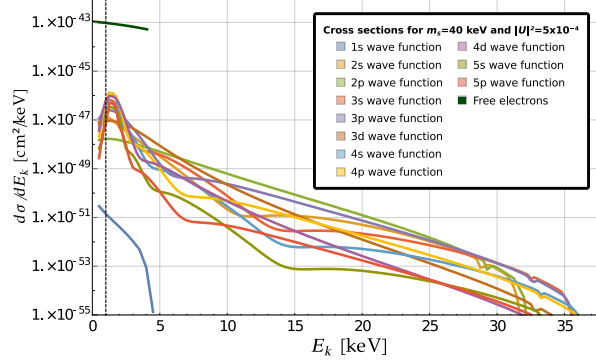


Figure 3.4: Differential cross section of massive sterile neutrinos with free (dark green) and bound electrons (light colors) for  $m_S = 40$  keV and  $|U_{Se}|^2 = 5 \times 10^{-4}$ . The vertical dashed line represents the lower threshold of  $E_{Th} = 1$  keV (see next section 3.4).

Given eq. (3.4), the differential event rate of the process, measured in differential rate units (dru):=(kg day keV) $^{-1}$ , is then

$$\frac{dR_t}{dE_k}(m_S, |U_{Se}|^2) = \frac{\rho_0}{m_S} n_e \int \frac{d\sigma_t}{dE_k}(m_S, |U_{Se}|^2) f(\beta) \beta d\beta, \quad (3.6)$$

where  $n_e$  is the number of electrons per kilogram of target material and  $f(\beta)$  the velocity distribution in the detector frame as defined in section 1.3.2. Effects present in WIMPs searches, such as annual modulation, would in principle also appear in this case, but are neglected for the sake of simplicity.

### 3.4 Experimental and Statistical Details

From the experimental point of view, the relevant quantity corresponds to the differential number of events. For a particular electronic configuration  $t$ , it directly depends on the mass of the detector  $M$  and the the exposure time  $T$  as

$$\frac{dN_t}{dE_k}(m_S, |U_{Se}|^2) = M \cdot T \cdot \frac{dR_t}{dE_k}(m_S, |U_{Se}|^2). \quad (3.7)$$

In this work we will focus in three particular experiments: XENON100, XENONIT and what is considered the ultimate dark matter detector, DARWIN. For the first two cases we take respectively

$$\begin{aligned} M_{100} &= 34 \text{ kg} & \& \quad T_{100} = 224.6 \text{ days} \\ M_{1T} &= 10^3 \text{ kg} & \& \quad T_{1T} = 2 \times 365 \text{ days.} \end{aligned} \quad (3.8)$$

If we were to take the XENONnT case, a global factor  $n$  would appear in comparison with XENONIT. By all means, other experimental aspects will be different

to the XENONIT case and are difficult to state at the moment. Due to these reasons, we do not include the XENONnT case here. For the DARWIN case we use an exposure of  $M \cdot T = 200 \text{ ton} \times \text{year}$ , as estimated in [14].

Besides general characteristics such as live time and the mass of the fiducialized target material, other experimental details must be taken into account before we can perform a statistical analysis. We consider the XENON100 experiment as a reference from here on, due to the high amount of detailed information related to its functioning. The global acceptance to ER events of the detector, for example, is essential in the low energy region which is where the signal is located, as we will see. Once appropriate selection cuts have been imposed (details can be found in [9]), the ER acceptance can be evaluated on calibration data obtained by exposing the detector to  $^{60}\text{Co}$  and  $^{232}\text{Th}$  sources. The resulting function can be seen in the upper panel of fig. 3.5, which weakens the signal for a small amount of registered photoelectrons (PE) in  $S1$ . This is due mainly to data quality criteria. In order to translate the dependency of this function to our theoretical variable, i.e. the kinetic energy of the recoil electron (in keV), we need a conversion function. This function takes into account all the details of the detector response, such as the scintillation efficiency and the quenching factor, using the NEST model [15]. It can be seen in the lower panel of fig. 3.5. In both of these plots a vertical dashed line can be observed at 3 PE ( $\sim 2 \text{ keV}$  using  $\text{Conv}(E_k)$ ) which represents the lower energy threshold ( $E_{\text{Th}}$ ) in XENON100. For the XENONIT experiment we will consider on the other hand  $E_{\text{Th}} = 1 \text{ keV}$ . Concerning the acceptance and conversion functions, we will take a conservative approach and use the same as those derived for XENON100, although it is expected the light collection to be increased in this case [16].

The total differential number of events is obtained then summing eq. (3.7) over all electronic states  $t$ , modulated with the corresponding detector acceptance

$$\frac{dN_T}{dE_k}(m_S, |U_{Se}|^2) = \sum_t \text{Acc}(\text{Conv}(E_k)) n_t \frac{dN_t}{dE_k}(m_S, |U_{Se}|^2), \quad (3.9)$$

where  $n_t$  is the number of electrons in the  $t$  state (see table 3.1).

Once the signal is defined, we need to compare it with the expected background. As already mentioned it is mostly composed of  $\gamma$  scattering off electrons and intrinsic  $\beta$  decays. It can be modelled using the calibration data previously stated. Both signal (blue curve) and background (red curve), as expected in the XENONIT experiment, can be seen in fig. 3.6 for particular values of the sterile neutrino mass and mixing angle, namely  $m_S = 40 \text{ keV}$  and  $|U_{Se}|^2 = 5 \times 10^{-4}$ . The lower threshold is established as a vertical dashed black line at 1 keV.

From the behaviour of both signal and background we can perform a block space analysis in order to obtain the statistical significance. We focus on the region in which the signal is over the noise and integrate to define



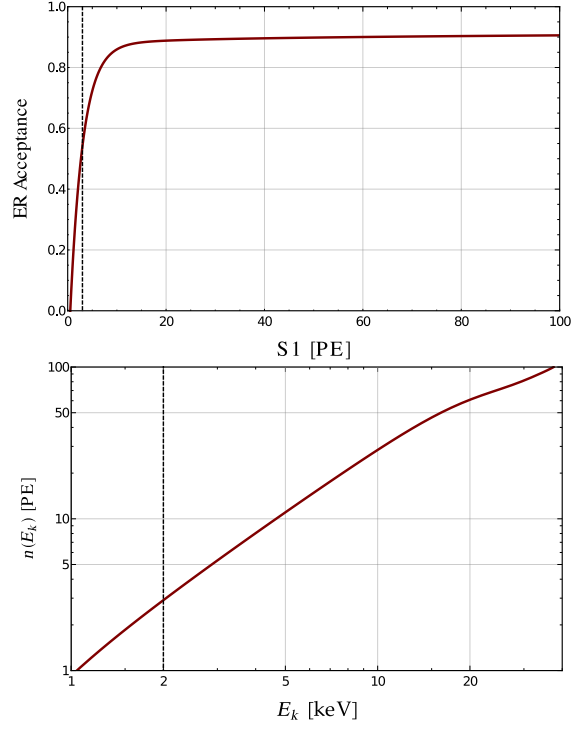


Figure 3.5: Upper panel: Acceptance function for the XENON100 experiment, evaluated on calibration data. Lower panel: Conversion function between the recorded number of PEs and recoil energy (in keV) for XENON100. Both functions reproduced from [9].

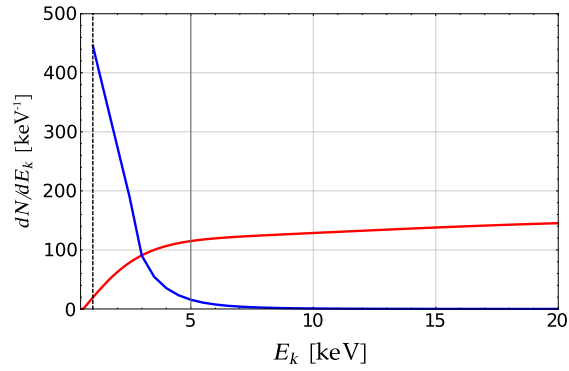


Figure 3.6: Differential number of events for bound electrons for  $m_S = 40$  keV and  $|U_{Se}|^2 = 5 \times 10^{-4}$  in XENON1T (blue) and estimated background  $F_b$  (red). The vertical dashed line represents lower threshold of  $E_{Th} = 1$  keV.

$$N_s := \int_{E_{\text{Th}}}^{E_0} \frac{dN_T}{dE_k} dE_k \quad \text{and} \quad N_b := \int_{E_{\text{Th}}}^{E_0} F_b dE_k. \quad (3.10)$$

The upper integration limit  $E_0$  represents the point where the signal intersects the background  $F_b$  or the upper bound of the electron recoil energy kinematically allowed, depending on which of those two values is lower. The background for the DARWIN case will be taken from [17] and extrapolated to the energy range here considered. The lower energy threshold and the acceptance function on the other hand will be conservatively taken as in the XENONIT case.

Finally, the statistical significance will be defined in terms of a  $\chi^2$  distribution as a function of  $N_s$  and  $N_b$ :

$$\chi^2(m_S, |U_{Se}|^2) := \frac{(N_s(m_S, |U_{Se}|^2) - N_b(m_S, |U_{Se}|^2))^2}{N_b(m_S, |U_{Se}|^2)}. \quad (3.11)$$

Imposing  $\chi^2 \geq 4.60$  (13.82) for a 90% (99.9%) C.L. the region in the  $m_S$  and  $|U_{Se}|^2$ -plane that can be excluded is obtained.

### 3.5 Results

Using eq. (3.11) with the exposure time in eq. (3.8) for the XENON100 and XENONIT detectors, we obtain the exclusion regions shown in fig. 3.7, in light and dark green respectively. We compare these results with current and future constraints imposed by other detectors. The purple curves show the exclusion limits imposed by current Earth-based experiments: the  $\beta$ -spectrum analysis of  $^{63}\text{Ni}$  [18] and  $^{35}\text{S}$  [19]. These results already exclude the region that XENON100 is able to probe diminishing the impact of this dataset. The limits imposed by XENONIT after two years of data taking however are much more interesting and are closer to detection than capture of keV-scale WDM neutrinos in  $\beta$ -decaying nuclei [26]. The DARWIN exclusion plot is shown in blue, where a total exposure of 200 ton $\times$ yr was used and is almost one order of magnitude better than for the XENONIT experiment. Of course, this exclusion limit is presented as a mere reference as thresholds and acceptance are expected to improve in comparison to the latter case. A future limit is also presented as a black curve: the expected 90% statistical exclusion limit of a differential measurement using a modified setup of the KATRIN experiment [20], after 3 years of live time. It will be much more constraining in terms of the mixing angle, although covering a reduced mass range. A confirmed measurement coming from neutrinoless double beta decay ( $0\nu\beta\beta$ ) experiments could eventually arise from a Majorana sterile neutrino, as it was discussed in section 1.4.2. Null-results impose the limit shown in red dashed, using  $|U_{Se}|^2 m_S < (0.3 \pm 0.1)$  eV (see for example [21] for details). Despite the fact that  $0\nu\beta\beta$  detectors provide stronger constraints

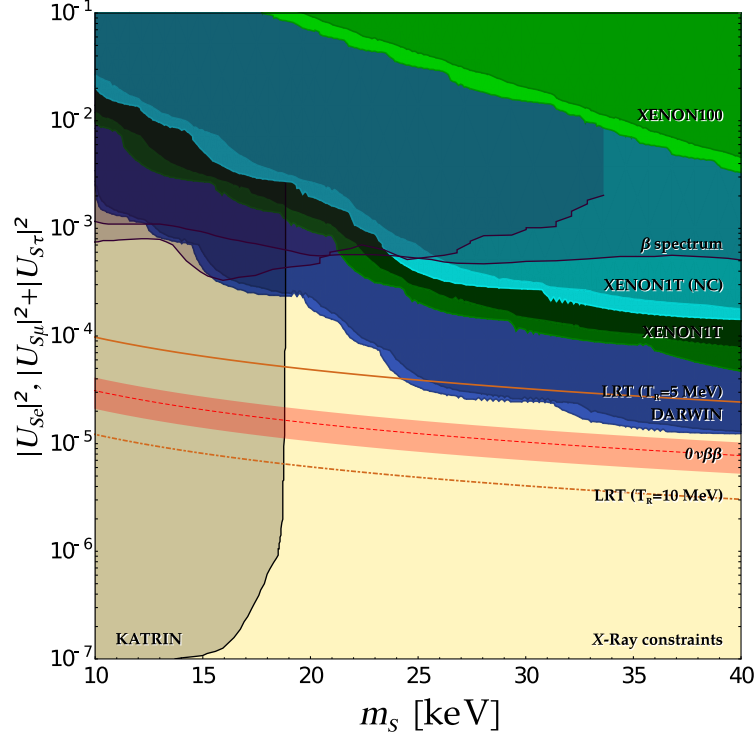


Figure 3.7: Light Green: Sensitivity on sterile neutrino WDM parameters for XENON100 as a function of  $m_s$  and  $|U_{Se}|^2$ . The contours delimit 90% and 99.9% C.L.

Dark Green: Equivalent for XENONIT;

Blue: Equivalent for DARWIN;

Purple: Current limits from analysis of  $\beta$  spectrum of different radioisotopes [18, 19];

Black: Expected statistical sensitivity of a modified KATRIN setup (Fig. 11 in [20]);

Red dashed: Limits coming from  $0\nu\beta\beta$  experiments [21];

Magenta dashed: Upper and lower bounds from Dodelson-Widrow production of DM [22];

Orange solid (and dot-dashed): Excluded area for production in case of a low reheating temperature (LRT) of  $T_R = 5$  MeV ( $T_R = 10$  MeV) [23];

Yellow: Constraint from X-ray searches [24, 25];

Turquoise: limit on  $|U_{S\mu}|^2 + |U_{S\tau}|^2$  if the sterile neutrino does not couple to electron neutrinos and only has neutral currents.

than direct detection experiments, they rely on the assumption of sterile neutrinos being Majorana particles and that there is no interference among the many possible mechanisms for double beta decay.

If the sterile neutrino were not to couple to electron neutrinos, it could still have NC interactions. This process can set limits on  $|U_{S\mu}|^2 + |U_{S\tau}|^2$  and it is shown as the turquoise region in fig. 3.7. In this case the other Earth-based experiments that can currently constrain the parameter space, i.e. beta and double

beta decays, do not apply.

We have not discussed here production mechanisms for this WDM candidate. The Dodelson-Widrow mechanism discussed in section 1.3.3.3 however, sets a limit for  $|U_{Se}|^2$  below  $10^{-9}$  according to [22]. This might not be the main way in which the relic abundance is achieved, but as it was mentioned, the process is unavoidable. Were the XENONIT or the DARWIN experiments measure a signal, it would imply that an alternative mechanism is at work. Additionally, its lifetime would be smaller than the age of the universe, possibly violating the stability condition established in section 1.3.3. One option to avoid the overproduction is to consider a low reheating temperature in inflationary models which would suppress the production of non-relativistic particles at  $T \lesssim T_R$  [23], departing then from the  $\Lambda$ CDM paradigm. Depending on the value of  $T_R$  different regions of the parameter space can be excluded. We take  $T_R = 5$  MeV and  $T_R = 10$  MeV and show the consequences of this assumption in fig. 3.7 as an orange solid and dot-dashed line respectively. Another possibility is to assume the insertion of additional entropy in the system, as in Refs. [27, 28]. Finally, in comparison to the direct detection mechanism proposed here, indirect detection techniques such as  $X$ -ray searches are much more constraining [24, 25] but rely in several astrophysical assumptions. The limit is shown in yellow and rules out the whole region of parameter space probed by the plot. Despite this, the exclusion limit that can be achieved using ER data from direct detection experiments can be one order of magnitude stronger than those set by other Earth-based limits and up to two using future experiments, improving the limits in a cosmologically independent way.

## References

- [1] M. Schumann, *Dual-Phase Liquid Xenon Detectors for Dark Matter Searches*, *JINST* **9** (2014) C08004 [[arXiv:1405.7600](#)].
- [2] B.A. Dolgoshein, V.N. Lebedenko and B.U. Rodionov, *New Method of Registration of Ionizing-particle Tracks in Condensed Matter*, *Soviet Journal of Experimental and Theoretical Physics Letters* **11** (June, 1970) 351.
- [3] **XENON** Collaboration, E. Aprile et al., *First Dark Matter Search Results from the XENON1T Experiment*, *Phys. Rev. Lett.* **119** (2017) 181301 [[arXiv:1705.0665](#)].
- [4] **LUX** Collaboration, D.S. Akerib et al., *Results from a search for dark matter in the complete LUX exposure*, *Phys. Rev. Lett.* **118** (2017) 021303 [[arXiv:1608.0764](#)].
- [5] **PandaX-II** Collaboration, X. Cui et al., *Dark Matter Results From 54-Ton-Day Exposure of PandaX-II Experiment*, *Phys. Rev. Lett.* **119** (2017) 181302 [[arXiv:1708.0691](#)].
- [6] **XENON100** Collaboration, E. Aprile et al., *Dark Matter Results from 225 Live Days of XENON100 Data*, *Phys. Rev. Lett.* **109** (2012) 181301 [[arXiv:1207.5988](#)].
- [7] **XENON100** Collaboration, E. Aprile et al., *Exclusion of Leptophilic Dark Matter Models using XENON100 Electronic Recoil Data*, *Science* **349** (2015) 851 [[arXiv:1507.0774](#)].
- [8] R. Bernabei et al., *New Results from DAMA/LIBRA: Final Model-Independent Results of Dama/Libra-Phase1 and Perspectives of Phase2*, *Frascati Phys. Ser.* **58** (2014) 41.
- [9] **XENON100** Collaboration, E. Aprile et al., *First Axion Results from the XENON100 Experiment*, *Phys. Rev.* **D90** (2014) 062009 [[arXiv:1404.1455](#)]. [Erratum: *Phys. Rev.* **D95**, no.2, 029904(2017)].
- [10] S. Ando and A. Kusenko, *Interactions of keV sterile neutrinos with matter*, *Phys. Rev.* **D81** (2010) 113006 [[arXiv:1001.5273](#)].
- [11] G.J. Gounaris, E.A. Paschos and P.I. Porfyriadis, *Electron spectra in the ionization of atoms by neutrinos*, *Phys. Rev.* **D70** (2004) 113008 [[hep-ph/0409053](#)].

- [12] C.F. Bunge, J.A. Barrientos and A.V. Bunge, *Rootaan-hartree-fock ground-state atomic wave functions: Slater-type orbital expansions and expectation values for  $z=2-54$* , *Atomic data and nuclear data tables* **53** (1993) 113.
- [13] Wolfram Research, Inc. , “Mathematica, Version 11.3.” Champaign, IL, 2018.
- [14] **DARWIN** Collaboration, J. Aalbers et al., *DARWIN: towards the ultimate dark matter detector*, *JCAP* **1611** (2016) 017 [[arXiv:1606.0700](#)].
- [15] M. Szydagis, N. Barry, K. Kazkaz, J. Mock, D. Stolp, M. Sweany, M. Tripathi, S. Uvarov, N. Walsh and M. Woods, *NEST: A Comprehensive Model for Scintillation Yield in Liquid Xenon*, *JINST* **6** (2011) P10002 [[arXiv:1106.1613](#)].
- [16] **XENON** Collaboration, E. Aprile et al., *Physics reach of the XENON1T dark matter experiment*, *JCAP* **1604** (2016) 027 [[arXiv:1512.0750](#)].
- [17] M. Schumann, L. Baudis, L. Buetikofer, A. Kish and M. Selvi, *Dark matter sensitivity of multi-ton liquid xenon detectors*, *JCAP* **1510** (2015) 016 [[arXiv:1506.0830](#)].
- [18] E. Holzschuh, W. Kundig, L. Palermo, H. Stussi and P. Wenk, *Search for heavy neutrinos in the beta spectrum of Ni-63*, *Phys. Lett.* **B451** (1999) 247.
- [19] E. Holzschuh, L. Palermo, H. Stussi and P. Wenk, *The beta-spectrum of S-35 and search for the admixture of heavy neutrinos*, *Phys. Lett.* **B482** (2000) 1.
- [20] S. Mertens, T. Lasserre, S. Groh, G. Drexlin, F. Glueck, A. Huber, A.W.P. Poon, M. Steidl, N. Steinbrink and C. Weinheimer, *Sensitivity of Next-Generation Tritium Beta-Decay Experiments for keV-Scale Sterile Neutrinos*, *JCAP* **1502** (2015) 020 [[arXiv:1409.0920](#)].
- [21] W. Rodejohann, *Neutrino-less Double Beta Decay and Particle Physics*, *Int. J. Mod. Phys.* **E20** (2011) 1833 [[arXiv:1106.1334](#)].
- [22] T. Asaka, M. Laine and M. Shaposhnikov, *Lightest sterile neutrino abundance within the nuMSM*, *JHEP* **01** (2007) 091 [[hep-ph/0612182](#)]. [Erratum: *JHEP*02,028(2015)].
- [23] G. Gelmini, S. Palomares-Ruiz and S. Pascoli, *Low reheating temperature and the visible sterile neutrino*, *Phys. Rev. Lett.* **93** (2004) 081302 [[astro-ph/0403323](#)].

- 
- [24] S. Horiuchi, P.J. Humphrey, J. Onorbe, K.N. Abazajian, M. Kaplinghat and S. Garrison-Kimmel, *Sterile neutrino dark matter bounds from galaxies of the Local Group*, *Phys. Rev.* **D89** (2014) 025017 [[arXiv:1311.0282](#)].
- [25] A. Kusenko, *Sterile neutrinos: The Dark side of the light fermions*, *Phys. Rept.* **481** (2009) 1 [[arXiv:0906.2968](#)].
- [26] Y.F. Li and Z.z. Xing, *Possible Capture of keV Sterile Neutrino Dark Matter on Radioactive  $\beta$ -decaying Nuclei*, *Phys. Lett.* **B695** (2011) 205 [[arXiv:1009.5870](#)].
- [27] F. Bezrukov, H. Hettmansperger and M. Lindner, *keV sterile neutrino Dark Matter in gauge extensions of the Standard Model*, *Phys. Rev.* **D81** (2010) 085032 [[arXiv:0912.4415](#)].
- [28] M. Nemevsek, G. Senjanovic and Y. Zhang, *Warm Dark Matter in Low Scale Left-Right Theory*, *JCAP* **1207** (2012) 006 [[arXiv:1205.0844](#)].





“We demand rigidly defined areas of doubt and uncertainty!”

Douglas Adams, *The Hitchhiker’s Guide to the Galaxy*

# 4

## Neutrino Masses in 2HDMs with a gauged $U(1)$

### 4.1 Introduction

The scalar sector of the SM presented in section 1.2.2 is composed by a single Higgs doublet. This particle was finally found, after almost 50 years of its proposal, by the ATLAS [1] and CMS [2] experiments at CERN. While its exact properties are still under study, the discovery represented a major breakthrough for the SM, while at the same time opening an experimental window for the search of an enlarged scalar sector. One of the simplest BSM possibilities in this sense is to introduce an additional scalar doublet. These extensions are known as Two Higgs-Doublet Models (2HDM) and have been thoroughly studied in the past [3]. Historically, they were first introduced by T. D. Lee back in 1973 while he was looking for new ways to generate  $CP$  violation [4]. A few years later Glashow and Weinberg, and Paschos independently, realized that in order to avoid Flavour Changing Neutral Interactions (FCNI) the fermions of a given electric charge can couple to—at most—one Higgs doublet [5, 6]. FCNI change the flavour of a fermion current, while conserving its electric charge and are not observed at tree level in the SM (left panel in fig. 4.1). Despite being allowed at loop-level, like in the *penguin* diagram in the right panel of fig. 4.1, the GIM mechanism suppresses them [7]. In order to avoid these experimentally constrained interactions [8], it is a common practice to include *ad-hoc* discrete symmetries like  $Z_2$ .

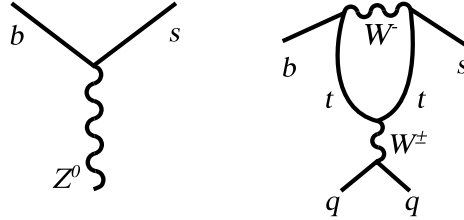


Figure 4.1: Left panel: *Forbidden tree-level FCNI in the SM.* Right panel: *GIM-suppressed loop-level FCNI in the SM.*

Up to this point we have considered different extensions to the SM with the goal of providing different approaches to the unresolved question of the nature of dark matter. We have examined enlarged gauge sectors, additional fermions and right-handed neutrinos. In this section we combine all these elements in the context of 2HDM and present, once again, the phenomenological aspects of our assumptions. The goal is to avoid FCNI through gauge principles and generate at the same time neutrino masses. We will also see that the collection of models developed can successfully accommodate dark matter candidates rather naturally.

We focus on the study of an additional  $U(1)$  symmetry due to its simplicity and the fact that once it is broken,  $Z_2$  appears as a remnant symmetry. As the particle content of the model can assume different quantum numbers under  $U(1)$  and still avoid FCNI, a collection of models stem from our requirements. A further restriction is for them to be anomaly-free, as we aim to obtain UV-complete models.

Once  $U(1)_X$  is broken, a massive gauge boson appears in the spectrum, as we saw in section 2.2, and in very much the same way, we will constrain these models analysing different kinds of experimental setups in a wide energy range, from atomic parity violation probes to LHC searches. The difference here is that, as we attempt to remain as general as possible, mass and kinetic mixing with the SM  $Z$  boson will be considered.

## 4.2 Two-Higgs Doublet Models

In this section we concisely introduce 2HDM, and then move to the most interesting case in which an additional gauge symmetry is introduced.

In order to not spoil the experimentally confirmed predictions of the SM, any BSM extension must comply with EWPT. Concerning extended scalar sectors, for example, the  $\rho$  parameter is particularly constraining, with a value given by

$\rho = 1.00040 \pm 0.00024$  obtained from a global fit [9]. It is defined as

$$\rho = \frac{\sum_{i=1}^n [I_{3,i}(I_{3,i} + 1) - \frac{1}{4} Y_i^2] v_i}{\sum_{i=1}^n \frac{1}{2} Y_i^2 v_i}. \quad (4.1)$$

with  $I_{3,i}$  and  $Y_i$  introduced in section 1.2.2 as the weak isospin and weak hypercharge, in this case of a scalar representation whose neutral component has a vev  $v_i$ . It can be seen that the only possibilities to not modify  $\rho = 1$  are the introduction of an  $SU(2)$  scalar doublet with  $Y_i = \pm 1$  or a scalar singlet with  $Y_i = 0$ . The first option leads to the 2HDM framework and generates the following Yukawa Lagrangian

$$\begin{aligned} -\mathcal{L}_{Y_{2\text{HDM}}} = & y^{1d} \bar{Q}_L \Phi_1 d_R + y^{1u} \bar{Q}_L \tilde{\Phi}_1 u_R + y^{1e} \bar{L}_L \Phi_1 e_R \\ & + y^{2d} \bar{Q}_L \Phi_2 d_R + y^{2u} \bar{Q}_L \tilde{\Phi}_2 u_R + y^{2e} \bar{L}_L \Phi_2 e_R + h.c., \end{aligned} \quad (4.2)$$

with

$$\Phi_i = \begin{bmatrix} \phi_i^+ \\ (v_i + \phi_i + i\eta_i)/\sqrt{2} \end{bmatrix}. \quad (4.3)$$

If a  $Z_2$  symmetry is introduced in order to avoid FCNI in such a way that

$$\begin{aligned} \Phi_1 & \rightarrow -\Phi_1, \\ \Phi_2 & \rightarrow +\Phi_2, \end{aligned} \quad (4.4)$$

a condition known as Natural Flavour Conservation (NFC) criterion, we obtain the following scalar potential

$$\begin{aligned} V(\Phi_1, \Phi_2) = & m_{11}^2 \Phi_1^\dagger \Phi_1 + m_{22}^2 \Phi_2^\dagger \Phi_2 - m_{12}^2 (\Phi_1^\dagger \Phi_2 + \Phi_2^\dagger \Phi_1) + \frac{\lambda_1}{2} (\Phi_1^\dagger \Phi_1)^2 \\ & + \frac{\lambda_2}{2} (\Phi_2^\dagger \Phi_2)^2 + \lambda_3 (\Phi_1^\dagger \Phi_1) (\Phi_2^\dagger \Phi_2) + \lambda_4 (\Phi_1^\dagger \Phi_2) (\Phi_2^\dagger \Phi_1) \\ & + \frac{\lambda_5}{2} \left[ (\Phi_1^\dagger \Phi_2)^2 + (\Phi_2^\dagger \Phi_1)^2 \right]. \end{aligned} \quad (4.5)$$

where we assume  $CP$  conservation, a condition that we will maintain throughout this chapter. The fermionic content of the model can have four different parities under  $Z_2$ , which eliminates some of the terms from the general Lagrangian eq. (4.2). The four models generated in this fashion are listed in table 4.1.

### 4.3 Gauging $U(1)_X$

In [10] it is shown that the necessary  $Z_2$  symmetry introduced in the previous section can stem from gauge principles. In particular, the authors consider a

<i>model</i>	$\Phi_1$	$\Phi_2$	$u_R$	$d_R$	$e_R$	$Q_L$	$L_L$
<i>type I</i>	–	+	+	+	+	+	+
<i>type II</i>	–	+	+	–	–	+	+
<i>lepton-specific</i>	–	+	+	+	–	+	+
<i>flipped</i>	–	+	+	–	+	+	+

Table 4.1: 2HDMs classified depending on the parities under  $Z_2$  of the fermionic and scalar content of the model.

$U(1)$  symmetry as the discrete symmetry origin and analyse the theoretical and, briefly, the experimental consequences of this choice, in the framework of the 4 types of 2HDM presented in table 4.1. We take a different approach here, focusing on the type-I model, in which the fermions couple only to  $\Phi_2$ , whose neutral component will be later associated with the 125 GeV Higgs scalar found at CERN. Additionally, our experimental analysis will be thorough, while general when possible.

In this section we provide the theoretical foundations of the family of models that we will study, while in the next section the experimental aspects are analysed in detail.

### 4.3.1 Anomaly Cancellation

The NFC condition in eq. (4.4) can be obtained if the two scalar doublets transform differently under  $U(1)$ . This further reduces the potential in eq. (4.5) to

$$\begin{aligned}
 V(\Phi_1, \Phi_2) = & m_{11}^2 \Phi_1^\dagger \Phi_1 + m_{22}^2 \Phi_2^\dagger \Phi_2 + \frac{\lambda_1}{2} (\Phi_1^\dagger \Phi_1)^2 + \frac{\lambda_2}{2} (\Phi_2^\dagger \Phi_2)^2 \\
 & + \lambda_3 (\Phi_1^\dagger \Phi_1) (\Phi_2^\dagger \Phi_2) + \lambda_4 (\Phi_1^\dagger \Phi_2) (\Phi_2^\dagger \Phi_1).
 \end{aligned}
 \tag{4.6}$$

The next step is to choose the fermionic charges under  $U(1)_X$  in order to obtain the appropriate masses. If we call  $l, q, e, u, d$  the fermion charges and  $h_1, h_2$  the scalar charges, gauge invariance demands

$$\begin{aligned}
 d - q + h_2 &= 0 \\
 u - q - h_2 &= 0 \\
 e - l + h_2 &= 0,
 \end{aligned}
 \tag{4.7}$$

while the only condition over  $h_1$  is, for the moment,  $h_1 \neq h_2$ . On top of this, if we impose anomaly cancellation, an additional condition appears, as discussed

in detail in appendix C (see eq. (C.17)):

$$u = -2d. \quad (4.8)$$

However, a key ingredient is still missing: right-handed neutrinos. If we add three sterile states with charge  $n$ , requiring

$$n = -(u + 2d) \quad (4.9)$$

suffices to obtain an anomaly free model.

### 4.3.2 Neutrino Masses

We discussed in detail the possibility of neutrino mass generation through the seesaw mechanism in section 1.4.3. We implement this mechanism here, in a version in which the bare mass term for the right-handed neutrinos is not introduced by hand but arising naturally. As we will see below, in order to achieve this we need an additional singlet

$$\Phi_s = \frac{1}{\sqrt{2}}(v_s + \rho_s + i\eta_s) \quad (4.10)$$

with charge  $h_s$  under  $U(1)_X$  that generates an extra term in the scalar potential shown in eq. (4.6)

$$V_s = m_s^2 \Phi_s^\dagger \Phi_s + \frac{\lambda_s}{2} (\Phi_s^\dagger \Phi_s)^2 + \mu_1 \Phi_1^\dagger \Phi_1 \Phi_s^\dagger \Phi_s + \mu_2 \Phi_2^\dagger \Phi_2 \Phi_s^\dagger \Phi_s + \left( \mu \Phi_1^\dagger \Phi_2 \Phi_s + \text{h.c.} \right), \quad (4.11)$$

which requires  $h_s = h_1 - h_2$  in order to get gauge invariance. The Yukawa Lagrangian for neutrinos now reads

$$-\mathcal{L} \supset y_{ij}^D \bar{L}_{iL} \tilde{\Phi}_2 N_{jR} + Y_{ij}^M \overline{(N_{iR})^c} \Phi_s N_{Rj}, \quad (4.12)$$

leading to the seesaw type-I mechanism

$$m_\nu = -m_D^T M_R^{-1} m_D, \quad (4.13)$$

with  $m_D = \frac{y^D v_2}{2\sqrt{2}}$  and  $M_R = \frac{y^M v_s}{2\sqrt{2}}$ . If we take for example  $v_s \sim \mathcal{O}(\text{TeV})$ ,  $y^D \sim 10^{-4}$  and  $y^M \sim 1$ , we obtain active neutrino masses in agreement with current bounds  $m_\nu \sim 0.1$  eV. In particular, with sufficiently suppressed Yukawa couplings,  $y^M \ll 1$ , keV sterile neutrinos are also viable, possibly leading to the scenario discussed in chapter 3.

The Majorana mass term in eq. (4.12) is gauge invariant if  $2n + h_s = 0$ , which combined with the constraints on  $n$  and  $h_s$  translates into

$$h_1 = \frac{5u}{2} + \frac{7d}{2}. \quad (4.14)$$

$U(1)_X$	<i>fields</i>									
	$u_R$	$d_R$	$Q_L$	$L_L$	$e_R$	$N_R$	$\Phi_2$	$\Phi_1$	$\Phi_s$	
	<i>charges</i>									
	$u$	$d$	$\frac{(u+d)}{2}$	$\frac{-3(u+d)}{2}$	$-(2u+d)$	$-(u+2d)$	$\frac{(u-d)}{2}$	$\frac{5u}{2} + \frac{7d}{2}$	$2u+4d$	
$U(1)_A$	1	-1	0	0	-1	1	1	-1	-2	
$U(1)_B$	-1	1	0	0	1	-1	-1	1	+2	
$U(1)_C$	1/2	-1	-1/4	3/4	0	3/2	3/4	9/4	6/4	
$U(1)_D$	1	0	1/2	-3/2	-2	-1	1/2	5/2	2	
$U(1)_E$	0	1	1/2	-3/2	-1	-2	7/2	-1/2	-4	
$U(1)_F$	4/3	2/3	1	-3	-4	-8/3	1/3	17/3	16/3	
$U(1)_G$	-1/3	2/3	1/6	-1/2	0	-1	-1/2	-3/2	-2	
$U(1)_{B-L}$	1/3	1/3	1/3	-1	-1	-1	0	2	2	
$U(1)_Y$	2/3	-1/3	1/6	-1/2	-1	$\times$	1/2	$\neq h_2$	0	
$U(1)_N$	0	0	0	0	0	$\times$	0	$\neq h_2$	0	

*Table 4.2: Type-I 2HDM with an additional gauged  $U(1)_X$  symmetry and the quantum numbers of the particle content of the model under this symmetry. The upper block describe models that can explain neutrino masses and forbid FCNI, while the lower block can achieve just the second.*

This final condition settles all the free quantum numbers in terms of  $u$  and  $d$  and determines the family of models which can be generated fulfilling our conditions. These are summarized in table 4.2. The first block can address both the neutrino mass problem and the FCNI problem, while the second block ( $U(1)_Y$  and  $U(1)_N$ ) can address just the latter. From this list, probably the most well studied group, in different contexts, is  $U(1)_{B-L}$  in which the accidental baryon and lepton global symmetries are gauged [11-16].

The SSB decay chain goes as follow,

$$\begin{aligned}
& SU(3)_C \times SU(2)_L \times U(1)_Y \times U(1)_X \\
& \quad \Downarrow \langle \Phi_s \rangle = v_s \\
& SU(3)_C \times SU(2)_L \times U(1)_Y \times Z_2 \\
& \quad \Downarrow \langle \Phi_2 \rangle = v_2 \\
& SU(3)_C \times U(1)_{em} \times Z_2,
\end{aligned} \tag{4.15}$$

where  $v_s$  breaks  $U(1)_X$  and  $v_2$  finally breaks the group down to  $G_{\text{SM}} \times Z_2$ . The scale  $v_1$  is free as long as

$$v_1^2 + v_2^2 = v^2 \quad (4.16)$$

with  $v = 246$  GeV.

### 4.3.3 $Z'$ Strikes Again

In this subsection we deal with the gauge sector of the model, in order to obtain the relevant parameters that will allow us to put limits on it, based on additional gauge bosons searches. Unlike the analysis performed in section 2.2, we consider all possible terms guided by gauge principles, which include kinetic mixing among the gauge bosons. The most general gauge Lagrangian reads in this case

$$\mathcal{L}_{\text{gauge}} = -\frac{1}{4}\hat{B}_{\mu\nu}\hat{B}^{\mu\nu} + \frac{\epsilon}{2\cos\theta_W}\hat{X}_{\mu\nu}\hat{B}^{\mu\nu} - \frac{1}{4}\hat{X}_{\mu\nu}\hat{X}^{\mu\nu}, \quad (4.17)$$

where  $\epsilon$  is the kinetic mixing parameter, that must fulfil  $\epsilon \ll 1$  in order to respect EWPT. The covariant derivative concerning the  $SU(2)_L \times U(1)_Y \times U(1)_X$  sector, first introduced in eq. (1.6), is in this case

$$D_\mu = \partial_\mu + igT^a W_\mu^a + ig'\frac{Q_Y}{2}\hat{B}_\mu + ig_X\frac{Q_X}{2}\hat{X}_\mu, \quad (4.18)$$

where  $W_\mu^a$ ,  $g$  and  $T^a$  are the  $SU(2)_L$  gauge bosons, coupling constant and generators respectively;  $\hat{X}_\mu$ ,  $g_X$  and  $Q_X$  are the  $U(1)_X$  gauge boson, coupling constant and charge respectively; while  $\hat{B}_\mu$ ,  $g'$  and  $Q_Y$  the analogous for  $U(1)_Y$ . The hats indicate that these are not the physical fields. In order to obtain the physical ones we need to diagonalize the neutral gauge boson mass matrix. In the regime in which the physical gauge boson coming from  $U(1)_X$ , that we will call  $Z'$ , is much lighter than the SM  $Z^0$  we obtain the following masses [17, 18],

$$\begin{aligned} m_{Z^0}^2 &= \frac{g^2 v^2}{4\cos^2\theta_W} \\ m_{Z'}^2 &= \frac{v_s^2}{4}g_X^2 q_X^2 + \frac{g_X^2 v^2 \cos^2\beta \sin^2\beta}{4}(Q_{X1} - Q_{X2})^2, \end{aligned} \quad (4.19)$$

where  $q_X$ ,  $Q_{X1}$ ,  $Q_{X2}$  are the charges under  $U(1)_X$  of the singlet scalar, Higgs doublets  $\Phi_1$  and  $\Phi_2$  respectively and  $\tan\beta = v_2/v_1$ .

We will impose some experimental limits in terms of the parameter

$$\delta := \frac{2\cos\beta\cos\beta_d}{\sqrt{q_X^2 + \cos^2\beta_d(\sin^2\beta(Q_{X1} - Q_{X2})^2 - q_X^2)}}, \quad (4.20)$$

where

$$\tan\beta_d = \frac{v_s}{v_1}. \quad (4.21)$$

Using this definition, the  $Z'$  mass term can be rewritten simply as

$$m_{Z'} = \frac{g_X v \cos^2 \beta}{\delta}. \quad (4.22)$$

Finally, we parametrize the mixing among the gauge bosons in function of

$$\xi := \epsilon_Z + \epsilon \cot \theta_W, \quad (4.23)$$

where

$$\epsilon_Z := \frac{g_X}{g_Z} (Q_{X1} \cos^2 \beta + Q_{X2} \sin^2 \beta) \quad (4.24)$$

is the mass-mixing parameter.

In terms of these quantities, and having obtained the physical fields, we obtain the following Lagrangian describing the NC interactions

$$\begin{aligned} \mathcal{L}_{\text{NC}} = & -e J_{\text{em}}^\mu A_\mu - \frac{g}{2 \cos \theta_W} J_{\text{NC}}^\mu Z_\mu - \left( \epsilon e J_{\text{em}}^\mu + \epsilon_Z \frac{g}{2 \cos \theta_W} J_{\text{NC}}^\mu \right) Z'_\mu \\ & + \frac{1}{4} g_X \sin \xi [(Q_{Xf}^R + Q_{Xf}^L) \bar{\psi}_f \gamma^\mu \psi_f + (Q_{Xf}^R - Q_{Xf}^L) \bar{\psi}_f \gamma^\mu \gamma_5 \psi_f] Z_\mu \\ & - \frac{1}{4} g_X \cos \xi [(Q_{Xf}^R + Q_{Xf}^L) \bar{\psi}_f \gamma^\mu \psi_f - (Q_{Xf}^L - Q_{Xf}^R) \bar{\psi}_f \gamma^\mu \gamma_5 \psi_f] Z'_\mu, \end{aligned} \quad (4.25)$$

where  $Q_X^R$  ( $Q_X^L$ ) are the left-handed (right-handed) fermion charges under  $U(1)_X$ . The gauge sector of the resulting collection of models discussed here is very similar to that of the dark photon models [19, 20], with the difference that in the latter just the kinetic mixing is present. In the upper panel of fig. 4.2 the branching ratios of the dark photon as a function of its mass is shown, in the  $[10^{-3}, 10]$  GeV range. In comparison, we show in the other panels of the same figure the branching ratios for all the models presented in the upper block of table 4.2. The green (red) curve represents the combined branching ratios of  $Z'$  decaying into  $u\bar{u} + d\bar{d} + s\bar{s}$  ( $e^+e^- + \mu^+\mu^- + \tau^+\tau^-$ ). In comparison to the dark photon model, most models here considered allow decays into neutrinos, depicted as a blue curve.

As we can see, the decays of the  $Z'$  in this framework differ considerably from those concerning the  $Z'$  introduced in section 2.2. We analyse in detail the phenomenology arising from these considerations in the next section.

## 4.4 Phenomenological Constraints

As we mentioned in section 1.3.5, UV complete theories present a significant drawback: the high number of free parameters. Consequently, in order to constrain them we make use of a wide variety of experimental setups. The main



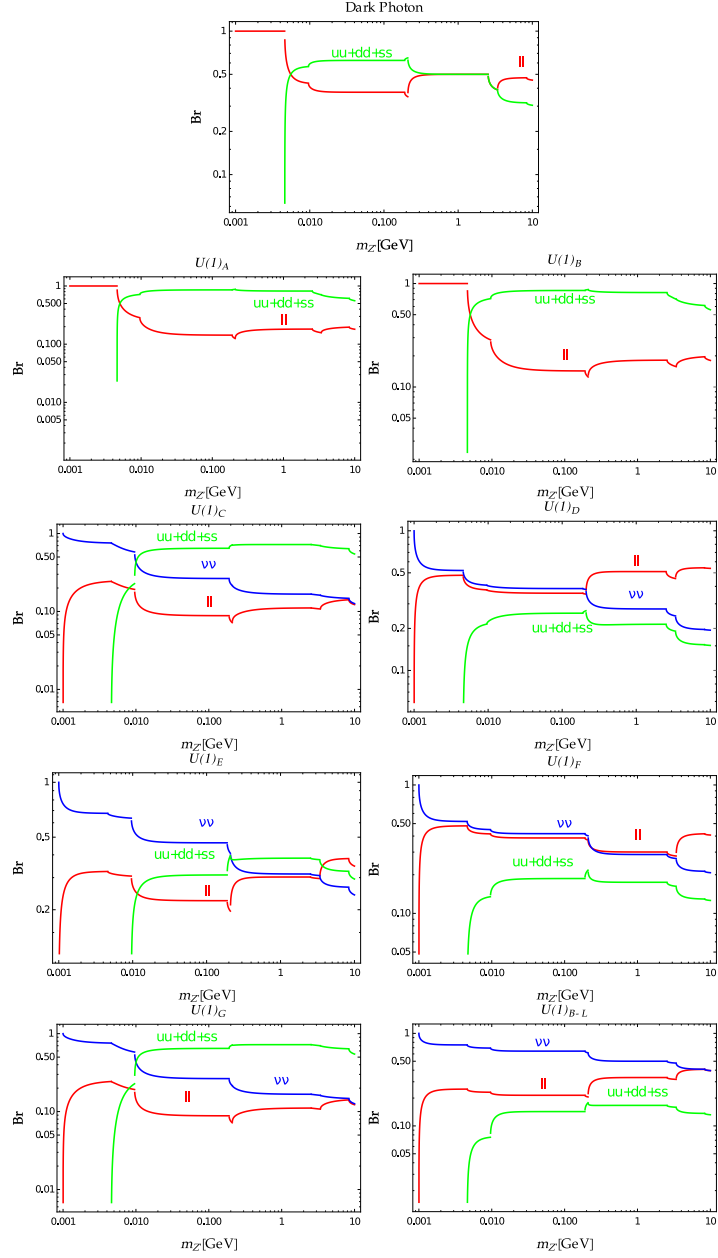


Figure 4.2: Branching ratios as a function of the  $Z'$  mass for several of the  $U(1)_X$  models under study.

<i>vertices</i>	<i>coupling</i>
$Ht\bar{t}, Hb\bar{b}, H\tau\bar{\tau}$	$\frac{\sin \alpha}{\sin \beta}$
$HWW, HZZ$	$\cos(\beta - \alpha)$
$ht\bar{t}, hb\bar{b}, h\tau\bar{\tau}$	$\frac{\cos \alpha}{\sin \beta}$
$hWW, hZZ$	$\sin(\beta - \alpha)$

Table 4.3: Scalar interactions in the type-I 2HDM.

purpose of this section is to review them and assess their importance limiting these free parameters.

Despite the fact that our goal is to describe the family of models obtained in the previous section from a general point of view, we will sometimes have to abandon it here in order to provide a qualitative analysis.

#### 4.4.1 Higgs Physics

The scalar spectrum in our models consists of two doublets and one singlet. In order to avoid unnecessary complications, we assume that the singlet does not mix with the doublets, which means that we can neglect  $\mu$ ,  $\mu_1$  and  $\mu_2$  in eq. (4.11). If we call  $H$  and  $h$  the resulting physical states from the  $CP$ -even neutral part of the Higgs doublets, their mixing can be parametrized with an angle  $\alpha$

$$\begin{bmatrix} H \\ h \end{bmatrix} = \begin{bmatrix} \cos \alpha & \sin \alpha \\ -\sin \alpha & \cos \alpha \end{bmatrix} \cdot \begin{bmatrix} \phi_1 \\ \phi_2 \end{bmatrix} \quad (4.26)$$

with

$$\tan 2\alpha = \frac{2(\lambda_3 + \lambda_4)v_1v_2}{\lambda_1v_1^2 - \lambda_2v_2^2}. \quad (4.27)$$

In this case the masses of the physical fields are given by [21]

$$\begin{aligned} m_s^2 &= \lambda_s v_s^2, \\ m_h^2 &= \frac{1}{2} \left( \lambda_1 v_1^2 + \lambda_2 v_2^2 - \sqrt{(\lambda_1 v_1^2 - \lambda_2 v_2^2)^2 + 4(\lambda_3 + \lambda_4)^2 v_1^2 v_2^2} \right), \\ m_H^2 &= \frac{1}{2} \left( \lambda_1 v_1^2 + \lambda_2 v_2^2 + \sqrt{(\lambda_1 v_1^2 - \lambda_2 v_2^2)^2 + 4(\lambda_3 + \lambda_4)^2 v_1^2 v_2^2} \right). \end{aligned} \quad (4.28)$$

From this equation, it is clear that, as  $H$  is the SM-like Higgs, the additional scalar  $h$  is lighter. The couplings of both scalars to pairs of SM-particles can be seen in table 4.3. The quantities in the second column are the overall multiplicative factor in front of the SM couplings. In other words  $H$  interacts with

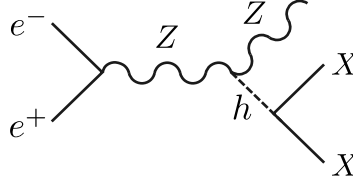


Figure 4.3: Feynman diagram for Higgs production at LEP, followed by its invisible decay.

fermions and gauge bosons identically to the SM Higgs, when  $\alpha = \beta$ . As the main decay of the light scalar is to  $Z'$  pairs, we can use invisible Higgs decay searches in order to put limits on the relevant parameter. In particular LEP performed these searches, which were focused on production with additional  $Z$  bosons [22–24], as in fig. 4.3. Using these experimental results, it is possible to set limits on

$$\frac{\sigma(Zh)}{\sigma(ZH_{SM})} \text{Br}(h \rightarrow \text{inv}). \quad (4.29)$$

Furthermore, if we assume that  $\text{Br}(h \rightarrow \text{inv}) \approx 1$ , these limits translate into  $\sin^2(\beta - \alpha)$  limits, as it is obvious from the last row of table 4.3. The corresponding constraints are shown in fig. 4.4, as a function of  $m_h$  and set a lower bound around

$$\sin^2(\beta - \alpha) \lesssim 0.1 \quad (4.30)$$

if  $m_h < 90$  GeV.

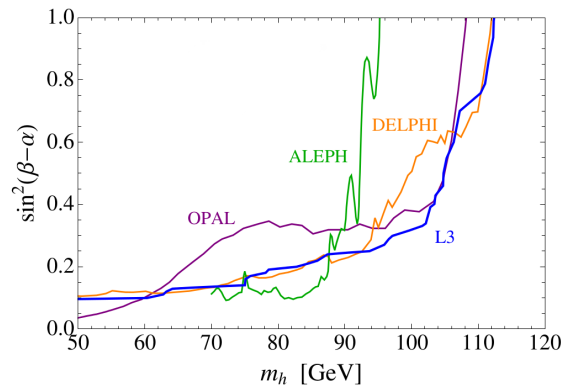


Figure 4.4: Upper limits from invisible Higgs decay searches translated to the light Higgs mass  $m_h$ . Figure taken from [21].

<i>Higgs decay channel</i>	<i>branching ratio</i>	<i>error</i>
$b\bar{b}$	$5.84 \times 10^{-1}$	1.5%
$c\bar{c}$	$2.89 \times 10^{-2}$	6.5%
$gg$	$8.18 \times 10^{-2}$	4.5%
$ZZ'$	$2.62 \times 10^{-1}$	2%
$WW'$	$2.14 \times 10^{-1}$	2%
$\tau^+\tau^-$	$6.27 \times 10^{-2}$	2%
$\mu^+\mu^-$	$2.18 \times 10^{-4}$	2%
$\gamma\gamma$	$2.27 \times 10^{-3}$	2.6%
$Z\gamma$	$1.5 \times 10^{-3}$	6.7%
$ZZ' \rightarrow 4\ell$	$2.745 \times 10^{-4}$	2%
$ZZ' \rightarrow 2\ell 2\nu$	$1.05 \times 10^{-4}$	2%

Table 4.4: List of experimental limits on the branching ratio of the SM Higgs.

Since the Higgs discovery in 2012, the LHC has been analysing the properties of this scalar particle in great detail. In particular they have been able to obtain its branching ratios to an outstanding precision, as it can be seen in table 4.4, where the channel  $ZZ' \rightarrow 2\ell 2\nu$  was obtained using the relation

$$\text{Br}(H \rightarrow ZZ' \rightarrow 2\ell 2\nu) = \text{Br}(H \rightarrow ZZ')\text{Br}(Z \rightarrow 2\ell)\text{Br}(Z \rightarrow 2\nu)^2. \quad (4.31)$$

The last two rows of this table are particularly useful, as we consider the  $M_{Z'} \ll M_H$  regime. As the decay widths of these channels are given by [21]

$$\Gamma(H \rightarrow ZZ') = \frac{g_Z^2}{64\pi} \frac{(M_H^2 - M_Z^2)^3}{M_H^3 M_Z^2} \delta^2 \tan \beta^2 \sin^2(\beta - \alpha), \quad (4.32)$$

and

$$\Gamma(H \rightarrow Z'Z') = \frac{g_Z^2}{128\pi} \frac{M_H^3}{M_Z^2} \delta^4 \tan \beta^4 \left( \frac{\cos^3 \beta \sin \alpha + \sin^3 \beta \cos \alpha}{\cos \beta \sin \beta} \right)^2. \quad (4.33)$$

we can use this information to constrain the  $\delta$  parameter, which results in

$$\delta^2 \leq \frac{4.6 \times 10^{-6}}{\text{Br}(Z' \rightarrow \ell^+\ell^-) \sin^2(\beta - \alpha) \tan \beta^2}. \quad (4.34)$$

### 4.4.2 Rare Meson Decays

If kinematically allowed, rare mesons decays can also contribute to interesting constraints. In particular, the branching ratio of  $K^+$  decaying to  $\pi^+ Z'$  in a 2HDM with mass mixing like the one in which we are interested, is estimated to be [25]

$$\text{Br}(K^+ \rightarrow \pi^+ Z') \simeq 4 \times 10^{-4} \delta^2, \quad (4.35)$$

which can be compared to rare meson decays searches [9],

$$\begin{aligned} \text{Br}(K^+ \rightarrow \pi^+ e^+ e^-)_{\text{exp}} &= (3.00 \pm 0.09) \times 10^{-7}, \\ \text{Br}(K^+ \rightarrow \pi^+ \mu^+ \mu^-)_{\text{exp}} &= (9.4 \pm 0.6) \times 10^{-8}, \\ \text{Br}(K^+ \rightarrow \pi^+ \nu \bar{\nu})_{\text{exp}} &= (1.7 \pm 1.1) \times 10^{-10} \end{aligned} \quad (4.36)$$

in order to obtain the following limits on  $\delta$

$$\begin{aligned} \delta &\lesssim \frac{2 \times 10^{-2}}{\sqrt{\text{Br}(Z' \rightarrow \ell^+ \ell^-)}}, \\ \delta &\lesssim \frac{7 \times 10^{-4}}{\sqrt{\text{Br}(Z' \rightarrow \text{missing energy})}}. \end{aligned} \quad (4.37)$$

In the same way, we can use rare  $B$  decays to impose similar constraints. As the limits on these decays are given by [9],

$$\begin{aligned} \text{Br}(B^+ \rightarrow K^+ l^+ l^-)_{\text{exp}} &< 4.5 \times 10^{-7}, \\ \text{Br}(B^+ \rightarrow K^+ \bar{\nu} \nu)_{\text{exp}} &< 1.6 \times 10^{-5}, \end{aligned} \quad (4.38)$$

and the decay of  $B$  to  $K Z'$  is estimated to be [25-27],

$$\text{Br}(B \rightarrow K Z') \simeq 0.1 \delta^2, \quad (4.39)$$

we arrive at the following constraints on  $\delta$ ,

$$\begin{aligned} \delta &\lesssim \frac{2 \times 10^{-3}}{\sqrt{\text{Br}(Z' \rightarrow l^+ l^-)}}, \\ \delta &\lesssim \frac{1.2 \times 10^{-2}}{\sqrt{\text{Br}(Z' \rightarrow \text{missing energy})}}. \end{aligned} \quad (4.40)$$

As in the previous case, a model needs to be selected in order to obtain the proper branching ratios of  $Z'$ . If  $Z'$  happens to decay mostly into charged leptons, for example, the bound arising from rare  $B$  decays will be more constraining than that from  $K$  decays, as it can be seen by comparing eq. (4.40) with eq. (4.37).

### 4.4.3 Atomic Parity Violation

While high energy colliders experiments provide a direct observation of new particles which is certainly useful in the context of the models here discussed, low energy searches provide indirect yet highly precise probes. In particular Atomic Parity Violation (APV) is aptly suited to test the existence of neutral light bosons.

The parity non-conservation measurements are interpreted in terms of the weak nuclear charge  $Q_W$ , that quantifies the strength of the electroweak coupling between atomic electrons and quarks in the nucleus and can be expressed as

$$Q_W^{\text{SM}} = -N + (1 - 4 \sin^2 \theta_W Z + \text{rad. corr.}), \quad (4.41)$$

where  $Z$  and  $N$  are the numbers of protons and neutrons of the nucleus under study and the radiative corrections are not explicitly taken into account.

On the other hand, the contribution coming from  $Z'$  can be quantified as [28]

$$\begin{aligned} \Delta Q_W = & -\delta^2 Q_W^{\text{SM}} - \delta^2 4Z \sin \theta_W \cos \theta_W \frac{\epsilon}{\epsilon_Z} - \delta^2 \frac{(q+u)(2Z+N)}{Q_{x1} \cos^2 \beta + Q_{x2} \sin^2 \beta} \\ & - \delta^2 \frac{(q+d)(Z+2N)}{Q_{x1} \cos^2 \beta + Q_{x2} \sin^2 \beta} \left( 1 - \frac{l-e}{Q_{x1} \cos^2 \beta + Q_{x2} \sin^2 \beta} \right), \end{aligned} \quad (4.42)$$

where  $l, e, q, u, d, Q_{x1}, Q_{x2}$  are the  $U(1)_X$  charges formerly introduced.

Knowing that the difference between the SM prediction for the weak nuclear charge in the caesium case [29]

$$Q_W^{\text{SM}} = -73.16(5) \quad (4.43)$$

and the measured value ( $Q_W^{\text{exp}}$ ) is, at 90% C. L. [30],

$$|\Delta Q_W(\text{Cs})| = |Q_W^{\text{exp}} - Q_W^{\text{SM}}| < 0.6, \quad (4.44)$$

we can arrive at a general APV expression for  $U(1)_X$  models for the caesium nucleus

$$\begin{aligned} & \left| 73.16\delta^2 - 220\delta^2 \left( \frac{\epsilon}{\epsilon_Z} \right) \sin \theta_W \cos \theta_W - \delta^2 \frac{188(q+u)}{Q_{x1} \cos^2 \beta + Q_{x2} \sin^2 \beta} \right. \\ & \left. - \delta^2 \frac{211(q+d)}{Q_{x1} \cos^2 \beta + Q_{x2} \sin^2 \beta} \left( 1 - \frac{l-e}{Q_{x1} \cos^2 \beta + Q_{x2} \sin^2 \beta} \right) \right| \times K(M_{Z'}; \text{Cs}) < 0.6, \end{aligned} \quad (4.45)$$

where the correction factor  $K(M_{Z'}; \text{Cs})$  is introduced for low values of  $M_{Z'}$ , when the local limit approximation is not valid. Different values for this correction factor are listed in Table I of [28]. In order to obtain a more quantitative

<i>experiment</i>	$\langle Q \rangle$	$\sin^2 \theta_W(M_Z)$	$\epsilon^2$ constrain at 90% C.L.
<i>Caesium APV</i>	2.4 MeV	0.2313(16)	$\epsilon^2 < \frac{39 \times 10^{-6}}{\delta^2} \left( \frac{M_{Z'}}{M_Z} \right)^2 \frac{1}{K^2(M_{Z'}; Cs)}$
<i>E158 (SLAC)</i>	160 MeV	0.2329(13)	$\epsilon^2 < \frac{62 \times 10^{-6}}{\delta^2} \left( \frac{(160 \text{ MeV})^2 + M_{Z'}^2}{M_{Z'} M_Z} \right)^2$
<i>Qweak (JLAB)</i>	170 MeV	$\pm 0.0007$	$\epsilon^2 < \frac{7.4 \times 10^{-6}}{\delta^2} \left( \frac{(170 \text{ MeV})^2 + M_{Z'}^2}{M_{Z'} M_Z} \right)^2$
<i>Moller (JLAB)</i>	75 MeV	$\pm 0.00029$	$\epsilon^2 < \frac{1.3 \times 10^{-6}}{\delta^2} \left( \frac{(75 \text{ MeV})^2 + M_{Z'}^2}{M_{Z'} M_Z} \right)^2$
<i>MESA (Mainz)</i>	50 MeV	$\pm 0.00037$	$\epsilon^2 < \frac{2.1 \times 10^{-6}}{\delta^2} \left( \frac{(50 \text{ MeV})^2 + M_{Z'}^2}{M_{Z'} M_Z} \right)^2$

Table 4.5: Existing (upper block) and projected (lower block) constraints on the kinetic mixing parameter as a function of the mass mixing parameter  $\delta$  and the  $U(1)_X$  boson mass  $M_{Z'}$ . All masses in MeV. Table taken from [30].

statement we can take  $U(1)_{B-L}$  as an example, in which case we find that

$$\left| -59.84\delta^2 - 220\delta \left( \epsilon \frac{M_Z}{M_{Z'}} \right) \sin \theta_W - 133\delta^2 \tan^2 \beta \right| \times K(M_{Z'}; Cs) < 0.6. \quad (4.46)$$

where we use the fact that, in this case,

$$\delta = \frac{M_Z}{M_{Z'}} \epsilon_Z \cos \theta_W. \quad (4.47)$$

If we neglect powers of  $\delta$  higher than 2 (and assume that  $\tan \beta$  is not big enough), we obtain the constraint on  $\epsilon^2$  shown in the first row of table 4.5.

Low energy experiments offer another way to constrain the kinetic mixing parameter. The presence of an additional gauge boson that mixes with the SM  $Z$  boson generates the following shift in the measurement of  $\sin \theta_W$  at an energy  $Q$  [30]

$$\Delta \sin^2 \theta_W = -0.42\epsilon\delta M_Z \frac{M_{Z'}}{M_{Z'}^2 + Q^2}. \quad (4.48)$$

The measured error of  $\sin^2 \theta_W(M_Z)$  at E158 [31], Qweak [32], Moller (JLAB) [33] and MESA [34, 35] experiments are shown in the third column of table 4.5, generating the limits of the fourth column.

#### 4.4.4 Neutrino Electron Scattering

To finish this section, we review one last class of experiments able to constrain models with additional gauge bosons that lie in the intensity frontier: neutrino-

<i>experiment</i>	<i>incoming neutrino</i>	$\langle E_\nu \rangle$	$E_k$
<i>TEXONO-NPCGe</i> [37]	$\bar{\nu}_e$	1 – 2 MeV	0.35 – 12 keV
<i>TEXONO-CsI(Tl)</i> [38]	$\bar{\nu}_e$	1 – 2 MeV	3 – 8 MeV
<i>BOREXINO</i> [39]	$\nu_e$	862 keV	270 – 665 keV
<i>GEMMA</i> [40]	$\bar{\nu}_e$	1 – 2 MeV	3 – 25 keV
<i>CHARM II</i> [41]	$\nu_\mu$	23.7 GeV	3 – 24 GeV
	$\bar{\nu}_\mu$	19.1 GeV	3 – 24 GeV

Table 4.6: Neutrino-electron scattering experiments used to constrain  $g_{B-L}$  in fig. 4.6.

electron scattering. As this is a purely leptonic process, it suffers from low-backgrounds which makes it ideal for precision analyses. In the SM the process can be mediated by the charged and neutral currents shown in the upper panel of fig. 4.5. Additional diagrams arising from the inclusion of  $Z'$ , shown in the lower panel of fig. 4.5, lead to modifications to the predicted number of events measured in the different facilities. To obtain a notion of the limits expected from these experiments we focus here on the most well studied model from table 4.2, i.e.  $U(1)_{B-L}$ .

Due to strong constraints on the kinetic mixing parameter, the dominant contribution relevant for new physics in fig. 4.6 is the lower left diagram, which implies that we neglect  $\epsilon$  in this subsection. This diagram generates the following cross section [36],

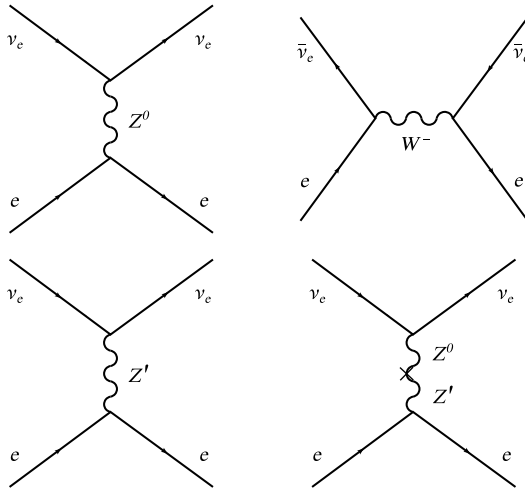


Figure 4.5: Feynman diagrams for neutrino-electron scattering. The upper diagrams represent the SM contribution, while the lower diagrams shows the contribution of  $Z'$ .



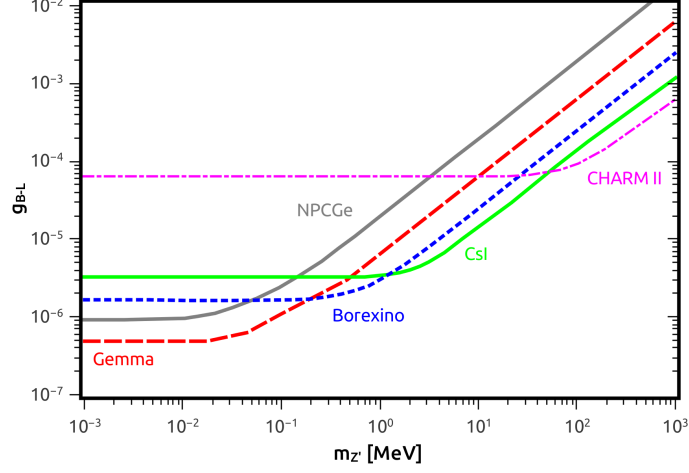


Figure 4.6: Constraints on  $g_{B-L}$  using neutrino-electron scattering experiments.

$$\frac{d\sigma}{dE_k} = \frac{g_{B-L}^4 m_e}{4\pi E_\nu^2 (M_{Z'}^2 + 2m_e E_k)^2} (2E_\nu^2 + E_k^2 - eE_k E_\nu - m_e E_k) \quad (4.49)$$

where  $E_k$  is the electron recoil energy,  $E_\nu$  the energy of the incoming neutrino,  $m_e$  the electron mass, and  $G_F$  the Fermi constant.

In addition to eq. (4.49) it is necessary to include the interference terms between all the possible channels, as it is done in [42]. The differential rate due to new physics in an experiment where  $\rho_e$  is the electron number density per kg of the target mass, after a live time  $t$ , is given by

$$\left( \frac{dR}{dE_k} \right)_{NP} = t \rho_e \int_{E_\nu^{min}}^{\infty} \frac{d\Phi}{dE_\nu} \frac{d\sigma}{dE_k} dE_\nu, \quad (4.50)$$

where  $\Phi$  is the neutrino flux.

After integrating on  $E_k$  we can obtain 90% exclusion limits, as we did in chapter 3, using a  $\chi^2$  analysis

$$\chi^2 = \sum_{i=1} \frac{(R_i^{\text{exp}} - (R_i^{\text{SM}} + R^{\text{NP}}))^2}{\sigma_i} \quad (4.51)$$

where we summed over the energy bins  $i$  and  $R_i^{\text{exp}}$ ,  $R_i^{\text{SM}}$  are the measured and SM predicted rates respectively, while  $\sigma_i$  is the statistical error of  $R_i^{\text{exp}}$ .

Using the experiments listed in table 4.6, where the average incoming neutrino energy and the electron recoil energy limits are specified, we can use eq. (4.51) in order to constrain the  $U(1)_{B-L}$  coupling constant as shown in fig. 4.6.

Despite the fact that we have used  $U(1)_{B-L}$  as a benchmark scenario in order to obtain qualitative limits, it is possible to translate these bounds to the other models in table 4.2. If we call  $g_{Z'ee}$  and  $g_{Z'\nu\nu}$  the  $Z'$  coupling constants to electrons and neutrinos respectively, we can see that the contribution from  $Z'$  in eq. (4.49) scales with  $g_{Z'ee}^2 g_{Z'\nu\nu}^2$ . As the interference terms scale with  $g_{Z'ee} g_{Z'\nu\nu}$  as it is shown in [42], it is possible to rescale these constraints knowing that the vectorial coupling to a fermion  $f$  is given by

$$g_{fv} = \frac{g_X}{2(Q_{fL} + Q_{fR})} \quad (4.52)$$

where  $Q_{fL}$  and  $Q_{fR}$  are the charges of the left- and right-handed field components under  $U(1)_X$  listed in table 4.2.

## 4.5 The Dark Matter Possibility

To conclude this chapter we briefly explore the possibility of adding a dark matter candidate  $\chi$ , while maintaining the defining features of the framework developed. We consider a fermionic dark matter particle, which has to be vector-like in order to maintain the theory anomaly-free. As this particle is charged under  $U(1)_X$ , the  $Z'$  acts as a portal between the dark and the visible sector, exactly like in the model presented in section 2.2 and depicted in fig. 4.7, which allows for a rich phenomenology as shown for example in [43, 44]. One important difference with the quoted references and with the model on chapter 2 is that we focus here in the  $M_{Z'} \ll M_Z$  regime, for which the additional parameter introduced, given by the dark matter mass  $M_\chi$ , must also be small in order for the diagram presented in fig. 4.7 to be relevant.

The implementation of this additional particle is straightforward, but in order to combine the constraints from the previous section and compare their relevance, we focus once again on  $U(1)_{B-L}$ . From the free parameters to constrain we select the kinetic mixing parameter  $\epsilon$  and for a quantitative assessment we fix the dark matter mass to  $M_\chi = 50$  MeV and the coupling constant to  $g_{B-L} = 1$ . Under these assumptions we can impose limits on  $\epsilon$  as a function of  $M_{Z'}$  as shown in fig. 4.8. The first constraint to impose, as we did in section 2.2.2, is the relic density that we assume here to be generated through thermal processes. In order to reproduce the measured density in eq. (1.22), the free parameters must lie in the black curve of fig. 4.8. Another possible constraint coming exclusively from the dark matter inclusion is direct detection. We implement it here by considering the XENON100 dataset [45], which translates into the orange curve of the same figure. The other relevant constraints are rare meson decays (magenta region), atomic parity violation in caesium for different values of  $\delta$  (purple dashed curves) and neutrino-electron scattering in the TEXONO

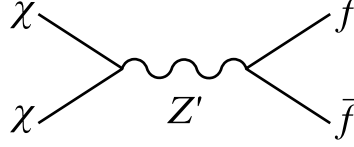


Figure 4.7: Feynman diagram showing the  $Z'$  portal connecting the dark matter particle  $\chi$  and SM fermions  $f$ .

experiment (red dashed curve). Finally, there are two types of experiments that were included in fig. 4.8, but not discussed in section 4.4. The muon anomalous magnetic moment whose measured value presents a  $3.6\sigma$  discrepancy with respect to the SM prediction [46]

$$\Delta a_\mu = a_\mu^{exp} - a_\mu^{SM} = (287 \pm 80) \times 10^{-11}, \quad (4.53)$$

which can be explained by these kind of models, as the additional gauge boson introduces a correction given by [47, 48]

$$\Delta a_\mu(Z') \simeq \frac{1}{12\pi^2} \frac{m_\mu^2}{m_{Z'}^2} (g_v^2 - 5g_a^2). \quad (4.54)$$

This limit is shown in the green  $3\sigma$  region, while an additional cyan curve shows the limit coming from the precise measurements of  $(g-2)_e$  and the determination of the fine structure constant [49, 50]. Both of these limits were taken from [51]. The second type of experiments not previously mentioned are

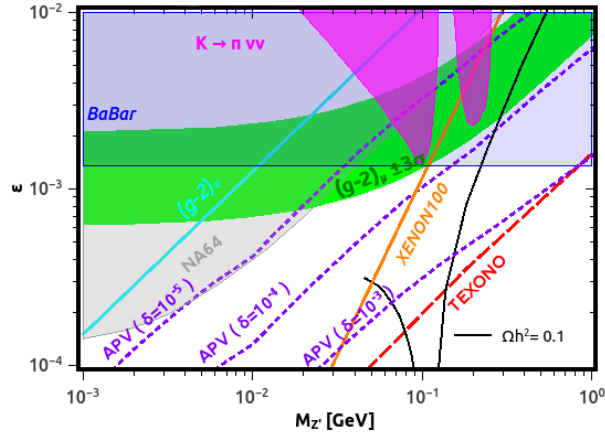


Figure 4.8: Dark matter constraints summary for  $M_\chi = 50 \text{ MeV}$  and  $g_{B-L} = 1$ .

low energy accelerators. Colliders like the BaBar experiment [52] (blue area) and fixed target experiments like NA64 [53] (gray area) can constrain dark photon decays such as

$$e^+e^- \rightarrow \gamma Z' \rightarrow \gamma \ell^+ \ell^-, \quad (4.55)$$

where the dark photon-charged leptons coupling is proportional to  $\epsilon$ .

In the particular example given in this section, we can observe that low energy experiments like TEXONO are in fact capable of imposing the strongest constraints, due to the low mass range needed for this particular dark matter candidate. This is in stark contrast to what happened in chapter 2, where high energy colliders like the LHC offered limits almost insurmountable to the limits obtained by other kind of research facilities, pointing again to the essential complementarity gained from exploring a wide variety of experiments; an approach that has been our main focus throughout this thesis.

## References

- [1] **ATLAS** Collaboration, G. Aad et al., *Observation of a new particle in the search for the Standard Model Higgs boson with the ATLAS detector at the LHC*, *Phys. Lett.* **B716** (2012) 1 [[arXiv:1207.7214](#)].
- [2] **CMS** Collaboration, S. Chatrchyan et al., *Observation of a new boson at a mass of 125 GeV with the CMS experiment at the LHC*, *Phys. Lett.* **B716** (2012) 30 [[arXiv:1207.7235](#)].
- [3] G.C. Branco, P.M. Ferreira, L. Lavoura, M.N. Rebelo, M. Sher and J.P. Silva, *Theory and phenomenology of two-Higgs-doublet models*, *Phys. Rept.* **516** (2012) 1 [[arXiv:1106.0034](#)].
- [4] T.D. Lee, *A Theory of Spontaneous T Violation*, *Phys. Rev.* **D8** (1973) 1226.
- [5] S.L. Glashow and S. Weinberg, *Natural Conservation Laws for Neutral Currents*, *Phys. Rev.* **D15** (1977) 1958.
- [6] E.A. Paschos, *Diagonal Neutral Currents*, *Phys. Rev.* **D15** (1977) 1966.
- [7] S.L. Glashow, J. Iliopoulos and L. Maiani, *Weak Interactions with Lepton-Hadron Symmetry*, *Phys. Rev.* **D2** (1970) 1285.
- [8] D. Atwood, L. Reina and A. Soni, *Phenomenology of two Higgs doublet models with flavor changing neutral currents*, *Phys. Rev.* **D55** (1997) 3156 [[hep-ph/9609279](#)].
- [9] **Particle Data Group** Collaboration, C. Patrignani et al., *Review of Particle Physics*, *Chin. Phys.* **C40** (2016) 100001.
- [10] P. Ko, Y. Omura and C. Yu, *A Resolution of the Flavor Problem of Two Higgs Doublet Models with an Extra  $U(1)_H$  Symmetry for Higgs Flavor*, *Phys. Lett.* **B717** (2012) 202 [[arXiv:1204.4588](#)].
- [11] H.S. Lee and E. Ma, *Gauged  $B - x_i L$  origin of R Parity and its implications*, *Phys. Lett.* **B688** (2010) 319 [[arXiv:1001.0768](#)].
- [12] W. Rodejohann and C.E. Yaguna, *Scalar dark matter in the BL model*, *JCAP* **1512** (2015) 032 [[arXiv:1509.0403](#)].
- [13] K. Kaneta, Z. Kang and H.S. Lee, *Right-handed neutrino dark matter under the BL gauge interaction*, *JHEP* **02** (2017) 031 [[arXiv:1606.0931](#)].
- [14] B. Batell, M. Pospelov and B. Shuve, *Shedding Light on Neutrino Masses with Dark Forces*, *JHEP* **08** (2016) 052 [[arXiv:1604.0609](#)].

- [15] M. Abbas and S. Khalil, *Neutrino masses, mixing and leptogenesis in TeV scale  $B - L$  extension of the standard model*, *JHEP* **04** (2008) 056 [[arXiv:0707.0841](#)].
- [16] J. Heeck, *Leptogenesis with Lepton-Number-Violating Dirac Neutrinos*, *Phys. Rev.* **D88** (2013) 076004 [[arXiv:1307.2241](#)].
- [17] K.S. Babu, C.F. Kolda and J. March-Russell, *Implications of generalized  $Z - Z'$  prime mixing*, *Phys. Rev.* **D57** (1998) 6788 [[hep-ph/9710441](#)].
- [18] P. Langacker, *The Physics of Heavy  $Z'$  Gauge Bosons*, *Rev. Mod. Phys.* **81** (2009) 1199 [[arXiv:0801.1345](#)].
- [19] D. Curtin, R. Essig, S. Gori and J. Shelton, *Illuminating Dark Photons with High-Energy Colliders*, *JHEP* **02** (2015) 157 [[arXiv:1412.0018](#)].
- [20] H. An, M. Pospelov, J. Pradler and A. Ritz, *Direct Detection Constraints on Dark Photon Dark Matter*, *Phys. Lett.* **B747** (2015) 331 [[arXiv:1412.8378](#)].
- [21] H.S. Lee and M. Sher, *Dark Two Higgs Doublet Model*, *Phys. Rev.* **D87** (2013) 115009 [[arXiv:1303.6653](#)].
- [22] **ALEPH** Collaboration, R. Barate et al., *Search for an invisibly decaying Higgs boson in  $e^+e^-$  collisions at 189-GeV*, *Phys. Lett.* **B466** (1999) 50.
- [23] **L3** Collaboration, P. Achard et al., *Search for an invisibly-decaying Higgs boson at LEP*, *Phys. Lett.* **B609** (2005) 35 [[hep-ex/0501033](#)].
- [24] **OPAL** Collaboration, G. Abbiendi et al., *Search for invisibly decaying Higgs bosons in  $e^+e^- \rightarrow Z^0 h^0$  production at  $\sqrt{s} = 183 - 209$  GeV*, *Phys. Lett.* **B682** (2010) 381 [[arXiv:0707.0373](#)].
- [25] L.J. Hall and M.B. Wise, *Flavor changing Higgs boson couplings*, *Nucl. Phys.* **B187** (1981) 397.
- [26] M. Freytsis, Z. Ligeti and J. Thaler, *Constraining the Axion Portal with  $B \rightarrow Kl^+l^-$* , *Phys. Rev.* **D81** (2010) 034001 [[arXiv:0911.5355](#)].
- [27] H. Davoudiasl, H.S. Lee and W.J. Marciano, *'Dark'  $Z$  implications for Parity Violation, Rare Meson Decays, and Higgs Physics*, *Phys. Rev.* **D85** (2012) 115019 [[arXiv:1203.2947](#)].
- [28] C. Bouchiat and P. Fayet, *Constraints on the parity-violating couplings of a new gauge boson*, *Phys. Lett.* **B608** (2005) 87 [[hep-ph/0410260](#)].

- [29] W.J. Marciano and A. Sirlin, *Radiative corrections to atomic parity violation*, *Phys. Rev.* **D27** (1983) 552.
- [30] H. Davoudiasl, H.S. Lee and W.J. Marciano, *Muon Anomaly and Dark Parity Violation*, *Phys. Rev. Lett.* **109** (2012) 031802 [[arXiv:1205.2709](#)].
- [31] **SLAC E158** Collaboration, P.L. Anthony et al., *Precision measurement of the weak mixing angle in Moller scattering*, *Phys. Rev. Lett.* **95** (2005) 081601 [[hep-ex/0504049](#)].
- [32] D.S. Armstrong et al., *The Qweak Experiment: A Search for New Physics at the TeV Scale via a Measurement of the Proton's Weak Charge*, [arXiv:1202.1255](#).
- [33] **MOLLER** Collaboration, J. Benesch et al., *The MOLLER Experiment: An Ultra-Precise Measurement of the Weak Mixing Angle Using Moller Scattering*, [arXiv:1411.4088](#).
- [34] N. Berger et al., *Measuring the weak mixing angle with the P2 experiment at MESA*, *J. Univ. Sci. Tech. China* **46** (2016) 481 [[arXiv:1511.0393](#)].
- [35] R. Bucoveanu, M. Gorchtein and H. Spiesberger, *Precision Measurement of  $\sin^2 \theta_w$  at MESA*, *PoS LL2016* (2016) 061 [[arXiv:1606.0926](#)].
- [36] R. Harnik, J. Kopp and P.A.N. Machado, *Exploring  $\nu$  Signals in Dark Matter Detectors*, *JCAP* **1207** (2012) 026 [[arXiv:1202.6073](#)].
- [37] J.W. Chen, H.C. Chi, H.B. Li, C.P. Liu, L. Singh, H.T. Wong, C.L. Wu and C.P. Wu, *Constraints on millicharged neutrinos via analysis of data from atomic ionizations with germanium detectors at sub-keV sensitivities*, *Phys. Rev.* **D90** (2014) 011301 [[arXiv:1405.7168](#)].
- [38] **TEXONO** Collaboration, M. Deniz et al., *Measurement of  $\text{Nu}(e)\text{-bar}$ -Electron Scattering Cross-Section with a CsI(Tl) Scintillating Crystal Array at the Kuo-Sheng Nuclear Power Reactor*, *Phys. Rev.* **D81** (2010) 072001 [[arXiv:0911.1597](#)].
- [39] G. Bellini et al., *Precision measurement of the  $7\text{Be}$  solar neutrino interaction rate in Borexino*, *Phys. Rev. Lett.* **107** (2011) 141302 [[arXiv:1104.1816](#)].
- [40] A.G. Beda, E.V. Demidova, A.S. Starostin, V.B. Brudanin, V.G. Egorov, D.V. Medvedev, M.V. Shirchenko and T. Vyllov, *GEMMA experiment: Three years of the search for the neutrino magnetic moment*, *Phys. Part. Nucl. Lett.* **7** (2010) 406 [[arXiv:0906.1926](#)].

- [41] **CHARM-II** Collaboration, P. Vilain et al., *Measurement of differential cross-sections for muon-neutrino electron scattering*, *Phys. Lett.* **B302** (1993) 351.
- [42] S. Bilmis, I. Turan, T.M. Aliev, M. Deniz, L. Singh and H.T. Wong, *Constraints on Dark Photon from Neutrino-Electron Scattering Experiments*, *Phys. Rev.* **D92** (2015) 033009 [[arXiv:1502.0776](#)].
- [43] G. Arcadi, Y. Mambrini, M.H.G. Tytgat and B. Zaldivar, *Invisible  $Z'$  and dark matter: LHC vs LUX constraints*, *JHEP* **03** (2014) 134 [[arXiv:1401.0221](#)].
- [44] G. Arcadi, Y. Mambrini and F. Richard, *Z-portal dark matter*, *JCAP* **1503** (2015) 018 [[arXiv:1411.2985](#)].
- [45] **XENON100** Collaboration, E. Aprile et al., *Dark Matter Results from 225 Live Days of XENON100 Data*, *Phys. Rev. Lett.* **109** (2012) 181301 [[arXiv:1207.5988](#)].
- [46] T. Blum, A. Denig, I. Logashenko, E. de Rafael, B. Lee Roberts, T. Teubner and G. Venanzoni, *The Muon ( $g-2$ ) Theory Value: Present and Future*, [arXiv:1311.2198](#).
- [47] J.P. Leveille, *The Second Order Weak Correction to ( $G-2$ ) of the Muon in Arbitrary Gauge Models*, *Nucl. Phys.* **B137** (1978) 63.
- [48] F. Jegerlehner and A. Nyffeler, *The Muon  $g-2$* , *Phys. Rept.* **477** (2009) 1 [[arXiv:0902.3360](#)].
- [49] B.C. Odom, D. Hanneke, B. D'Urso and G. Gabrielse, *New Measurement of the Electron Magnetic Moment Using a One-Electron Quantum Cyclotron*, *Phys. Rev. Lett.* **97** (2006) 030801. [Erratum: *Phys. Rev. Lett.* **99**, 039902(2007)].
- [50] D. Hanneke, S. Fogwell and G. Gabrielse, *New Measurement of the Electron Magnetic Moment and the Fine Structure Constant*, *Phys. Rev. Lett.* **100** (2008) 120801 [[arXiv:0801.1134](#)].
- [51] M. Pospelov, *Secluded  $U(1)$  below the weak scale*, *Phys. Rev.* **D80** (2009) 095002 [[arXiv:0811.1030](#)].
- [52] **BaBar** Collaboration, J.P. Lees et al., *Search for a Dark Photon in  $e^+e^-$  Collisions at BaBar*, *Phys. Rev. Lett.* **113** (2014) 201801 [[arXiv:1406.2980](#)].
- [53] **NA64** Collaboration, D. Banerjee et al., *Search for a new  $X(16.7)$  boson and dark photons in the NA64 experiment at CERN*, [arXiv:1803.0774](#).



# 5

## Summary and Outlook

Slowly but steadily, the evidence advocating the dark matter case has been piling up over the course of the last four decades. It has grown to—arguably—become the biggest unsettled issue at the intersection of astronomy, particle physics, astrophysics and cosmology. Some of its properties have been properly assessed, like the amount needed in order to reproduce the largest patterns observed in the universe. Its precise nature, however, remains largely unknown. As a result, there is no shortage of well motivated candidates arising from particle physics. Furthermore, theories of modified gravity cannot be completely excluded at the moment, despite the fact that attempts at overhauling gravity have failed at explaining the entire constellation of observational evidence. If the solution to this conundrum *does* come from particle physics, it is quite natural to conceive that it might be linked to other open questions in the field, as has historically happened. Among these enigmas are the origin and nature of neutrino masses. With this in mind, we have explored in the present work different dark matter candidates, in connection with neutrino physics, and considered their experimental imprints.

Due to the sheer amount of experimental data available regarding dark matter, it is sensible to corner dark matter models using different experimental strategies. This is the point of view adopted in this work. In chapter 2 we described two different types of simplified models characterized by their economy in terms of parameters, and established the way in which those free parameters can be constrained. The first model is the dark sequential  $Z'$  portal, in which dark matter is considered to be a Majorana fermion, while its sole connection to the

SM is given by a  $Z'$  boson. After we determine the region in parameter space in which these assumptions produce the right amount of dark matter, we find that most of it can be excluded using a combination of direct, indirect and collider searches, depending on the value of the coupling between dark matter and  $Z'$ . Collider searches, like those performed at LHC, produced in fact the most stringent limits for small values ( $\leq 1$ ) of this coupling, revealing their importance in simplified models and despite their inability to directly measure the dark matter candidate. On the other hand, we could not impose relevant constraints to the parameter space using the detection of  $\gamma$ -rays coming from our galactic neighbourhood, due to the chosen nature of the dark matter particle. Coincidentally, these searches are the only ones able to constrain the second simplified model introduced: the neutrino portal. In this model we described a heavy right-handed neutrino linking the dark with the visible sector, through seesaw type-I interactions. Due to their feeble nature, these interactions can only be tested through indirect detection. The relevant quantity in this case is the energy spectrum, which is not sensitive to the mixing structure of the neutrinos. Consequently, this analysis introduced an orthogonal test to sterile neutrino models in the regime of suppressed mixings. After analysing data coming from  $\gamma$ -ray telescopes like Fermi-LAT and H.E.S.S. we were able to exclude thermally produced dark matter with masses below 200 [GeV]. As a conclusion to this chapter, we highlight the value of complementarity coming from the different experimental approaches and how it can be exploited as a tool to shed light on the dark matter mystery. The approach used in this chapter could serve as a template for future studies in which the role of the mediator particle is emphasized.

Dominating the dark matter landscape, WIMPs have remained the main focus of experimental endeavours. We have argued, however, that many reasons exist to remain agnostic regarding its identity, specially due to unresolved astrophysical issues at small scales ( $\leq 0.1$  Mpc). In this direction, we proposed in chapter 3 a new method to use existing facilities aimed at WIMP direct detection to search for keV sterile neutrinos as dark matter. We noticed in this study that an electron recoil signal can be produced whenever a keV mass neutrino scatters inelastically off bound electrons. This signal, considered as background from the point of view of WIMP detection, can constrain the sterile neutrino parameter space of masses and mixing angles. The limits projected for an experiment like XENONIT are the most sensitive for Earth based experiments, for masses above 20 keV and using as the only assumption dark matter entirely consisting of sterile neutrinos. Despite stronger exclusion limits arising from  $X$ -ray searches, the bounds presented are independent and hence complementary to them. The original use of well established experiments with the purpose of probing less studied aspects of alternative dark matter candidates, as was done here, should

be particularly stressed; specially considering the lack of positive results coming from deep-rooted paradigms.

The notion of gauge symmetry has been a guiding principle for the SM since its conception and has paved the way to its many successes. In order to reproduce this success, while addressing some of its murkier features, many BSM attempts rely on extended gauge sectors. In this vein, we introduced in chapter 4 a gauged  $U(1)$  symmetry in the context of 2HDM with the goal of avoiding the presence of FCNI in these models, while at the same time providing a natural way to obtain neutrino masses through the seesaw type-I mechanism. Each assignment of fermionic quantum numbers defines a different model, and our restrictions led us to identify a set of eight groups. In the spirit of this thesis, motivated by a strong interplay between theory and phenomenology, we studied the impact of this family of models in different experimental facilities, ranging from low energy (like APV or neutrino-electron scattering) to the highest available energies (like Higgs physics at the LHC). Interesting constraints were derived from this analysis, most of them model independent. Whenever a specific model was needed to obtain quantitative assessments, we opted for using  $U(1)_{B-L}$  as an example, due to its strong connections to other particle physics topics, specially to dark matter and neutrino physics. Nevertheless, we provided methods to translate the relevant limits to the other models in study. In this analysis we considered the light  $Z'$  regime in which  $M_{Z'} \ll M_Z$  and due to the fact that this choice dictates the phenomenology of the model, the complementary regime of heavier  $Z'$  masses in this context is worth considering for future studies. We also showed, with a particular example, that dark matter can be naturally accommodated in this type of models, but a thorough study of this ambitious framework is left for future work.



# A

## Description of the Software Used in the Neutrino Portal Model

### A.1 Pythia

`Pythia` is a Monte Carlo event generator for high-energy collisions, mainly used for event simulation and statistical analysis in colliders [1]. Despite not involving spin correlations, it produces a reasonable approximation applicable to the model at hand. It does include parton showers and hadronization in order to obtain, in this case, the final  $\gamma$  spectrum. This is implemented in a different way in comparison to, for example, `Herwig` [2] which is another widely used event generator (see [3] for a discussion in this direction).

As it was already discussed in section 2.3, the non-relativistic dark matter annihilation of a particle with mass  $M_\chi$  is equivalent to the decay of a resonance  $\mathcal{D}$  with mass  $M_{\mathcal{D}} = 2M_\chi$ . This decay into SM particles can be easily implemented in an event generator like `Pythia` 8.219. Besides the introduction of the new scalar resonance, we also include a new fermion to which the scalar particle exclusively decays in order to appropriately describe the neutrino portal introduced in section 2.3. We implement the branching ratios of the right-handed neutrino shown in eqs. (2.12) to (2.14) as a function of mass, in order to account for kinematic thresholds.

We express our results as a function of the energy fraction

$$x := \frac{E_\gamma}{M_\chi}, \tag{A.1}$$

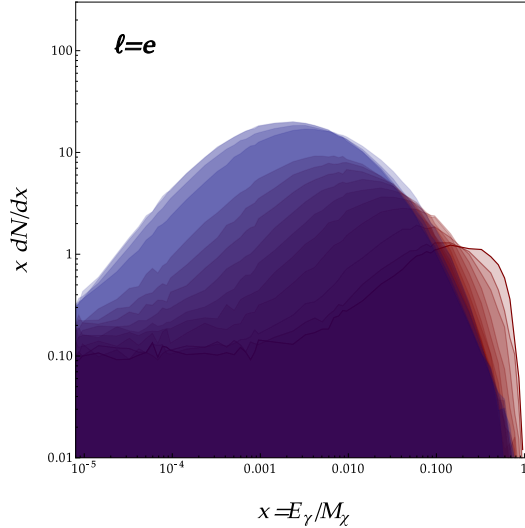


Figure A.1: Gamma spectra for the annihilation of a dark matter particle with mass  $M_\chi = 785$  GeV for 14 different values of  $M_N$ , going from  $M_N = 1$  GeV (red to the right) to  $M_N = 545$  GeV (blue to the left). For simplicity we show just the case in which  $N$  mixes exclusively with  $\ell = e$ .

where  $E_\gamma$  is the kinetic energy of the final photons in the  $\mathcal{D}$  rest frame. The spectrum consists of the particle multiplicity as a function of the logarithmic energy fraction  $dN/d \log x = \log(10) x dN/dx$ . In order to check that the inclusion of the decay widths were properly implemented, we plot the gamma spectra for 14 different right-handed neutrino masses

$$M_N = [1.000, 1.624, 2.637, 4.281, 6.952, 11.289, 18.330, 29.763, 48.329, 78.476, 127.427, 206.914, 335.982, 545.559]$$

in fig. A.1, for a given dark matter mass  $M_\chi = 785$  GeV. In the transition red to blue it is possible so observe the  $M_N < M_Z$  to  $M_N > M_Z$  transition (or 3 to 2 body decays), which is rather smooth, as expected.

As a final comment related to the spectra generated, it is worth to mention that we did not include inverse Compton scattering, which is usually relevant for annihilations into  $e^+e^-$  and  $\mu^+\mu^-$  pairs. However there are a number of reasons why we consider that they do not play a significant role in this case. First of all, unlike purely leptonic decays in which inverse Compton scattering is certainly important, in this case the right-handed neutrinos can decay to  $\ell^\pm W^\mp$ ,  $\nu_\ell Z$  and  $\nu_\ell H$  rendering the hadronic contribution dominant as it can be seen from fig. 2.10, in which the exchange  $e \leftrightarrow \mu$  produces no noticeable change. Additionally, in the case of dSphs this effect hardly plays any role

due to low interstellar radiation field and unknown diffusion, while in the GC is subject to large uncertainties due to our lack of knowledge regarding the diffusion coefficient. At any rate, were the inclusion of this effect introduce any change it would lead to stronger constraints, for which we qualify our analysis as conservative in this sense.

## A.2 GAMBIT & gamLike

The Global And Modular Beyond-the-Standard-Model Inference Tool (GAMBIT) [4] is a global fitting package which combines extensive calculations of observables and likelihoods in particle and astroparticle physics. It is designed in a modular way and for the statistical analysis of section 2.3, we used one of said modules: `DarkBit` [5], and more specifically, the dedicated likelihood calculator for gamma-ray observations `gamLike`. This package includes several options for the  $J$ -factors introduced in section 1.3.4.1, which allows to marginalise or profile over the  $J$ -factor uncertainties. For the analysis of the combined dSphs limits performed in section 2.3.2.1, for example, we profile over the  $J$ -factors of all 15 adopted dwarfs separately for determining the combined likelihood value.

## References

- [1] T. Sjostrand, S. Mrenna and P.Z. Skands, *A Brief Introduction to PYTHIA 8.1*, *Comput. Phys. Commun.* **178** (2008) 852 [[arXiv:0710.3820](#)].
- [2] G. Corcella, I.G. Knowles, G. Marchesini, S. Moretti, K. Odagiri, P. Richardson, M.H. Seymour and B.R. Webber, *HERWIG 6: An Event generator for hadron emission reactions with interfering gluons (including supersymmetric processes)*, *JHEP* **01** (2001) 010 [[hep-ph/0011363](#)].
- [3] M. Cirelli, G. Corcella, A. Hektor, G. Hutsi, M. Kadastik, P. Panci, M. Raidal, F. Sala and A. Strumia, *PPPC 4 DM ID: A Poor Particle Physicist Cookbook for Dark Matter Indirect Detection*, *JCAP* **1103** (2011) 051 [[arXiv:1012.4515](#)]. [Erratum: *JCAP*1210,E01(2012)].
- [4] **GAMBIT** Collaboration, P. Athron et al., *GAMBIT: The Global and Modular Beyond-the-Standard-Model Inference Tool*, *Eur. Phys. J.* **C77** (2017) 784 [[arXiv:1705.0790](#)]. [Addendum: *Eur. Phys. J.* C78,no.2,98(2018)].
- [5] **The GAMBIT Dark Matter Workgroup** Collaboration, T. Bringmann et al., *DarkBit: A GAMBIT module for computing dark matter observables and likelihoods*, *Eur. Phys. J.* **C77** (2017) 831 [[arXiv:1705.0792](#)].





# B

## Cross Section of Neutrinos with Bound Electrons

### B.1 Kinematic Variables

In order to obtain the cross section for the following process

$$N_S(p_S)e^-(p_B) \rightarrow \nu_e(p_\nu)e^-(p_e) \quad (\text{B.1})$$

we can use the usual Lagrangian

$$\mathcal{L}_{eff} = -\frac{G_F}{\sqrt{2}} [\bar{\nu}_e \gamma^\mu (1 - \gamma^5) \nu_e] [\bar{e} \gamma_\mu (g'_V - g'_A \gamma^5) e], \quad (\text{B.2})$$

where  $g'_V = 1 + g_V$  and  $g'_A = 1 + g_A$ .

By defining an effective mass for the bound electron

$$\tilde{m} := E_B^2 - |\vec{p}_B|^2, \quad (\text{B.3})$$

it is possible to obtain the following averaged square amplitude<sup>1</sup>

$$\begin{aligned} |\mathcal{M}(N_S + e^- \rightarrow \nu_e + e^-)|^2 = & 16G_F^2 |U_{Se}|^2 [g_1^2 (s - m_e^2)(s - \tilde{m}^2 - m_S^2) \\ & + g_2^2 (u - \tilde{m}^2)(u - m_e^2 - m_S^2) \\ & + 2g_1 g_2 m_e \tilde{m} (t - m_S^2)] \end{aligned} \quad (\text{B.4})$$

---

<sup>1</sup>Notice that there is a mistake in eq. (14) of [1], where the last  $m_e^2$  factor should be replaced by  $m_e \tilde{m}$ . That equation is recovered then by setting  $m_S = 0$  in eq. (B.4).

with

$$\begin{aligned} g_1 &:= 1 + \frac{1}{2}(g_V + g_A), \\ g_2 &:= \frac{1}{2}(g_V - g_A) \end{aligned} \quad (\text{B.5})$$

as defined in chapter 3 and  $s, t, u$  the Mandelstam variables satisfying

$$s + t + u = m_e^2 + \tilde{m}^2 + m_S^2. \quad (\text{B.6})$$

If we define  $\hat{z}$  as the direction of the incoming neutrino, then the kinematic variables are given by

$$\begin{aligned} p_S &= (E_S, 0, 0, p_1) \\ p_B &= (E_B, p_2 \sin \theta_B \cos \phi_B, p_2 \sin \theta_B \sin \phi_B, p_2 \cos \theta_B) \\ p_e &= (E_e, p_R \sin \theta_R, 0, p_R \cos \theta_R), \end{aligned} \quad (\text{B.7})$$

where we have redefined  $p_1 := |\vec{p}_S|$ ,  $p_2 := |\vec{p}_B|$  and  $p_R := |\vec{p}_e|$  in order to avoid clutter notation. The angles lie by definition in the range

$$0 < \theta_B < \pi, \quad 0 < \phi_B < 2\pi, \quad (\text{B.8})$$

$$0 < \theta_R < \pi. \quad (\text{B.9})$$

In this case the Mandelstam variables are given then by

$$\begin{aligned} s &= (p_B + p_S)^2 = m_S^2 + \tilde{m}^2 + 2(E_S E_B - p_1 p_2 \cos \theta_B) \\ t &= (p_B - p_\nu)^2 = -m_S^2 + 2E_S(E_e - E_B) + 2p_1(p_2 \cos \theta_B - p_R \cos \theta_R) \\ u &= (p_B - p_e)^2 = m_S^2 + m_E^2 - 2(E_S E_e - p_1 p_R \cos \theta_e). \end{aligned} \quad (\text{B.10})$$

It is possible to obtain the recoil angle  $\theta_R$  as a function of the other variables by solving the condition obtained by neglecting the active neutrino masses

$$p_\nu^2 = (p_S + p_B - p_e)^2 = 0, \quad (\text{B.11})$$

which leads to

$$\tan\left(\frac{\theta_R}{2}\right) = \frac{\zeta_1 \pm \sqrt{\zeta_1^2 - \zeta_2}}{2\zeta_3}, \quad (\text{B.12})$$

where

$$\begin{aligned} \zeta_1 &:= 2p_2 p_R \sin \theta_B \cos \phi_B \\ \zeta_2 &:= 4[(E_e(E_S + E_B) - \xi)^2 - p_R^2(p_1 + p_2 \cos \theta_B)^2] \\ \zeta_3 &:= E_e(E_S + E_B) - \xi + p_R(p_1 + p_2 \cos \theta_B) \end{aligned} \quad (\text{B.13})$$

and

$$\xi := \frac{1}{2}(m_S^2 + \tilde{m}^2 + m_e^2) + E_S E_B - p_1 p_2 \cos \theta_B. \quad (\text{B.14})$$

The condition  $\zeta_1^2 \geq \zeta_2$  in eq. (B.12) translates into a condition for  $E_e$  given by

$$E_e^{min} \leq E_e \leq E_e^{max} \quad (\text{B.15})$$

where

$$\begin{aligned} E_e^{min} &:= \frac{\xi(E_S + E_B) - \xi' \sqrt{\xi^2 - m_e^2} ((E_S + E_B)^2 - \xi'^2)}{(E_S + E_B)^2 - \xi'^2}, \\ E_e^{max} &:= \frac{\xi(E_S + E_B) + \xi' \sqrt{\xi^2 - m_e^2} ((E_S + E_B)^2 - \xi'^2)}{(E_S + E_B)^2 - \xi'^2} \end{aligned} \quad (\text{B.16})$$

and

$$\xi'^2 := (p_1 + p_2 \cos \theta_B)^2 + (p_2 \sin \theta_B \cos \phi_B)^2. \quad (\text{B.17})$$

From the definition eq. (B.10), it is possible to obtain the Jacobian that appears in eq. (3.4) (remembering that in that equation  $E_k$  is the kinetic energy of the recoil electron, and then  $E_e = m_e + E_k$ ), which results in

$$\frac{du}{dE_e} = -2 \left( E_S - p_1 \frac{E_e}{p_R} \cos \theta_R + p_1 p_R \sin \theta_R \frac{d\theta_R}{dE_e} \right) \quad (\text{B.18})$$

where  $\frac{d\theta_R}{dE_e}$  can be obtained by deriving the condition eq. (B.11)

$$\frac{d\theta_R}{dE_e} = \frac{E_e(p_1 \cos \theta_R + p_2(\cos \theta_B \cos \theta_R + \sin \theta_B \cos \phi_B \sin \theta_R) - p_R(E_S + E_B))}{p_R^2[p_1 \sin \theta_R + p_2(\cos \theta_B \sin \theta_R - \sin \theta_B \cos \phi_B \cos \theta_R)]} \quad (\text{B.19})$$

## B.2 The Roothan-Hartree-Fock Method

The Hartree-Fock (HF) method was developed to obtain the approximate wave function and energy of a quantum many-body system for stationary states, while the Roothan-Hartree-Fock (RHF) method consists of applying a linear variation to the HF equations using a basic set of atomic orbitals [2].

In the RHF formalism the radial atomic orbitals of the HF wave functions are expanded as

$$R_{nl}(r) = \sum_j C_{jnl} S_{jl}(r) \quad (\text{B.20})$$

where (in coordinate space)

$$S_{jl}(r) = N_{jl} r^{n_{jl}-1} \exp(-Z_{jl} r) \quad (\text{B.21})$$

as defined in [3]. In momentum space we can write

$$\tilde{S}_{jl}(k) = 4\pi \int_0^\infty dr r^2 S_{jl}(r) j_l(kr), \quad (\text{B.22})$$

where  $j_l(kr)$  are the spherical Bessel functions.

Analogously to eq. (B.20) we can write in momentum space

$$\tilde{R}_{nl}(k) = \sum_j C_{jnl} \tilde{S}_{jl}(k), \quad (\text{B.23})$$

which is the expression needed in eq. (3.4) with  $t = nl$ . The corresponding expressions for  $\tilde{S}_{jl}$  as a function of  $Z_{jl}$  for a given  $n_{jl}$  are

- $l = 0$  ( $j = 1, \dots, 13$ ):

$$\begin{aligned} n_{j0} = 1 &\rightarrow \tilde{S}_{j0}(k) = \frac{16\pi Z_{j0}^{5/2}}{(Z_{j0}^2 + k^2)^2}, \\ n_{j0} = 2 &\rightarrow \tilde{S}_{j0}(k) = \frac{16\pi Z_{j0}^{5/2} (3Z_{j0}^2 - k^2)}{\sqrt{3}(Z_{j0}^2 + k^2)^3}, \\ n_{j0} = 3 &\rightarrow \tilde{S}_{j0}(k) = \frac{64\sqrt{10}\pi Z_{j0}^{9/2} (Z_{j0}^2 - k^2)}{5(Z_{j0}^2 + k^2)^4}, \\ n_{j0} = 4 &\rightarrow \tilde{S}_{j0}(k) = \frac{64\pi Z_{j0}^{9/2} (5Z_{j0}^4 - 10Z_{j0}^2 k^2 + k^4)}{\sqrt{35}(Z_{j0}^2 + k^2)^5}, \\ n_{j0} = 5 &\rightarrow \tilde{S}_{j0}(k) = \frac{128\sqrt{14}\pi Z_{j0}^{13/2} (3Z_{j0}^4 - 10Z_{j0}^2 k^2 + 3k^4)}{21(Z_{j0}^2 + k^2)^6}, \end{aligned} \quad (\text{B.24})$$

- $l = 1$  ( $j = 14, \dots, 25$ ):

$$\begin{aligned} n_{j1} = 2 &\rightarrow \tilde{S}_{j1}(k) = \frac{64\pi k Z_{j1}^{7/2}}{\sqrt{3}(Z_{j1}^2 + k^2)^3}, \\ n_{j1} = 3 &\rightarrow \tilde{S}_{j1}(k) = \frac{64\sqrt{10}\pi k Z_{j1}^{7/2} (5Z_{j1}^2 - k^2)}{15(Z_{j1}^2 + k^2)^4}, \\ n_{j1} = 4 &\rightarrow \tilde{S}_{j1}(k) = \frac{128\pi k Z_{j1}^{11/2} (5Z_{j1}^2 - 3k^2)}{\sqrt{35}(Z_{j1}^2 + k^2)^5}, \\ n_{j1} = 5 &\rightarrow \tilde{S}_{j1}(k) = \frac{128\sqrt{14}\pi k Z_{j1}^{11/2} (35Z_{j1}^4 - 42Z_{j1}^2 k^2 + 3k^4)}{105(Z_{j1}^2 + k^2)^6}, \end{aligned} \quad (\text{B.25})$$

- $l = 2$  ( $j = 26, \dots, 33$ ):

$$\begin{aligned} n_{j2} = 3 &\rightarrow \tilde{S}_{j2}(k) = \frac{128\sqrt{10}\pi k^2 Z_{j2}^{9/2}}{5(Z_{j2}^2 + k^2)^4}, \\ n_{j2} = 4 &\rightarrow \tilde{S}_{j2}(k) = \frac{128\pi k^2 Z_{j2}^{9/2} (7Z_{j2}^2 - k^2)}{\sqrt{35}(Z_{j2}^2 + k^2)^5}. \end{aligned} \quad (\text{B.26})$$

The numerical values of  $(C_{jln}, Z_{jl})$  are given in the corresponding table for  $Z = 54$  in [3], where  $C_{jln}$  is dimensionless while  $Z_{jl}$  are expressed in units of  $m_e\alpha = 3.73$  keV.

## References

- [1] G.J. Gounaris, E.A. Paschos and P.I. Porfyriadis, *Electron spectra in the ionization of atoms by neutrinos*, *Phys. Rev.* **D70** (2004) 113008 [[hep-ph/0409053](#)].
- [2] J.C.J.C. Slater, *Quantum theory of atomic structure*, International series in pure and applied physics McGraw-Hill (1960).
- [3] C.F. Bunge, J.A. Barrientos and A.V. Bunge, *Roothaan-hartree-fock ground-state atomic wave functions: Slater-type orbital expansions and expectation values for  $z=2-54$* , *Atomic data and nuclear data tables* **53** (1993) 113.



# C

## Theoretical Aspects of 2HDM

### C.1 Anomaly Cancellation

In this appendix we will obtain the anomaly cancellation conditions relevant for  $G_{\text{SM}} \times U(1)_X$ . If we call  $Y' = l, q, e, u, d$  the  $U(1)_X$  charges, then we have

- $[SU(3)_c]^2 U(1)_X$ :

$$\mathcal{A} = \text{Tr} \left[ \left\{ \frac{\lambda^a}{2}, \frac{\lambda^b}{2} \right\} Y'_R \right] - \text{Tr} \left[ \left\{ \frac{\lambda^a}{2}, \frac{\lambda^b}{2} \right\} Y'_L \right] \quad (\text{C.1})$$

$$\mathcal{A} \propto \sum_{\text{quarks}} Y'_R - \sum_{\text{quarks}} Y'_L = [3u + 3d] - [3 \cdot 2q] = 0. \quad (\text{C.2})$$

$$\Rightarrow u + d - 2q = 0. \quad (\text{C.3})$$

- $[SU(2)_L]^2 U(1)_X$ :

$$\mathcal{A} = -\text{Tr} \left[ \left\{ \frac{\sigma^a}{2}, \frac{\sigma^b}{2} \right\} Y'_L \right] \propto -\sum Y_L = -[2l + 3 \cdot 2q] = 0. \quad (\text{C.4})$$

$$\Rightarrow l = -3q. \quad (\text{C.5})$$

- $[U(1)_Y]^2 U(1)_X$ :

$$\mathcal{A} = \text{Tr} [\{Y_R, Y_R\} Y'_R] - \text{Tr} [\{Y_L, Y_L\} Y'_L] \propto \sum Y_R^2 Y'_R - \sum Y_L^2 Y'_L \quad (\text{C.6})$$

$$\mathcal{A} \propto \left[ (-2)^2 e + 3 \left( \frac{4}{3} \right)^2 u + 3 \left( -\frac{2}{3} \right)^2 d \right] - \left[ 2(-1)^2 l + 3 \cdot 2 \left( \frac{1}{3} \right)^2 q \right] = 0. \quad (\text{C.7})$$

$$\Rightarrow 6e + 8u + 2d - 3l - q = 0. \quad (\text{C.8})$$

•  $U(1)_Y [U(1)_X]^2$ :

$$\mathcal{A} = \text{Tr} [\{Y'_R, Y'_R\} Y_R] - \text{Tr} [\{Y'_L, Y'_L\} Y_L] \propto \sum Y_R Y_R'^2 - \sum Y_L Y_L'^2 \quad (\text{C.9})$$

$$\mathcal{A} \propto \left[ (-2) e^2 + 3 \left( \frac{4}{3} \right) u^2 + 3 \left( -\frac{2}{3} \right) d^2 \right] - \left[ 2(-1) l^2 + 3 \cdot 2 \left( \frac{1}{3} \right) q^2 \right] = 0. \quad (\text{C.10})$$

$$\Rightarrow -e^2 + 2u^2 - d^2 + l^2 - q^2 = 0. \quad (\text{C.11})$$

•  $[U(1)_X]^3$ :

$$\mathcal{A} = \text{Tr} [\{Y'_R, Y'_R\} Y'_R] - \text{Tr} [\{Y'_L, Y'_L\} Y'_L] \propto \sum Y_R'^3 - \sum Y_L'^3 \quad (\text{C.12})$$

$$\mathcal{A} \propto [e^3 + 3u^3 + 3d^3] - [2l^3 + 3 \cdot 2q^3] = 0. \quad (\text{C.13})$$

$$\Rightarrow e^3 + 3u^3 + 3d^3 - 2l^3 - 6q^3 = 0. \quad (\text{C.14})$$

If we use eq. (C.5) in order to express eq. (4.7) in terms of  $u$  and  $d$ , we obtain

$$q = \frac{(u+d)}{2},$$

$$l = \frac{-3(u+d)}{2}, \quad (\text{C.15})$$

$$e = -(2u+d),$$

$$h_2 = \frac{(u-d)}{2}.$$

which satisfy immediately eqs. (C.3), (C.5), (C.8) and (C.11), but in order to fulfil eq. (C.14) we require

$$e^3 + 3u^3 + 3d^3 - 2l^3 - 6q^3 = [-(2u+d)]^3 + 3u^3 + 3d^3 - 2 \left[ \frac{-3(u+d)}{2} \right]^3$$

$$- 6 \left[ \frac{(u+d)}{2} \right]^3$$

$$= -(2u+d)^3 + 3u^3 + 3d^3 + 6(u+d)^3$$

$$= u^3 + 8d^3 + 6u^2d + 12ud^2$$

$$= (u+2d)^3, \quad (\text{C.16})$$

which finally leads to

$$u = -2d. \quad (\text{C.17})$$